Seeps, slip, and subduction: A geochemical investigation of subduction zone hydrogeology and its links to megathrust slip behavior

Irita Aylward

A dissertation

submitted in partial fulfillment of the

requirements for the degree of

Doctor of Philosophy

University of Washington

2024

Reading Committee:

Evan A. Solomon, Chair

Deborah S. Kelley

Marta E. Torres

Program Authorized to Offer Degree:

School of Oceanography

University of Washington

Abstract

Seeps, slip, and subduction: A geochemical investigation of subduction zone hydrogeology and its links to megathrust slip behavior

Irita Aylward

Chair of the Supervisory Committee:
Evan A. Solomon
School of Oceanography

Subduction zone faults host a range of modes of slip spanning the spectrum from aseismic creep to devastating earthquakes. Hydrogeologic processes and conditions at the plate boundary and in surrounding sediments of the outer forearc have profound impacts on geomechanical processes in these convergent margins. Specifically, fluid production, permeability and fluid migration pathways, and pore fluid pressures, are thought to impact the nature and timing of slip behavior. While direct measurements of these properties are rare and limited to depths and locations only accessible by scientific ocean drilling, seafloor seeps hosted by deep-reaching faults provide a unique opportunity to assess the nature and efficiency of fluid flow through the system, informing on the state of pore fluid overpressure, the permeability structure, and the overall water budget of the outer forearc. This dissertation comprises three studies in which visual, geophysical, and chiefly geochemical methods are employed at sites of focused and diffuse flow (i.e., seeps and non-seeps, respectively) to investigate and advance our understanding of the interrelationships between mechanical and hydrogeologic processes at subduction zones.

Chapters 2 and 3 target active seafloor seeps and diffuse flow sites spanning the continental slope at the northern and southern Hikurangi margin, offshore of the North Island of New Zealand. Using pore water from sediment cores and heat flow measurements, Chapter 2 provides direct constraints on the source and flow rate of fluids traveling through the accretionary wedge. Results suggest that fluids are not efficiently draining from the plate boundary or surrounding sediments to the seafloor along fault zones. This implies that splay fault permeability at depth is low in the offshore forearc, likely contributing to the accumulation of pore fluid overpressure in the region of slow slip at northern Hikurangi.

Chapter 3 reports continuous fluid flow rates measured by benthic fluid flow meters deployed at seeps and non-seep locations over a 2-year period. Early in the deployment period, a large slow slip event (SSE) occurred beneath the instrument array offshore northern Hikurangi. Net flow polarities at non-seep locations are consistent with creeping on the shallow megathrust and locking in the slow slip source region in the inter-SSE period; flow transients reflect local volumetric strain induced by the slow slip event. At seep sites, flow transients additionally reflect gas-driven processes and possibly a shallow permeability response to the SSE, but convincing evidence of wide-spread fault-valving is not observed.

Chapter 4 presents a detailed examination of a single seep site called Pythia's Oasis, which is located ~20 km landward of the deformation front on the central Cascadia margin. The composition of the venting fluid suggests a fluid source within the subducting sediment section, at source temperatures of ~170 ˚C – 250 ˚C. Highly altered fluid compositions, along with anomalously high heat flow and rapid flow rates observed at Pythia's Oasis, are consistent with focused, long-range water flow along the Alvin Canyon fault in the mid-slope region. High permeability conditions along the Alvin Canyon fault and/or high pore fluid pressures in the central

Cascadia outer wedge likely permit sustained, high-volume discharge at Pythia's Oasis. These hydrogeologic conditions may play an important role in the reduced locking, increased seismicity, and other changes in margin characteristics that occur in this region. Solute fluxes at Pythia's Oasis resulting from the rapid, long-distance fluid transport are comparable to those at both high- and low-temperature hydrothermal discharge sites, indicating that subduction zone seeps may be more important for marine geochemical cycles than previously considered.

TABLE OF CONTENTS

LIST OF FIGURES

LIST OF TABLES

ACKNOWLEDGEMENTS

First and foremost, I would like to thank my parents, Ellen Martin and Barry Aylward, siblings Rowie and Xandra, and family for their unconditional love and support throughout this journey and into the next.

To my advisor, Evan Solomon, thank you for always being excited and curious about this research, for settling for nothing less than exceptional science, and for helping me develop into the writer, critical thinker, and pore water geochemist I have become over the last 6 years.

I owe special thanks to my supervisory committee, Deb Kelley, Marv Lilley, Andrea Ogston, Harold Tobin, and Marta Torres. Members of this incredible group have served as co-principal investigators for these studies, co-authors on the resultant papers, and also as mentors to me in the field and in the lab. I am also grateful to Rob Harris and Laura Wallace, who have co-led and co-authored these studies and who have served as additional mentors and collaborators.

I am indebtted to the captains, crews, technicians, and scientists on board for each of the 6 research expeditions in which I have participated during these 6 years. Not only did these expeditions and their participants afford the samples that are the basis of this dissertation, but they also taught me more than any class ever could. Special mentions to Sarah Seabrook, Art Spivack, Dennis Graham, Demian Saffer, April Abbott, Min Luo, Neville Palmer, Jess Hillman, Ann Cook, and Orest Kawka.

I am grateful to my labmates through the years, Rick Berg, Theresa Whorley, Claire McKinley, Brendan Philip, Romina Centurion, Taylor Walton, Reese Miller, and Man-Yin Tsang, for their support and friendship in the lab, at sea, and in life. I am particulary thankful to have learned so much from Theresa Whorley, who introduced me to the laboratory techniques applied throughout this dissertation and who mentored me with unmatched kindness and patience during my first years in graduate school.

Lastly, I owe a huge thanks to my friends and second-families, past and present, who have made this whole journey (and life) worthwhile: Angie, Don, and Kimm Howard, Colleen Wagner, Maddie O'Nan, Tyler DeWitt, Chandra Greenberg, Sean Gallivan, Laurenz Boettger, Korey Verhein, Evan Lahr, Amy Wyeth, Laura Moore, Natalie Kellogg, and many more. And to my partner, Will Wagner, thank you for everything; I can't wait for our next chapter.

Chapter 1. INTRODUCTION

1.1 MOTIVATION

Subduction zones are complex, dynamic systems that shape the Earth upon which we live. A simplified picture of subduction depicts the collision of two tectonic plates where the denser (oceanic) plate descends beneath the overriding (continental) plate along a megathrust fault (**Fig. 1.1**). Portions of the megathrust support stable sliding of the plates past one another, resulting in slow, aseismic "creeping" motion. In other zones, the plates are strongly coupled together such that elastic stress builds until eventual seismic release during an earthquake. At the trench of many subduction zones, incoming sediments are scraped off and accreted onto the overriding plate, forming an accretionary wedge. At others, the incoming sediments are subducted or overlying material is eroded and added to the subducting plate. In both accretionary and erosional subduction zones, as the subducting plate descends deeper, partial melting of the overlying mantle wedge fuels magmatism along a volcanic arc. These primary subduction zone processes mediate global heat and elemental cycling, drive changes in climate, power plate tectonic movement, and pose significant earthquake, tsunami, and volcanic hazards to dense population centers along coastlines.

In the past few decades, intense study and monitoring of subduction zones and megathrust slip, paired with improved instrumentation and increased computing power, have revealed a wide range of physical and behavioral characteristics that extend beyond early observations. One such finding is the recognition of a spectrum of megathrust slip behavior that spans the range from aseismic creep to fast earthquakes, including tremor, low frequency earthquakes, and slow slip events (e.g., Peng and Gomberg, 2010; Sacks et al., 1978; Schwartz

and Rokosky, 2007). While not fully understood, the mode of megathrust slip is thought to be dictated by many factors, including convergence rate and obliquity, incoming sediment thickness and plate roughness, and the age, composition, and thermal state of the subducting and overriding plates (e.g., Bürgmann, 2018; Wallace, 2020). Likewise, the presence of fluid and the occurrence of high pore fluid pressure are recognized as primary players in many subduction zone processes, including fault mechanics and slip behavior (e.g., Hubbert and Rubey, 1959, Liu and Rice, 2007; Moore and Vrolijk, 1992, Saffer and Tobin, 2011).

Fluids enter subduction zones as both pore water (fluids that occupy the interstitial spaces of sediments and basaltic crust), and as chemically bound water (fluids incorporated into hydrous minerals). The fate of fluids that enter subduction zones falls into three general categories, principally governed by permeability. Some of the fluid exits the system via diffuse flow through matrix sediments, some is channeled to the seafloor along conduits of higher permeability such as the megathrust and splay faults in the wedge, and some remains trapped and is carried to depth. Focused fluid expulsion supports benthic ecosystems, gas hydrate reservoirs, and causes geochemical and thermal anomalies at seafloor seeps (e.g., Levin, 2005; Suess, 2014). Progressive fluid-rock reactions and pore fluid pressure fluctuations with depth impact large- and small-scale fault strength, frictional velocity dependence, and slip behavior (e.g., Moore and Saffer, 2001; Scholz et al., 1998). Deeper still, 5-20% of the fluid is incorporated into the overlying continental crust and mantle, triggering arc volcanism (Peacock, 2004). Hence, fluids impact subduction zone processes at all depths and scales (Moore and Vrolijk, 1992). Importantly, the inverse is also true: tectonic forcing affects fluid pressure and flow at all depths and scales by mediating pore volume and permeability (Neuzil, 2003). While a complex interweaving of fluid and mechanical processes has long been recognized, the nature, timing, and

efficiency of fluid drainage and thus the spatial distribution of pore pressure at individual subduction zones remain incompletely understood, as do the links between the evolution of pore pressure and fluid flow with slip behavior.

This dissertation comprises three studies that explore fluid sources, permeability and fluid migration pathways, and pore fluid pressures in the outer forearc of two subduction margins: the Hikurangi margin, offshore of New Zealand, and the central Cascadia margin, offshore of western North America. Using visual, geophysical, and chiefly geochemical methods, these studies serve to advance our understanding of the interrelationship between mechanical and hydrogeologic processes in subduction zones.

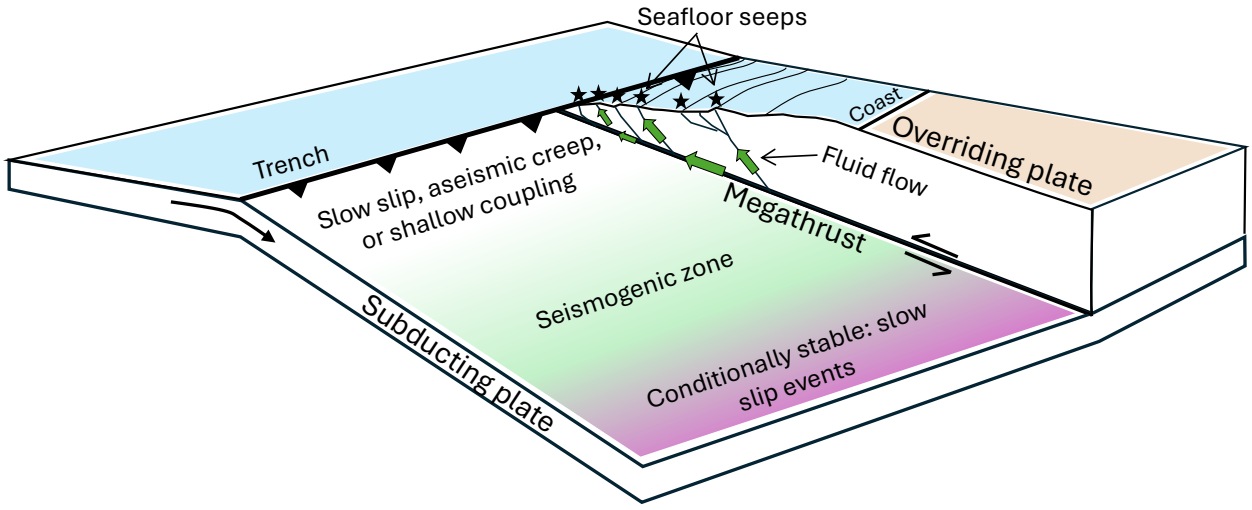

Figure 1.1. Diagram of a shallow subduction zone highlighting slip domains and fluid expulsion. Adapted from Bartlow et al., (2021); Bilek and Lay, (2002); Saffer and Tobin, (2011).

1.2 Background: Hydrogeology of Subduction Zone Outer Forearcs

The volume of pore water and chemically bound water entering subduction zones is dependent on the thickness and composition of incoming sediments, the geothermal gradient, and the hydration state of the oceanic crust (e.g., Kastner et al., 1991; Peacock, 2004). Tectonic compression and rapid burial beneath the overlying wedge expel sediment pore water via

porosity reduction. Consolidation decreases with increasing depth such that this process is the dominant fluid source in the upper 5-7 km (Moore and Vrolijk, 1992; Moore and Saffer, 2001; Saffer and Tobin, 2011). As temperature and pressure increase with depth, chemically bound water is released as hydrous minerals are dehydrated. The largest dehydration-derived shallow fluid source in most subduction zones is the transition from smectite to illite, which reaches peak fluid production at 60 – 150 ˚C (e.g., Pytte and Reynolds, 1989; Kastner et al., 1991), producing fluid in proportion to the amount of smectite present. The transformation from Opal-A to quartz constitutes an additional shallow source, reaching completion by 100 ˚C (Behl and Garrison, 1994). Farther landward, metamorphic dehydration of mafic and metasedimentary rocks (e.g., breakdown of lawsonite and chlorite minerals in basaltic crust; metapelite dehydration), followed by ultramafic rocks (e.g., serpentinized mantle) at even higher temperatures and pressures, provide additional fluid inputs deep within the system (e.g., Condit et al., 2020; Fagereng et al., 2018; Stern, 2002).

To reach the seafloor, fluids sourced from porosity reduction and mineral dehydration traverse the wedge via diffuse intragranular flow and via focused flow along permeable conduits (e.g., Carson and Screaton, 1998; Moore and Vrolijk, 1992). Diffuse flow through low-permeability wedge sediments is slow and pervasive, without significant seafloor expression. Fault zones, permeable sediment strata (e.g., uncemented sands), and the underlying basement are often characterized by higher permeabilities and can host focused fluid transport at higher rates (e.g., Lauer and Saffer, 2012; Solomon et al., 2009; Sun et al., 2020). Seafloor seeps are the surface expression of focused fluid migration from depth, often characterized by the presence of benthic macrofaunal and microbial communities, acoustic signatures (water column bubble plumes, high seafloor backscatter), authigenic mineral assemblages (carbonate, barite), gas

hydrate reservoirs, and geochemical and heat flow anomalies (e.g., Levin, 2005; Suess, 2014). Seeps often coincide with faults that extend to the plate boundary and have been found to expel fluids sourced from the deep wedge, along the megathrust, and within the underthrust sediments (**Fig. 1.1**). Thrust faults, including the megathrust itself (e.g., Silver et al., 2000; Solomon et al., 2009), normal faults (e.g., Ranero et al., 2008), and strike slip faults (e.g., Tobin et al., 1993; Philip et al., 2023) have all been documented to efficiently transport fluid from depth to the seafloor. The importance of focused flow along different conduits varies between subduction zones; drainage along the megathrust is thought to be more important at accretionary margins, while upper plate normal faults may host more fluid flow at non-accretionary margins (Kastner et al., 2014; Saffer and Tobin, 2011; Ranero et al., 2008).

Suprahydrostatic pore fluid pressures (overpressures) develop when fluid production outpaces diffuse and focused fluid drainage. Fine-grained wedge and underthrust sediments have low permeability, which is reduced further by physical compaction and chemical cementation (e.g., Spinelli et al., 2004). Hence, near-lithostatic fluid pressures can build as sediments are compacted and dehydrated while efficient drainage is impeded by low permeability conditions (e.g., Neuzil, 1995). Evidence for elevated pore fluid pressures along the megathrust and within surrounding sediments comes from direct and indirect observations as well as numerical models. Measurements and long-term monitoring at boreholes exhibit transient elevated pressures (e.g., Davis et al., 2023 and references therein). Active mud volcanism at the seafloor on subduction zone forearcs (e.g., Kopf 2002) and extensional veining in exhumed subduction thrust assemblages (e.g., Fagereng et al., 2018) provide further evidence of locally enhanced fluid pressures. Geophysical observations of high-amplitude, negative-polarity reflections (e.g., Ranero et al., 2008; Bangs et al., 2009; Bell et al., 2010), zones of low P-wave velocity and high

Vp/Vs (e.g., Eberhart-Philips and Bannister, 2015; Park et al., 2010; Yarce et al., 2021), and high conductivity/low resistivity data (Chesley et al., 2021; Heise et al., 2017) have been interpreted as abundant fluid content or elevated fluid pressure. Further, calculations of porosity, fluid pressure and effective stress from seismic velocity structure indicate elevated pore pressure (Arnulf et al., 2021; Kitajima and Saffer 2012; Tobin and Saffer 2009). Hydrologic modeling (Lauer and Saffer, 2012; Ellis et al., 2015; Sun et al, 2020) also predicts high pore pressures when the permeability of fault zones (and therefore efficient drainage) is limited.

The occurrence of pore fluid overpressures has long been known to reduce normal stresses to effective values, where effective normal stress is the applied normal stress minus the pore fluid pressure (e.g., Rice and Cleary, 1976). This in turn reduces the frictional shear strength of fault zones, i.e., the critical value of shear stress required to initiate slippage is reduced as fluid pressures increase (Hubbert and Rubey, 1959). Elevated pore fluid pressures also impact the sliding stability of faults; the reduction of effective normal stress may promote a conditionally stable (rather than unstable) frictional regime (Scholz, 1998). Thus, the spatial variability of fluid overpressure has frequently been invoked to explain changes in slip behavior with depth on megathrust faults (e.g., Moore and Saffer, 2001; Saffer and Tobin, 2011). On the shallow megathrust, it is hypothesized that overpressures prevent stick-slip behavior and instead promote aseismic slow slip, very low frequency earthquakes (VLFE), and tremor (e.g., Tobin and Saffer, 2009; Kitajima and Saffer, 2012). Decreased fluid abundance and increased effective stress with depth may then play a primary role in the transition from shallow aseismic to deeper seismic deformation (Ranero et al., 2008; Saffer and Tobin 2011; **Fig. 1.1**).

Given that measurements of fluid flow and fluid pressure conditions are relatively rare and often temporally static, the role of fluid pressure variations over time in the earthquake cycle

remains poorly constrained. It has been suggested that the transient accumulation and release of fluid pressure help govern slip nucleation and recurrence (Sibson, 1990). In a process referred to as “fault-valving,” shear failure brought on by the accumulation of shear stress and/or fluid pressure temporarily increases fault permeability and opens fluid migration pathways (Sibson 1990). As a result, fluid discharge is enhanced and fluid pressures reduced until the fault reseals and fluid pressures begin to re-accumulate. When overpressures are restored, the next failure episode can occur (Sibson and Rowland 2003). Classic evidence of transient changes in permeability and fluid flow along fault zones includes observations of changes in groundwater level and surface discharge following earthquakes (e.g., Roeloffs, 1996), structural and mineral textures along faults that indicate episodic cracking and healing (e.g., Hickman 1995), and observations of rapid seepage that require either focusing of fluid from a large area or transient fluid storage and release (e.g., Bekins and Screaton, 2007; Saffer and Bekins, 1998). More recently, long-term borehole monitoring has shown that flow rate and geochemical transients correlate with slip events (Solomon et al., 2009), and several lines of geophysical evidence including the evolution of earthquake focal mechanisms (Warren-Smith et al., 2019), Vp/Vs and shear wave splitting delay times (Zal et al., 2020), and repeating earthquakes (Shaddox & Schwartz, 2019) through the slip cycle support this model.

In addition to the impact of pore fluid pressure on effective stress and therefore fault strength and stability, fluids and fluid-rock reactions also influence the physical and mechanical properties of solids with implications for fault strength and stability (e.g., Hickman et al., 1995). Fluid-assisted cementation, hydrothermal alteration, and gas hydrate formation may rapidly and significantly reduce porosity and permeability along faults (e.g., Brantley et al., 1990; Saishu et al., 2017). In general, porosity reduction and cementation are thought to increase fault strength

and promote velocity-weakening behavior (i.e., frictional resistance decreases with increasing slip rate), encouraging stick-slip style deformation (Moore and Saffer, 2001; Scholz, 1998). These processes are also likely to generate pressure seals, an essential component of the fault-valve model (Sibson, 1990). Likewise, mineralogical changes resulting from fluid-rock reactions can impact fault strength (e.g., when strong feldspars are replaced by weak phyllosilicates; Wintsch et al., 1995) and stability (e.g., the replacement of clays with zeolites, carbonate, and quartz may promote velocity-weakening behavior; Moore and Saffer, 2001).

In summary, fault zone hydrogeologic and mechanical processes are intimately linked. Porosity and permeability, fault strength, and deformation style are dynamic properties that evolve with mineral assemblage, displacement, stress state, and pore fluid pressure, and thus evolve with depth and over time. Hence, knowledge of the hydrogeologic conditions of the plate boundary and surrounding sediments, namely the fluid inputs, permeability and fluid migration pathways, fluid flow rates, and pore fluid pressures, is required to better understand and predict the timing and nature of fault slip at subduction zones.

1.3 Methods: Assessing Fluid Sources and Flow Rates Using Pore Water Geochemistry

The chemical and isotopic composition of the upwelling pore water in subduction zone forearcs is often distinct from seawater (e.g., Kastner et al., 1991; 2014). While shallow, compaction-derived pore fluids are of seawater origin, chemical reactions, solute diffusion along concentration gradients, advection along pressure gradients, and mixing with fluids of other sources (e.g., dehydration-derived fluids) alter their nature and composition during early diagenesis (e.g., Berner, 1980). Proceeding over time and with increasing depth, these processes

produce chemical and isotopic signatures indicative of the origin, transport path, and rate of flow of fluids. Pore fluid chemistry provides direct information on fluid sources and fluid flow rates, which in turn can be used to infer the permeability architecture, fluid drainage efficiency, and the development of pore fluid overpressure in subduction zone forearcs.

Common techniques for sampling sediments include conventional gravity- and piston-coring of the upper ~15 m of the sediment column, directed push coring using a remotely operated vehicle, and deep core recovery during scientific ocean drilling. Pore fluids are extracted from sediment cores by squeezing (e.g., Reeburgh, 1967), Rhizon sampling (e.g., Seeberg-Elverfeldt et al., 2005), or centrifugation (e.g., Schulz et al., 1994); the method chosen depends on analytes of interest, volume of pore water required, porosity/permeability of the sediment, and financial budget (e.g., Schulz and Zabel, 2006). Sampling of pore fluids is also accomplished using osmotic pumps in borehole hydrologic observatories (OsmoSamplers; Jannasch et al., 2004; Wheat et al., 2003; Solomon et al., 2009) and seafloor fluid flow meters (Solomon et al., 2008, Tryon et al., 2001), using peepers (Hesslein, 1976), and using Isobaric Gas Tight (IGT) and Major samplers (Seewald et al., 2001; von Damm et al., 1985). Successful recovery of fluid samples using these and other techniques, followed by proper storage and careful laboratory analysis, allows for the determination of the composition of the pore fluid and inferences of fluid sources and migration pathways. Subsequently, reactive-transport modeling of fluid compositions with depth (e.g., from sediment core samples) or tracer concentrations over time (e.g., from fluid flow meter samples), allows for quantification of fluid flow rates. The primary considerations of these two undertakings (inference of fluid sources and flow pathways, and estimation of fluid flow rates) are summarized in the remainder of this section.

The breakdown (i.e., catabolism) and oxidation of sedimentary organic matter by marine microbes cause early and clear changes in the pore water chemistry (e.g., Berner, 1980; Burdige, 2006; Froelich et al., 1979). High biological activity in the overlying water, terrigenous input of particulate organic carbon, and relatively shallow water depths result in rapid accumulation of organic-rich sediments on continental margins (e.g., Hedges and Keil, 1995). To metabolize this organic matter, oxidants are used in a sequential order corresponding to redox potential and thus energy efficiency, resulting in a depth zonation of reactions (termed the "redox ladder"), and characteristic pore water changes (e.g., Burdige, 1993; Froelich et al., 1979; McKinney and Conway, 1957). First, aerobic respiration (oxidation of organic matter by dissolved O_2), which yields the most free energy, consumes oxygen and produces CO_2. Once oxygen is depleted, denitrification, followed by Mn(IV) and Fe(III) reduction, and sulfate (SO_4^{2-}) reduction occur in the suboxic and anoxic zones (Froelich et al., 1979; Burdige, 2006). Along with reduced metals and sulfur species, this series of reactions releases bicarbonate into the pore water, increasing alkalinity. Below the zone of sulfate reduction, organic matter is consumed as isotopically-light methane is produced via CO_2 reduction and acetate fermentation (e.g., Claypool and Kaplan, 1974). Between the sulfate-reducing zone and methanogenic zone, methane migrating upward is removed via the anerobic oxidation of methane (AOM) in the sulfate-methane transition zone (SMTZ), resulting in the formation of sulfide and bicarbonate and a dissolved inorganic carbon pool depleted in ^{13}C (e.g., Boetius et al., 2000; Iversen and Jørgensen, 1985).

Further pore water alteration results from indirect consequences of the above biogeochemical reactions. The production of alkalinity during sulfate reduction (including both sulfate reduction of organic matter and AOM), leads to the precipitation of authigenic calcium carbonate phases (e.g., Suess, 1979). Carbonate mineral precipitation removes calcium and

alkalinity from the pore water, as well as Mg, Sr, Mn, Fe, which can substitute for Ca in the mineral structure (e.g., Fantle et al., 2020). The depletion of sulfate results in the undersaturation and dissolution of barite, releasing Ba into the pore water; reprecipitation of barite then occurs when upward-migrating pore water encounters sulfate-rich fluids (e.g., Solomon and Kastner, 2012; Torres et al., 1996a; 1996b). Weathering of reactive silicates (ash and continentally-derived material) is enhanced below the SMTZ by the excess CO_2 generated during methanogenesis (e.g., Wallmann et al., 2008; Solomon et al., 2014; Torres et al., 2020). Silicate weathering produces dissolved cations (e.g., Si, Ca, K, Sr, Mg) and alkalinity, influencing the $^{87}Sr/^{86}Sr$ of the pore water, buffering the pH, and enabling carbonate precipitation and burial (Solomon et al., 2014; Torres et al., 2020). Under specific temperature and pressure conditions, methane produced below the SMTZ can form hydrate (a crystalline solid comprising water and gas), preferentially taking up heavy isotopes of oxygen and hydrogen. As such, the dissociation of methane hydrate either in situ or upon sample recovery, releases fresh water, resulting in negative pore water solute excursions and enrichment in ^{18}O and deuterium (e.g., Hesse and Harrison, 1981).

With increasing depth, fluid-rock (fluid-sediment) interactions at high temperatures and pressures continue to make the pore water chemically and isotopically more “exotic” (Kastner et al., 2014). In response to changing conditions (e.g., temperature, pH, dissolved ion concentrations) cations that occupy the interlayer spaces of clay minerals (e.g., B and Li) can exchange with those in solution (e.g., Burdige, 2006). Similarly, cations adsorbed to the charged surfaces of clays can desorb and exchange, acting as a source or sink to the pore water. The recrystallization (dissolution and reprecipitation of a mineral towards a more stable polymorph) of biogenic and authigenic carbonates takes up Mg, Mn, and Fe while releasing Sr (Fantle et al.,

2020; Walter et al., 1993). Fresh water is added to the pore water when opal-A transforms to opal-CT and quartz (Kastner et al., 1977; 1991). Greater volumes of dehydration-derived fluids are added to the pore water when hydrous clays (especially smectite) are transformed and lose interlayer water (e.g., Moore and Vrolijk, 1992). Tell-tale signatures of these transformations include diluted pore water Cl, decreased $\boldsymbol{\delta}$D and increased $\boldsymbol{\delta}^{18}$O, decreased K, elevated Si, and enrichment in elements that were sorbed in the interlayer space (e.g., B and Li) (e.g., Kastner et al., 1991; 2014). Signatures of fluid interaction with and alteration of upper oceanic crust include elevated Ca and low (non-radiogenic) $^{87}Sr/^{86}Sr$ (e.g., Elderfield et al., 1999; Teichert et al., 2005). Thermogenic methane and higher molecular weight hydrocarbons (e.g., ethane, propane, butane) form at high temperatures and are added to upwelling fluids (e.g., Bernard et al., 1977; Milkov and Etiope, 2018). In general, the following characteristics are typical of deeply-sourced fluids (Kastner et al., 2014): low Cl and K, high Si, B, and Li, the presence of thermogenic hydrocarbons, and anticorrelated oxygen and hydrogen isotope ratios.

The diagenetic reactions described above uniquely alter the composition of pore fluids, imparting chemical and isotopic signatures indicative of the fluid source (i.e., depth and temperature of formation) and transport path (i.e., subsequent changes experienced) from depth to the site of sampling. Additionally, changes in fluid chemistry brought on by early diagenesis provide a means to quantify fluid flow rates. Changes in solute concentration observed with depth and over time are a function of advection, diffusion, and reaction. Thus, if two of these components are known or well parameterized, the other can be estimated analytically or modeled numerically (e.g., Boudreau, 1997). Modeling of fluid flow rates is easiest for an unreactive solute (e.g., Cl or an unreactive tracer added to the system) where diffusion rate is calculated as a function of temperature, solute, and tortuosity, and reaction is set to zero. When reaction is non-

zero, its rate can be classified according to a first- or higher-order rate law (e.g., Berner, 1964; Boudreau, 1997) so that advection is the free parameter. Independent measurements of fluid flow rate (e.g., from modeling of heat flow data, tracking bubbles and particles expelled at seeps, and using fluid flow meters) supplement and verify rates estimated by advection-diffusion modeling (e.g., Hutnak et al., 2008; Rona and Trivett, 1992; Solomon et al., 2008).

Fluid flow rate estimates within fault intervals in boreholes and at fault-hosted seafloor seeps reflect fault zone permeability and pressure gradients, and thus are central to understanding and quantifying fluid budgets and the distribution of overpressures in subduction zones. In addition, at diffuse sites, fluid flow rates can serve as indicators of secular strain, providing constraints on offshore interplate coupling which is essential for the assessment of seismic and tsunami hazards. Long-term flow rate measurements reveal both background flow conditions and can record the hydrologic response to deformation, informing on the evolution of fault zone permeability, fluid pressure conditions, and the overall state of strain in the outer forearc (e.g., Brown et al., 2005). Hence, along with knowledge of fluid sources, measurements of flow rate at focused and diffuse sites are essential to make broad-scale inferences on hydrogeologic conditions, calculate fluid and solute fluxes, and constrain water budgets.

1.4 Dissertation Summary

This dissertation comprises three studies in which pore fluid chemical compositions and fluid flow rates are reported and interpreted in the context of broad-scale subduction zone processes. The three studies are briefly summarized below.

Chapter 2 reports on pore water from sediment cores and heat flow determinations at seep sites on the slope of the northern and southern Hikurangi margin, offshore of New Zealand. The

primary results are that fluid flow rates and heat flow are relatively low, and that seep fluid compositions are indicative of shallow, compactive sources. Hence, no evidence of appreciable drainage of the plate boundary or underthrust section along fault zones is observed. These observations suggest that fault zones from the deformation front to the upper slope are relatively impermeable at depth. As a result, fluids may remain trapped at depth, causing high pore pressures along the plate boundary, reducing effective stress and likely influencing the occurrence of slow slip.

Chapter 3 documents the hydrologic response to a large slow slip event (SSE) that occurred at the northern Hikurangi margin in early 2019 using continuous records of fluid flow rate collected via benthic fluid flow meters over a 2-year period. The first order results of this study are that net flow polarity varies across strike, and that transient flow pulses temporally correlate with the SSE. Net seafloor fluid flow rates suggest contrasting secular strain across strike: dilatational on the lower-slope and compressional on the mid-slope. These observations are consistent with slip on the shallow megathrust and locking in the slow slip source region in the inter-SSE period. Downward flow rate transients at diffuse sites on the lower-slope during the SSE may indicate shallow slip propagates along a splay fault or could result from seamount subduction. At focused flow sites, transients reflect non-tectonic seep processes and possibly shallow permeability changes, but convincing evidence of wide-spread fault-valving or transport of deeply-sourced fluids to the seafloor during the monitored period is not observed.

Chapter 4 presents a detailed investigation of fluid chemistry and heat flow at Pythia's Oasis Seep on the Cascadia margin. Results confirm persistent, rapid drainage of highly altered fluids at two emission sites within the seep area. The chemical composition of the venting fluids indicate a component of the fluid is sourced from within the subducting sediment section below

the megathrust (≥4 km below seafloor) at temperatures of ~170–250 ˚C. Sustained, rapid fluid discharge at Pythia's Oasis is most likely permitted by a combination of poor drainage (and resulting elevated pore pressures) beneath the outer wedge, and a highly permeable and interconnected strike slip fault (the Alvin Canyon Fault, ACF) funneling fluid from a large area vertically and along strike. These hydrogeologic conditions may play an important role in the regulation of pore fluid pressure and effective stress across and along strike, and thus may have broad impacts on margin structure and megathrust locking. Long-distance fluid flow along the ACF in the mid-slope region of the Cascadia margin also results in significant fluxes of B, Li, Sr Ca, Si, Mn, and Fe at Pythia's Oasis. Particularly, the B and Sr fluxes at Pythia's Oasis rival those at high-temperature hydrothermal vents and low-temperature ridge-flank hydrothermal sites. If similar high-volume seeps exist in Cascadia and elsewhere, the transfer of fluids to the ocean through seafloor seeps may influence marine geochemical cycles.

Chapter 2. GEOCHEMICAL AND THERMAL CONSTRAINTS ON THE HIKURANGI SUBDUCTION ZONE HYDROGEOLOGIC SYSTEM AND ITS ROLE IN SLOW SLIP

This chapter is modified from the version submitted to *Geochemistry, Geophysics, Geosystems* in July 2024 (revised in December 2024) with the following author list:

I. Aylward, E. A. Solomon, M. E. Torres, R. N. Harris

2.1 ABSTRACT

Fluid generation and migration regulate the development of pore fluid pressure, which is hypothesized to influence the occurrence of slow slip events at subduction zones. Seafloor seep sites present the opportunity to directly sample fluids flowing through the accretionary wedge and assess the hydrogeologic conditions of the outer forearc. We present heat flow measurements and pore water geochemistry from sediment cores collected at fault-hosted seep sites on the southern and northern Hikurangi margin, offshore the North Island of New Zealand. These measurements span the deformation front to the shelf break. Along the northern margin, heat flow data do not show anomalies that can be obviously attributed to the discharge of warm fluids. Pore fluid compositions indicate that seep fluids originate from compaction within the uppermost wedge. Reactive-transport modeling of pore water solute profiles produces fluid flow rate estimates ≤ 2 cm/yr. Shallow fluid sources and low discharge rates at offshore fault-hosted seeps suggest that the sampled fault zones are characterized by low permeability at depth, preventing efficient drainage of the megathrust and underthrust sediments to the seafloor. These results provide additional evidence that the northern Hikurangi margin plate boundary is associated with high pore fluid pressures that likely act as a control on slow slip activity.

2.2 Plain Language Summary

Subduction zone faults can produce devastating earthquakes and tsunamis when tectonic plates slip quickly past one another. The plate boundary (sometimes called the megathrust) can also slip slowly without generating seismic shaking during slow slip events. The magnitude of pore fluid pressure along the megathrust and in the surrounding sediments, controlled in part by the ability or inability of fluids to drain from the megathrust zone, is thought to impact the occurrence of fast versus slow slip. We investigate fluid drainage along the Hikurangi subduction zone offshore of New Zealand by sampling seafloor seeps, locations where fluids channeled along fault zones are expelled at the seafloor. Our heat flow and pore fluid geochemistry results suggest that fluids expelled at the sampled seeps are sourced from shallow sediment depths and are discharging at relatively low rates. We find no evidence that fault zones offshore of the southern and northern Hikurangi margin allow efficient drainage of fluids from deep within the subduction zone to the seafloor. These results support the hypothesis that high pore fluid pressures exist along the megathrust and in surrounding sediments, likely influencing the timing and style of fault slip.

2.3 Introduction

Geodetic and seismological observations at subduction zones over the last few decades have revealed a range of modes by which stress is released on the plate boundary, including episodic slow slip events (SSEs). SSEs occur at rates intermediate between fast, seismic slip that generates earthquakes (centimeters to meters per second) and aseismic creep at plate motion rates (centimeters per year) (e.g., Dragert et al., 2001; Hirose et al., 1999; Peng & Gomberg, 2010; Sacks et al., 1978; Schwartz & Rokosky, 2007). Offshore the east coast of New Zealand's

North Island, where the Pacific plate subducts beneath the Australian plate, the Hikurangi subduction zone (HSZ) hosts frequent, well-studied SSEs (Wallace, 2020 and references therein). The southern Hikurangi margin is characterized by deep (>30 km), long (>1 year), infrequent SSEs (every ~5 years) that occur at the thermally-controlled down-dip transition from brittle to ductile behavior (McCaffrey et al., 2008; Wallace, 2020). In contrast, the northern margin exhibits shallow (<15 km), short (<~1 month), frequent events (every 1-2 years) (Wallace, 2020). It is hypothesized that shallow SSEs in the northern HSZ are enabled by conditional fault zone stability arising from low effective normal stress linked to elevated pore fluid pressure (e.g., Bangs et al., 2023; Bell et al., 2010; Gase et al., 2023; Saffer & Wallace, 2015; Warren-Smith et al., 2019). Thus, characterizing the pore fluid pressure distribution in the source region of slow slip is recognized as an important step toward understanding SSEs and subduction zone fault behavior (e.g., Arnulf et al., 2021; Bell et al., 2010; Ellis et al., 2015; Sun et al., 2020a).

The development of pore fluid pressure in marine sediments is regulated by the balance of fluid sources (inputs) and fluid flow (outputs). Pore fluid overpressure (i.e., pore fluid pressure in excess of hydrostatic pressure) is common in subduction zones due to rapid mechanical loading of sediment and the release of mineral bound water that outpace drainage through low permeability matrix sediments (e.g., Ellis et al., 2015; Gamage & Screaton, 2006; Ranero et al., 2008; Sun et al., 2020a). Elevated pore fluid pressure reduces effective normal stress, which in turn reduces fault strength and can promote conditions favorable for slow slip. However, the plate boundary and faults within the forearc often exhibit higher permeability than the matrix sediments, thereby providing pathways for focused fluid flow and drainage of both underthrust and wedge sediments (e.g., Moore et al., 1991; Moore & Vrolijk, 1992; Saffer & Tobin, 2011).

Drainage of fluids along fault zones relieves overpressure, leading to an increase in effective stress and fault strength, which can promote stick-slip behavior. Thus, the pore pressure distribution, and its contribution to fault strength and stability, along the plate boundary are dictated by fluid sources and the permeability of the plate boundary and wedge, i.e., the ability of faults to support appreciable rates of fluid flow (e.g., Lauer & Saffer, 2012; Saffer & Bekins, 1998; Sun et al., 2020a).

Seep sites on the outer forearc of subduction zones often coincide with faults that extend to the plate boundary (Kluesner et al., 2013; Park et al., 2002; Watson et al., 2020), and as such, are potential sites of fluid discharge from within the wedge and along the megathrust (Hensen et al., 2004; Martin et al., 1996; Mottl et al., 2004; Philip et al., 2023; Ranero et al., 2008; Tryon et al., 2010). Deeply-sourced fluids have compositions that are distinct from seawater as a result of diagenetic reactions that proceed with increasing temperature and pressure (Kastner et al., 2014). These reactions uniquely change the fluid composition, providing a signature that is often maintained during transport from depth to expulsion at seafloor seeps. In this way, concentrations of various solutes in seep fluids are indicative of the temperature/pressure regime from which the fluid was sourced, providing information on the region of the subduction zone that is actively draining. Further, numerical modeling of seep pore water solute profiles yields field-based fluid flow rate estimates that can be compared to margin-scale model predictions and can indicate the efficiency of fluid drainage along fault zones. Together, the source and expulsion rate of fault-hosted seep fluids serve as valuable indicators of the permeability of fault zones and pore fluid pressure at depth.

Here we present the results of a systematic and comprehensive field campaign that includes 90 heat flow measurements and sampling of pore fluids from 33 piston, gravity, and

push cores spanning the deformation front to the upper slope at the southern and northern HSZ. We determine heat flow, fluid flow rates, and fluid compositions at seafloor seeps associated with faults to better understand the permeability architecture of the forearc and make inferences of the pore fluid pressure conditions in the region of shallow slow slip at the northern HSZ.

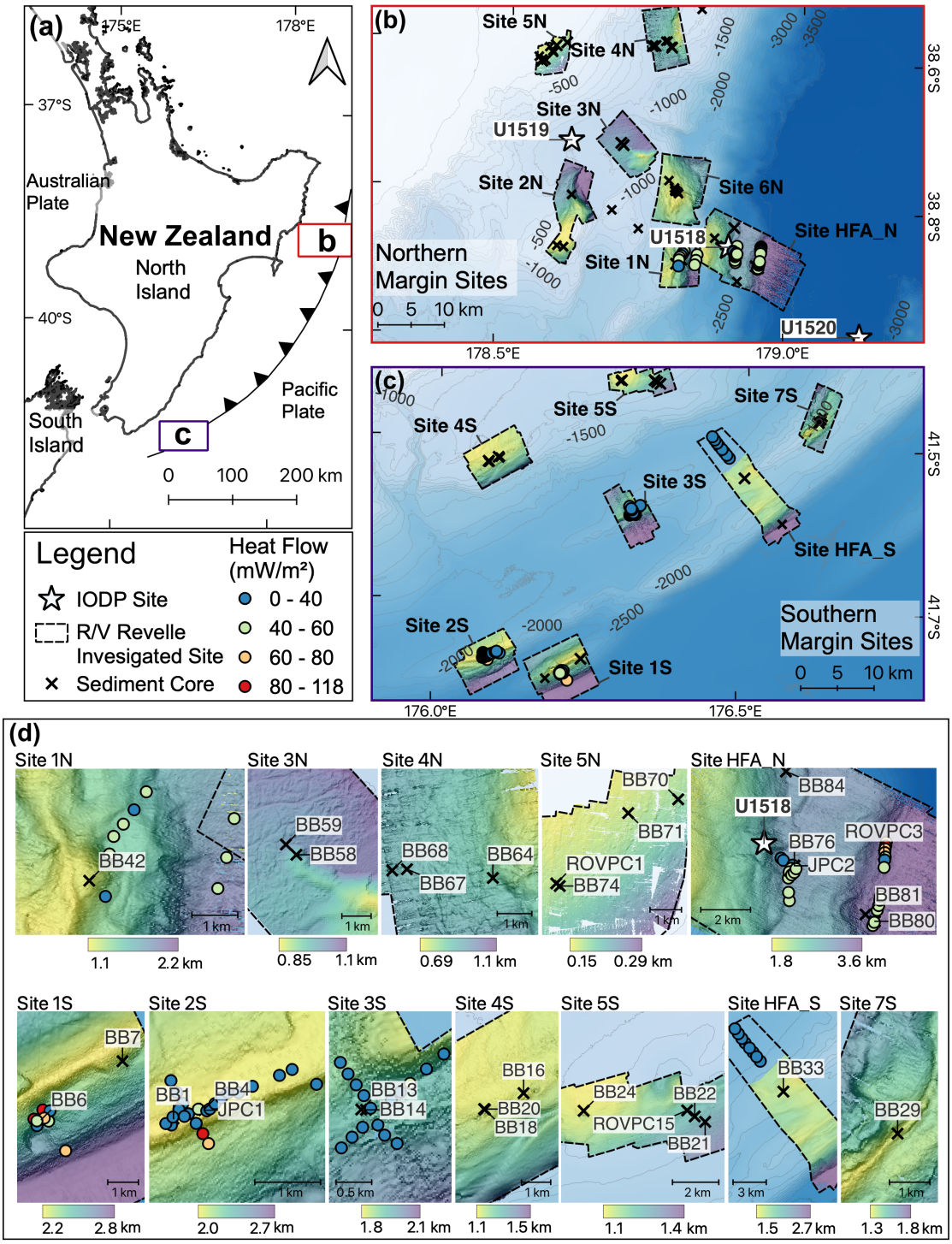

Figure 2.1. Regional and site-specific maps with coring and heat flow locations.
(a) Regional map of New Zealand's North Island. Black saw-toothed line shows deformation front. (b)(c) Locations of all collected cores, heat flow measurements using 3.5-m probe, and IODP Sites U1518, U1519 and U1520. 500-m bathymetric contours are labeled. (d) Zoom-in of the sites, 33 cores, and 90 heat flow measurements that are the focus of this study. Color-bars show bathymetry (km).

2.4 METHODS

2.4.1 *Sample collection*

During the 38-day SAFFRONZ (Slow-slip and Fluid Flow Response Offshore New Zealand) expedition on the *R/V Revelle* in early 2019 (RR1901/RR1902), we investigated 14 sites spanning from the deformation front to the upper slope offshore of the southern and northern Hikurangi margin (**Fig. 2.1**). Site selection was guided by the known distribution of seepage indicators described in Watson et al. (2020). Hydroacoustic surveys for bubble plume detection, collection of 90 heat flow measurements, and seafloor surveys using the remotely operated vehicle (ROV) *Jason* during the 2019 expedition further refined our coring locations. We specifically targeted fault-hosted sites of fluid emission, i.e., seafloor seeps located at the up-dip projections of fault zones or on seafloor ridges marking the hanging-walls of thrust systems (**Fig. 2.2**). Two piston cores, 58 gravity cores, and 19 push cores were collected for pore water geochemistry.

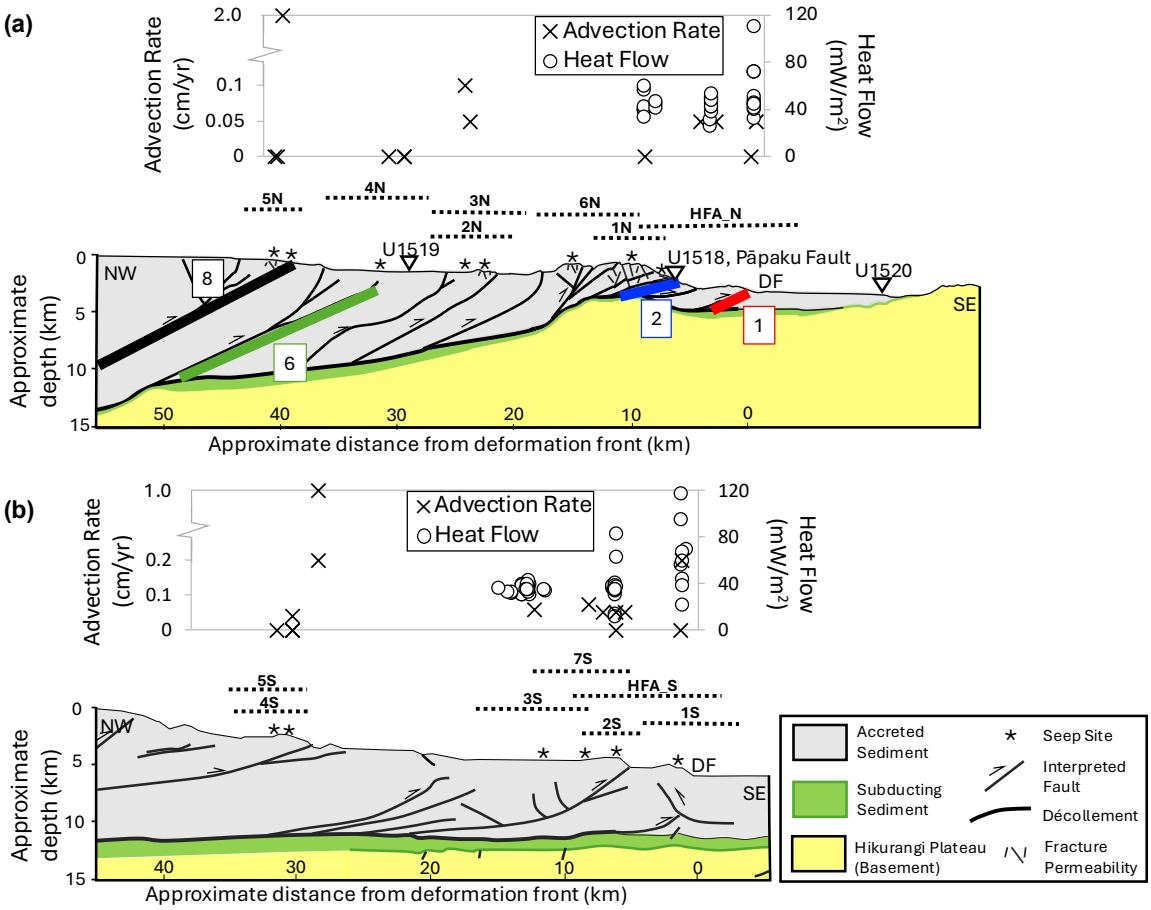

Figure 2.2. Heat flow and fluid flow rate results projected above conceptualized cross sections. Conceptualized cross sections of (a) the northern Hikurangi margin, based on Watson et al. (2020) and (b) the southern Hikurangi margin, based on the interpretations of seismic line SAHKE-01 by Bland et al. (2015). Approximate locations of our study sites are projected onto the cross sections, indicated by the dotted lines. Plots of heat flow and pore water advection rate results are also projected onto the cross sections; Y-axes are "broken" to show the spread of low advection rates. Thick colored lines in (a) reflect the four fault geometries used in the diffusive loss modeling (Fig. 2.6). IODP Sites U1518, U1519, and U1520 are shown as white triangles. Note site locations, depths, and distances from the deformation front (DF) are approximates.

Heat flow determinations were made using a "violin bow" style multipenetration heat flow probe at a nominal spacing of about 200 m near seep sites with the goal of locating areas of warm fluid discharge to guide coring and ROV operations. The probe's thermistor string is 3.5-m long and houses 11 thermistors. Once seep sites were targeted, additional heat flow

determinations were made with either a 0.6-m or 1.0-m probe on the ROV *Jason*. The ROV probes house five thermistors and measurement spacing was generally less than ~10 m. Determinations of heat flow consist of in situ measurements of the thermal gradient and thermal conductivity. Thermal conductivity was measured at most but not all sites. Where thermal conductivity was not measured it was estimated from nearby sites. All heat flow data was processed using software that allows iterative determination of the local thermal gradient and heat flux, including a Monte Carlo assessment of uncertainties (Villinger & Davis, 1987; Stein & Fisher, 2001). In total, 118 heat flow measurements were attempted with the 3.5-m probe. Of these, 90 were successful. Failed measurements were due to the inability of the probe to penetrate sediments, often attributed to authigenic carbonates at the seafloor.

Piston, gravity, and push cores were collected for pore water geochemical analysis across 14 sites. Piston cores were collected at two sites, averaging 7 m of penetration. Trigger cores (gravity cores that trigger the release of the piston upon hitting the seafloor) were collected alongside piston cores to ensure undisturbed samples of the top meter of sediment at those locations. Gravity cores were collected at all 14 sites, averaging about 3 m of penetration for successful cores. 101 gravity coring attempts were made, 58 of which were successful. 19 push cores (average recovery length of 20 cm) were collected at 8 sites using the ROV *Jason*. After collection, gravity and piston cores were immediately cut into 10-50 cm sections, capped, and stored in a cold room until further processing. Within ~24 hours, sediment was extruded at a 5 cm resolution in the top 20 cm of each core, and coarser resolution in deeper sections. Push cores were either similarly extruded in small sections or pore water was extracted using Rhizon samplers. During the extrusion process, 3 mL of sediment was collected from select samples using a cut-off syringe and placed into vials for later analysis of porosity. Extruded sediment

sections were then squeezed for pore water using Ti squeezers and hydraulic presses. Each sample was passed through a 0.2 μm syringe filter before being dispensed into bottles and preserved for a range of post-expedition chemical analyses.

2.4.2 *Pore water and sediment analyses*

Pore water salinity was measured shipboard using an optical hand-held refractometer. Alkalinity measurements were also conducted shipboard by Gran titration with HCl. Based on the profiles of alkalinity with depth, 33 cores were selected as representatives of the sites to be further analyzed on shore. Selected cores include 2 piston cores (JPC01, JPC02), 1 trigger core (JPC01_TC), 3 push cores (prefix ROVPC), and 27 gravity cores (prefix BB). **Figure 2.1** shows the locations of all collected cores with labels only for the 33 cores that are the focus of this study.

Porosity was measured at the University of Washington (UW) by weighing 3 mL sediment samples before and after drying in an oven for 24 hours at 80 ˚C. Pore water chloride concentrations were analyzed by titration with silver nitrate at UW following the method in Gieskes et al. (1991). Cl measurements were calibrated daily by comparison with at least 4 repeat analyses of IAPSO standard seawater to a precision of approximately 0.3%; reported concentrations are based on duplicate measurements of each sample. Concentrations of major (Ca, Mg, K, Na, S) and minor (B, Li, Sr, Fe, Mn, Si) elements were measured at Oregon State University using a Spectro Arcos ICP-OES, with samples diluted at 1:100 and 1:25 with a 1% and 2% nitric acid solution, respectively. Dilutions of IAPSO were used as calibration standards for the major elements. In-house standards prepared from certified reference standards were used for calibration of the minor elements. Analytical precision of major element analyses was <3%. Precision of B, Li, Fe, and Mn were <5%, and precision of Sr and Si were ≤6%. Sulfate was

measured at UW using a Perkin Elmer ICP-OES with IAPSO as the calibration standard. Sulfate analyses were only conducted for 6 sediment cores due to improper sample preservation; analytical precision was generally <5%. Ammonium was analyzed colorimetrically at UW following the method in Gieskes et al. (1991). Ammonium measurements were calibrated daily against a series of dilutions of an in-house solution prepared from certified ammonium chloride standard; analytical precision was <5% based on replicate analyses of a check standard. Analytical methods and results are included in (Aylward et al., 2024).

2.4.3 *Reactive transport modeling*

We estimate in situ reaction rates and fluid advection rates using a one-dimensional finite-difference model that solves the transient advection-diffusion equation run to steady-state (Berg, 2018),

$$\phi \frac{\partial C}{\partial t} = \frac{\partial}{\partial z}\left[\mathrm{D_s}\phi \frac{\partial C}{\partial z}\right] - \frac{\partial}{\partial z}[(\phi b + \phi v)C] \pm \phi R, \quad (2.1)$$

where C is solute concentration, t is time, z is depth, D_s is the sediment diffusion coefficient, ϕ is porosity, b is pore water burial rate, v is fluid advection rate, and R is the sum of the rates of in situ reactions.

Diffusion coefficients are calculated based on a reference diffusivity adjusted for temperature (T), salinity (S), and tortuosity (θ^2). We use the Stokes-Einstein relationship to calculate molecular diffusion coefficients,

$$D_m = \left(\frac{T}{\mu}\right)\left(\frac{\mu_r}{T_r}\right)(D_r), \quad (2.2)$$

where $\mu(T,S)$ is the fluid dynamic viscosity as a function of temperature and salinity, and μ_r is the viscosity at the reference temperature and salinity calculated following Sharqawy et al.

(2010). D_r is the reference diffusion coefficient at the reference temperature, T_r (Li & Gregory, 1974). The sediment diffusion coefficient is then,

$$D_s = \left(\frac{D_m}{\theta^2}\right), \tag{2.3}$$

where sediment tortuosity is calculated from porosity (ϕ) as (Boudreau, 1997),

$$\theta^2 = 1 - ln(\phi^2). \tag{2.4}$$

We estimate advection rates by modeling NH_4 profiles. Ammonium concentrations increase within our cored depth range and do not reach an asymptotic value, so we use NH_4 profiles from International Ocean Discovery Program (IODP) Sites U1518 and U1519 (locations shown in **Fig. 2.1b, 2.2a**) to represent background, non-seep conditions without fluid advection (v = 0). At these sites, we estimate zoned NH_4 reaction rates (R in Eqn. 2.1) with depth from the seafloor (NH_4 = 0 μM) through the upper sediments. Model input parameters (**Table A1**) include NH_4 concentrations, porosity, and temperature gradients at U1518 and U1519 from Wallace et al. (2019) and sedimentation rates from Crundwell and Woodhouse (2022). Fixing the reaction rate profiles, we can then model NH_4 profiles at a range of advection rates. Advection rates for our cores are then estimated by finding the best fit between our measured pore water NH_4 profiles with the advection models generated at the drilling sites. For both the northern and southern margin, Site U1519 is used as the reference site for cores taken on the mid- to upper-slope, and U1518 as the reference site for cores taken closer to the deformation front. This modeling assumes the U1518 and U1519 NH_4 profiles are representative of the bottom boundary concentrations and that in situ NH_4 reaction rates at the reference locations are applicable to the shallow section of seep sediments.

In addition, we estimate the solute concentration change due to diffusion during fluid transport along faults by sequentially implementing the two-dimensional model of Vasseur et al.

(1993). We first solve for temperature to compute the sediment diffusion coefficient and then solve for solute concentration. The model consists of a thin, permeable, and dipping fault that traverses a homogenous impermeable medium with a specified flow rate. Fluid is assumed to enter the base of the fault at the ambient temperature given by,

$$T = \Gamma z + T_0, \tag{2.5}$$

where Γ is the undisturbed thermal gradient, z is depth, and T_0 is the bottom water temperature. This fluid then flows upward along the fault at a specified flow rate (q), moving heat from the downdip portion of the fault and warming the updip portion of the fault. The temperature disturbance (ΔT) due to fluid flow along the fault is (Vasseur et al., 1993),

$$\Delta T(x) = \frac{Pe\ \Gamma \tan(\varphi)}{1 - Pe \tan(\varphi)} \left[h(x) - h_0 \left(\frac{h_0}{h(x)} \right)^{\frac{1}{Pe \tan(\varphi)}} \right], \tag{2.6}$$

where x is the horizontal distance, h_0 is the depth to the base of the fault at $x = 0$, $h(x)$ is the along-fault depth, φ is the fault dip, and Pe is the Peclet number. The Peclet number is the ratio of the advective and diffusive flow rates,

$$Pe = \frac{q\ \rho_f c_f}{\lambda}, \tag{2.7}$$

where q is the flow rate, λ is thermal conductivity, and ρ_f and c_f are the fluid density and specific heat, respectively, calculated as a function of pressure and temperature (Nayar et al., 2016; Sharqawy et al., 2010). The background temperature field is given by,

$$\frac{1}{\alpha} \left(\frac{\partial^2 T}{\partial x^2} + \frac{\partial^2 T}{\partial z^2} \right) = 0, \tag{2.8}$$

where α is the thermal diffusivity, and x and z are the horizontal and depth dimensions, respectively. The sides of the model are held constant at the ambient temperature (Eqn. 2.5). Temperature along the fault is then given by,

$$T_{fault} = T + \Delta T, \tag{2.9}$$

and Equation 2.8 is solved by substituting T_{fault} for grid nodes along the fault.

With temperatures in hand, the sediment diffusion coefficient (Eqn. 2.3) is known. We repeat the procedure, solving Equation 2.6 for solute concentration disturbance (ΔC) instead of ΔT, replacing $Pe = \frac{qz}{D_s}$, and solving Equation 2.8 by replacing α with D_s and T with C, the solute concentration. The background concentration gradient between the surface and the base of the fault is given by,

$$\Gamma_c = \frac{C_{base} - C_0}{z}, \tag{2.10}$$

Where C_{base} is the solute concentration at the base of the fault, C_0 is the bottom water solute concentration, and z is depth. The sides of the model are set to $C = \Gamma_c z + C_0$.

2.5 Results and Discussion

2.5.1 *Heat flow*

ROV determinations of heat flow show significantly higher values than those determined from the 3.5-m probe, but these high values appear to be associated with recent bottom water temperature variations. Because the ROV probes are relatively short, compared to the multipenetration probe, they are more susceptible to perturbations from recent bottom water temperature variations. Differences in mean heat flow values between the 3.5-m probe (mean value of 44 mW m^{-2}) and 0.6-m probe (mean value of 238 mW m^{-2}) are consistent with a change in bottom water temperature of about 0.3 ˚C over a couple of weeks prior to our measurements. Although no long-term records of bottom water temperature at our study sites exist, temperature changes of this magnitude were observed during the 2014-2015 Hikurangi Ocean Bottom Investigation of Tremor and Slow Slip (HOBITSS) seafloor geodesy campaign (Wallace et al., 2016) at a water depth of 2.4 km along the northern margin. These inferences lead us to believe

the ROV probe measurements are not suitable for detecting upward fluid advection and we do not discuss them further.

The locations and results of successful heat flow determinations using the 3.5-m probe are shown in **Figures 2.1 and 2.2**. Complete heat flow transects using the 3.5-m probe are shown in **Figures A1-A6**. The mean and standard deviation for these heat flow measurements are 44 and 17 mW m^{-2}, respectively. Sites 1N and HFA_N (**Fig. A1 and A2**) targeted splay faults near the toe of the forearc in the northern margin. Heat flow results at these sites are generally low and inconsistent with warm fluid discharge, but a relatively high heat flow value was determined at Site HFA_N near kilometer 4 of the eastern profile (**Fig. A2**). However, no seep is associated with this site; 3 ROV seafloor surveys and 6 cores during the 2019 expedition, as well as a subsequent deployment of a fluid flow meter (Aylward et al., 2023) do not reveal active seepage at site HFA_N. A possible explanation for this single anomalous value is slumping associated with deformation of the margin at this steeply-sloped site, but without additional information, it is difficult to explain this single high value. Sites 1S, 2S, and 3S (**Fig. A3-A5**) targeted seep sites along the southern margin. At Site 1S along profile A-A' heat flow values between kilometer 0.4 and 0.7 are slightly higher than average (**Fig. A3**) and near kilometer 0.4 of profile B-B' a value >100 mW m^{-2} is observed. At Site 2S, values of ~80 and 65 mW m^{-2} between kilometer 1.1 and 1.4 along profile A-A' are observed (**Fig. A4**). These high values are broadly consistent with upward fluid flow. Relatively low values of heat flow are also associated with Site 2S (**Fig. A4**). One of these values is along transect A-A' near kilometer 1 and the other along transect B-B' near kilometer 0.75. These low values may be associated with recharging of fluids due shallow gas emissions and bubble irrigation associated with the seep sites (e.g., Solomon et al., 2008).

2.5.2 *Constraints on fluid sources from pore fluid chemical profiles*

Select pore water solute profiles are shown in **Figure 2.3**; all pore water data are shown in **Figures A7 and A8**. Evident pore water deviations from seawater composition include increasing alkalinity, Si, Ba, and NH_4, and decreasing Ca, Li, and S concentrations with depth. Other solutes (K, Mg, Cl, Na, B, Sr) show near-vertical profiles that remain close to seawater concentrations. The most notable observation derived from this dataset is that Cl concentrations (**Fig. 2.3a, f**) do not show a significant negative deviation from seawater that would indicate freshening due to mineral dehydration, as has been widely documented at other margins (e.g., Brown et al., 2001; Hensen et al., 2004; Philip et al., 2023; Torres et al., 2004). The near-vertical Cl profiles suggest that the sampled seeps are not draining sediments that have undergone dehydration reactions, and thus are sourced from shallow depths. In the remainder of this section, we evaluate this inference in the context of additional geochemical and thermal data from the region.

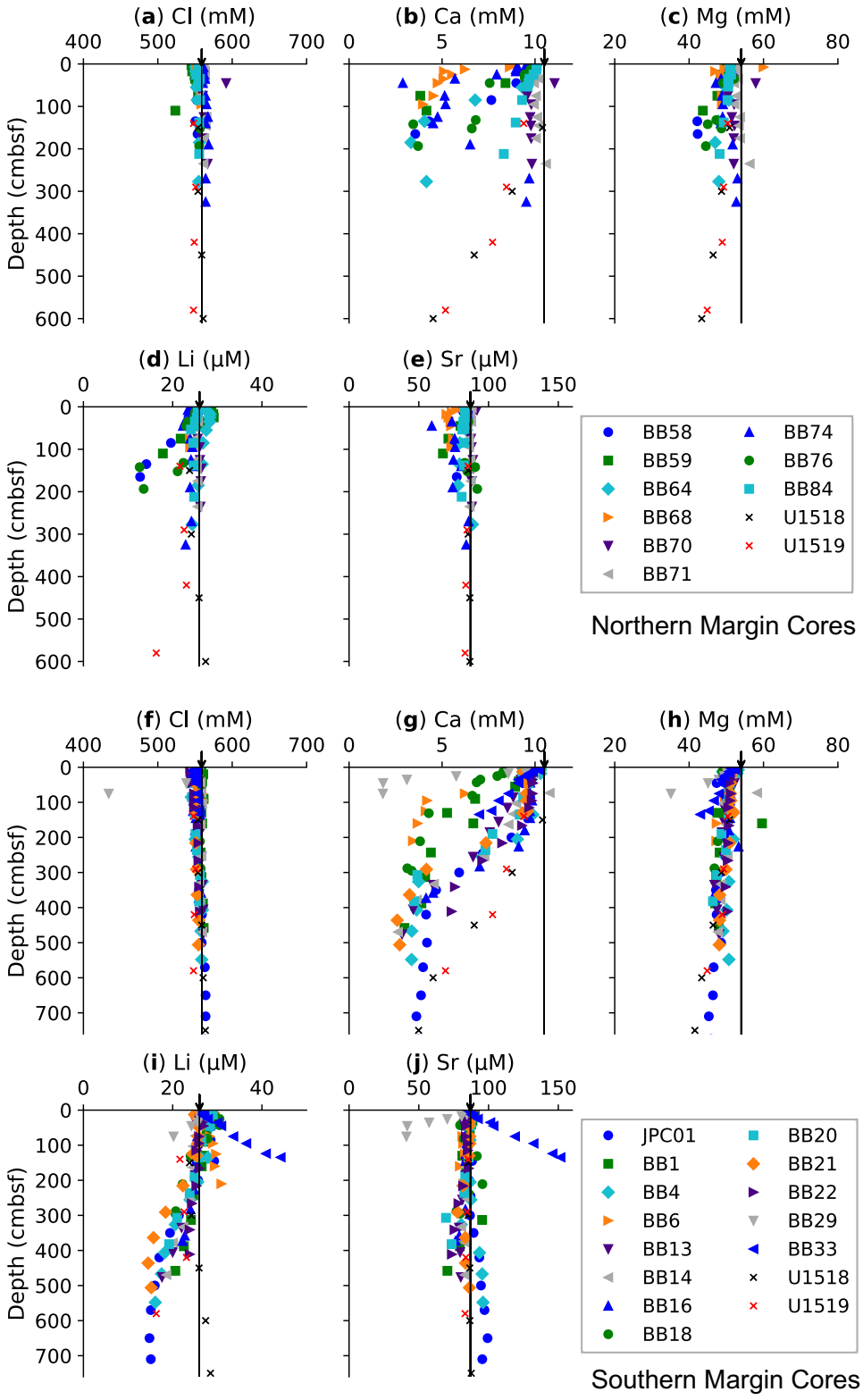

Figure 2.3. Select pore water solute profiles.

Select pore water solute profiles from gravity and piston cores taken at the northern (a-e) and southern (f-j) margin, along with the upper ~600-700 cm of pore water data from

IODP Sites U1518 and U1519 (Wallace et al., 2019). Seawater concentration is denoted by a black arrow and vertical line.

The incoming sediment section at the northern HSZ was drilled at IODP Site U1520 (Wallace et al., 2019; location shown in **Fig. 2.1, 2.2**). Coring of the upper ~510 mbsf recovered mainly trench-wedge facies and submarine slide materials (Barnes et al., 2020; Wallace et al., 2019; **Fig. A9**). Below 650 mbsf, Site U1520 is thought to sample the protolith material for the plate interface, i.e., the incoming plate interval that correlates to the plate interface zone (Barnes et al., 2020; Dutilleul et al., 2020). This protolith interval is composed largely of pelagic carbonates with alternating clay-rich layers (Lithologic Unit IV) and a highly altered volcaniclastic conglomerate with a smectite-based matrix (Lithologic Unit V) (Barnes et al., 2020; Wallace et al., 2019; **Fig. A9**). Analysis of these units suggests low to moderate bound water content in the Unit IV marls (~2–15%) and chalks (~2%), and very high hydrous mineral content (up to ~22%) in the Unit V smectite-rich volcaniclastic conglomerates (Dutilleul et al., 2020). The smectite to illite transition reaches peak fluid production at 60 – 150 ˚C, producing fluid in proportion to the amount of smectite present. Thermal modeling of the northern HSZ predicts that temperatures reach this range along the plate boundary between 10 and 50 km landward of the deformation front (Antriasian et al., 2019; **Fig. A10**). Thus, if fluids originating from within or below the plate interface 10 – 50 km landward of the deformation front are discharging at seep sites, they should carry low chloride concentrations indicative of smectite (and zeolite) dehydration reactions in the volcaniclastics (Lithologic Unit V).

The fault-hosted seep sites we sampled in the northern margin span the area from the deformation front to the shelf break approximately 40–45 km landward (**Fig. 2.2**); these sites overlap the region of expected dehydration reactions (**Fig. A10**). However, Cl concentrations in our sediment cores remain near seawater values, with endmember concentrations generally

ranging from 551-560 mM (**Fig. 2.3a**). Despite sampling seep sites that are thought to tap deeper fluid sources, the near-seawater Cl concentrations indicate that these fluids likely originate from sediment compaction within the accretionary wedge, rather than dehydration of the lower wedge or underlying underthrust sediment. We are confident that the lack of low-Cl signal is not a mere product of dilution with seawater-Cl fluids from compaction sources given that modeling by Ellis et al. (2015) predicted the volumetric fluid release from smectite-illite transformation in the wedge (1.2 m^3 yr^{-1} m^{-1}) and subducting sediments (1.8 m^3 yr^{-1} m^{-1}) is ~10% of the total fluid release from porosity change and mineral dehydration (~30 m^3 yr^{-1} m^{-1}), well within detectability of our methods. Further, these results are consistent with findings at IODP Site U1518: although U1518 sampled the westward-dipping Pāpaku thrust fault that extends from the megathrust to the seafloor at a depth of 304 – 322 mbsf, no low Cl signature was detected (Morgan et al., 2022; Wallace et al., 2019; **Fig. A9**).

To test our interpretation of shallow fluid sources, we consider additional pore water geochemistry data from the incoming section drilled at Site U1520 (**Fig. A9**). Pore fluid data from the lower section of subduction inputs (Lithologic Units IV and V) exhibit anomalous values of Sr, Mg, and Ca, that are easily distinguished from shallower accreted materials (Lithologic Units I – III) (Wallace et al. 2019; **Fig. 2.4**, **A9**). These signatures of the deeper units have been attributed to carbonate recrystallization towards dolomite (Wallace et al., 2019), which consumes Mg and releases Ca and Sr. In addition, a dissolved Li peak is observed at the transition between the shallower Unit III trench-wedge facies and deeper Unit IV pelagics, which has been interpreted to result from ash alteration (Luo et al., 2024). These anomalous signatures (low Mg, high Sr, Ca, Li) should be detectable in our samples if fluids were traveling from the plate boundary and deep wedge to the seafloor seeps.

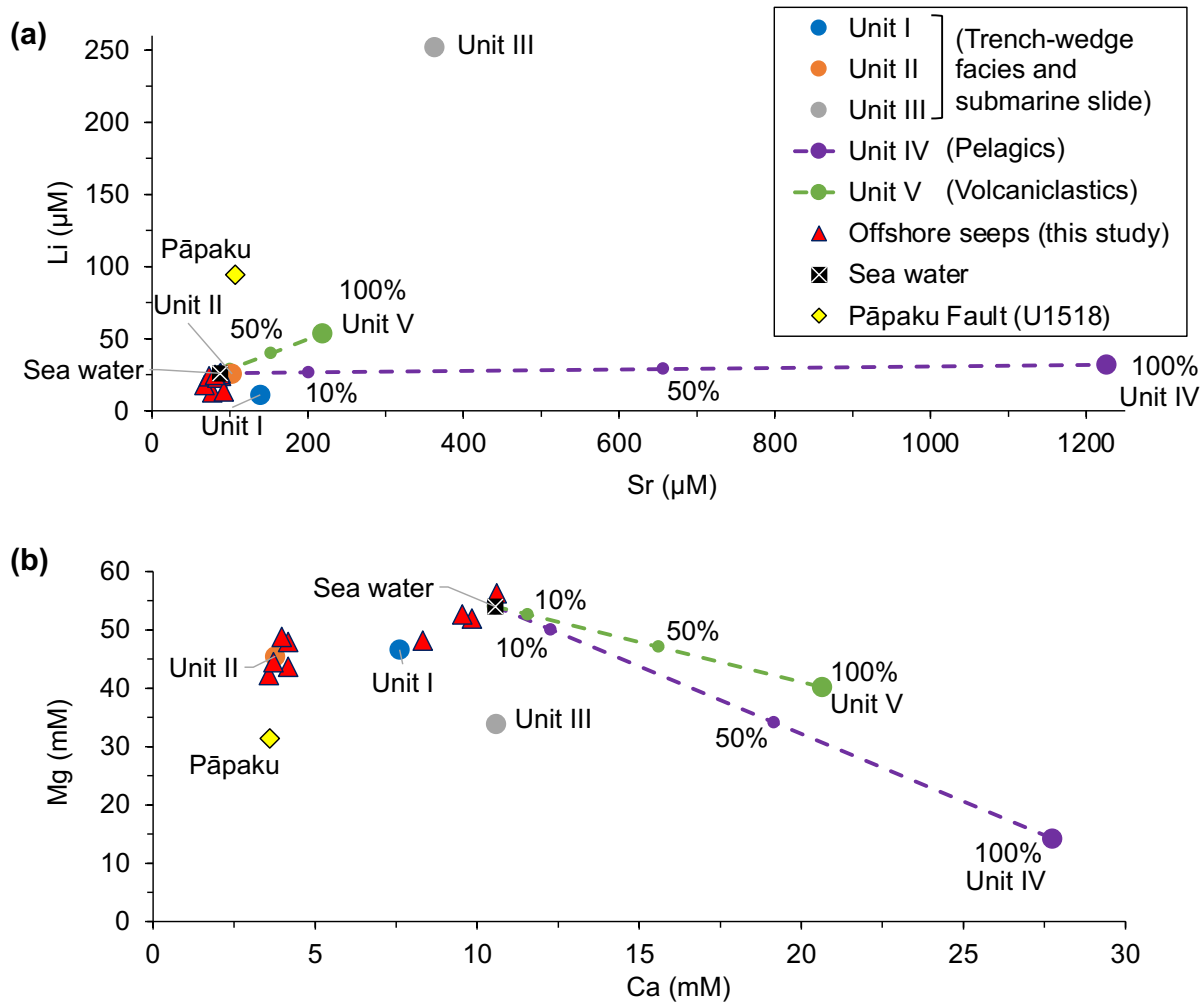

Figure 2.4. Cross plot comparisons of endmember fluid compositions.
Cross plots of Li vs. Sr (a) and Mg vs. Ca (b) concentrations. Data points include endmember concentrations for IODP Site U1520 Lithologic Units I-V (Wallace et al., 2019), measurements from the Pāpaku fault at IODP Site U1518, and cores from the northern margin in this study. Dashed lines represent concentrations resulting from mixing seawater with U1520 pelagic carbonates (Unit IV) and volcaniclastics (Unit V).

Figure 2.4 shows the endmember pore water concentrations of Li, Sr, Mg, and Ca for Lithologic Units I – V at Site U1520 (incoming sediments) and of the Pāpaku fault (U1518), alongside the endmember composition from our seep cores in the northern margin. Pore water data of seep cores roughly fall on a mixing line connecting seawater values with the compositions of fluids from the shallowest sediments (Units I and II) from Site U1520 (**Fig. 2.4**),

indicating that the fluid chemistry is likely the result of mixing between those two sources. Mixing lines connecting seawater values with endmember compositions of the deeper pelagics and volcaniclastics (Units IV and V) show how pore water composition would change for a given contribution of deeply-sourced fluid. These scenarios demonstrate that even a small fraction of fluids from the plate boundary or deep wedge (e.g., 10%) would cause a noticeable shift in composition. Such a shift is not observed in any of our northern margin cores, nor in fluids sampled directly from the Pāpaku fault at IODP Site U1518.

Because the IODP drilling transect (Wallace et al., 2019) and thermal modeling (Antriasian et al., 2019) are confined to northern Hikurangi, we do not include our southern margin results on the cross plot comparisons with Site U1520 (**Fig. 2.4**). The compositions of the southern margin cores, however, are generally comparable to those in the north, with no evidence of considerable alteration or input from mineral-dehydration reactions (**Fig. 2.3, A7**). However, two cores from the southern margin deviate from the norm. BB29 collected at Site 7S presents lower solute concentrations than average, explained by in situ carbonate mineral precipitation and gas hydrate dissociation upon core recovery. Numerous carbonate nodules and evidence of gas hydrate noted during ship-board processing of BB29 support this interpretation. Core BB33 taken at Site HFA_S, shows enrichment in Li and Sr not seen elsewhere. While these characteristics could signal fluid migration from depth, the enriched K and near-seawater Cl, S, B, and alkalinity also observed in this core are not consistent with enhanced fluid flow or deep sources. No known seep is associated with this site and heat flow determinations are not elevated. Instead, the enhanced Li and Sr in BB33 could be explained by ash dissolution/alteration which has been previously documented to release Sr and Li into the pore water at Hikurangi (Luo et al., 2023, 2024; Wallace et al., 2019). Overall, no systematic

differences in geochemical observations between the northern and southern sites are observed despite the varying subducted sediment thicknesses and tectonic characteristics along the margin (e.g., incoming plate roughness, convergence rate, slip behavior).

In summary, the geochemistry results from sediment cores collected at fault-hosted seep sites in both the northern and southern margin lack evidence of deep-sourced fluid input or long-range fluid flow. Most notably, Cl concentrations show no contribution from dehydration reactions, and Sr, Mg, Ca, and Li concentrations do not reflect those observed in the deep incoming sediments sampled at U1520 (**Fig. 2.3, 2.4**). Moderate B and K values (**Fig. A7, A8**) also suggest shallow sediment-water reaction sources given that input from altered, higher-temperature fluid sources would cause a significant increase in B and reduction in K (Kastner et al., 2014; Philip et al., 2023) not observed in our cores. The fault-hosted seep fluids lack evidence for drainage of the plate boundary and instead suggest a shallow wedge-compaction source at temperatures lower than 60 ˚C.

2.5.3 *Modeled fluid flow rates and inferences on fault zone permeability*

Fluid advection rates at seep sites are estimated by best fitting the measured NH_4 data from our sediment cores to modeled advection rate scenarios at reference Sites U1518 and U1519. NH_4 profiles for eight cores (four northern margin and four southern margin cores) are plotted along with the model-generated advection rate scenarios in **Fig. 2.5**, where positive values indicate upward fluid flow. Estimated maximum rates for all modeled cores are summarized in **Fig. 2.2** and **Table A2**. We note that cores with a mixed layer (vertical pore water solute profiles at seawater concentrations in the upper sediment column) are plotted from the base of the mixed layer to depth when estimating advection rates (e.g., BB6, BB59, BB20, and BB21 in Fig. 2.5), where the depth of the mixed layer is based on the alkalinity profiles. Cores

without a mixed layer (i.e., pore water solute profiles exhibit immediate excursions from seawater concentrations) are plotted from the seafloor to estimate advection rates (e.g., BB80 and JPC02 in Fig. 2.5). Cores whose full NH_4 profiles remain near-vertical or are concave-up are plotted from the seafloor and listed as zero upward flow (e.g., BB7 and BB71 in Fig. 2.5).

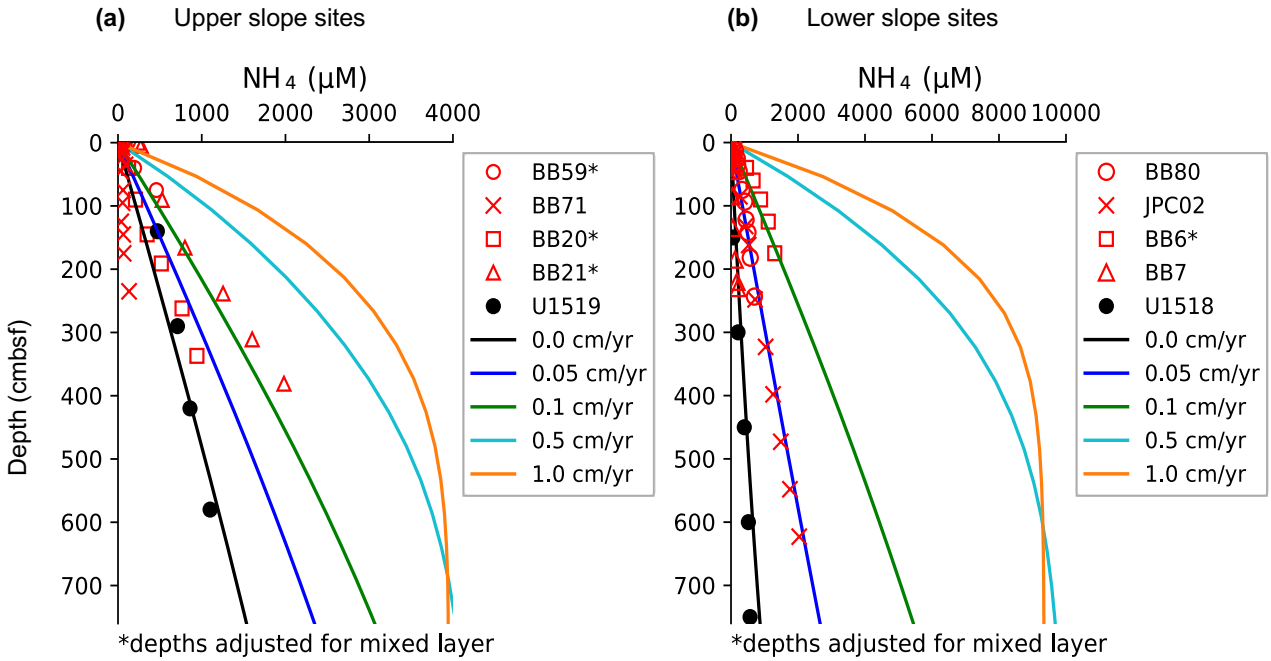

Figure 2.5. Select pore water solute profiles and advection model results.

Measured pore water ammonium profiles for 8 example cores (red symbols), and for the upper ~700 cm at IODP Sites U1518 and U1519 (black circles). Solid lines show modeled ammonium profiles for Sites U1518 and U1519 given a range of upward advection rate scenarios. Cores located on the mid-upper slope of the northern and southern margin (Sites 3N, 4N, 5N, 4S, 5S in this study) are referenced to U1519 (a) and cores on the lower slope (Sites HFA_N, 1N, 1S, 2S, 3S, 7S, HFA_S in this study) are referenced to U1518 (b). We estimate the following upward advection rates (cm/yr) for the example cores based on best fit (by-eye) to modeled profiles: BB21– 0.2; BB6, BB59 – 0.1; BB80, JPC02 – 0.05; BB20 – 0.04; BB7, BB71 – 0.

The rate of upward fluid flow varies between sites, ranging from ~0.04 to ~2 cm/yr. Similar to the pore fluid composition, the observed variations do not show a systematic or predictable change from north to south along strike, or from trenchward to landward across strike

(**Fig. 2.2, Table A2**). In the northern margin, the highest estimated flow rate for piston and gravity cores is ~0.1 cm/yr upward (BB59) located about 22 km landward of the deformation front. The remaining piston and gravity cores have rate estimates of <0.1 cm/yr upward. Estimated rates from southern margin piston and gravity cores are similarly low, with maximum rates of ~0.2 cm/yr upward (BB21). Two push cores, ROVPC1_1121 (northern margin) and ROVPC15_1115 (southern margin) give the highest flow rates estimates of ~2 and ~1 cm/yr, respectively. Notably, even the cores with the highest upward flow rates (e.g., ROVPC15_1115 and BB21) do not show geochemical signatures of deeply-sourced fluids (i.e., low Cl, K, high B, Li).

The range of modeled fluid flow rates is relatively low (generally ≤ 0.2 cm/yr) despite targeting seeps associated with fault zones that could channel fluid flow. We compare our estimated rates to the seafloor seepage rate predictions at fault zones in the outer forearc of subduction zones by Sun et al. (2020a). They use a numerical modeling approach in which mechanical loading, deformation, and fluid drainage are fully coupled. Given fault zone permeabilities that are considerably enhanced relative to sediment matrix permeabilities (Sun et al., 2020a, models REF, MK2, FK2), their models predict seafloor seepage rates of 10 cm/yr at fault zone locations. Our estimated flow rates are more compatible with model scenarios of little to no fault zone permeability enhancement, which predict rates of <5 cm/yr (Sun et al., 2020a models FK1, FK3). In summary, sediment cores from both the northern and southern Hikurangi margin provide geochemical evidence for low fluid flow rates that do not vary systematically, and imply relatively low fault zone permeability.

2.5.4 *Attenuation of geochemical signals due to diffusive loss along flow path*

Given the low fluid flow rates we estimate at fault-hosted seeps (≤ 2 cm/yr), we consider whether the lack of a geochemical signal of underthrust fluids (i.e., anomalous solute concentrations) could be due to diffusional loss during fluid migration from depth (e.g., Saffer & Screaton, 2003). To test the expected solute concentration loss due to diffusion to the surrounding sediment matrix during fluid transport along faults, we apply the diffusional loss model (Eqns. 2.5-2.10) to four representative fault geometries (**Fig. 2.2, 2.6, Table 2.1**). Fault length, depth of fault at $x = 0$ (h_0), and fault dip (φ) span the range of splay fault geometries along seismic line 05CM-04 at the northern Hikurangi margin (Barker et al., 2018). We calculate temperature at the bottom boundary (T_{base}) from the bottom water temperature (T_0) and the thermal gradient (Γ), based on results from Antriasian et al. (2019). Thermal conductivity ($\lambda = 0.9$ W/m K) is based on measurements from Antriasian et al. (2019) and we use a thermal diffusivity (α) of 1×10^{-6} m^2/s. Porosity (ϕ) is based on model results from Ellis et al. (2015). We use Sr as the modeled solute because the high Sr concentrations measured in the pelagic section of the incoming sediments at Site U1520 (Lithologic Unit IV) serve as an effective tracer of deep fluids. The Sr concentration at the seafloor (C_0) is the seawater value (**Table 2.1**), and the Sr concentration of 1300 µM at the bottom boundary (C_{base}) is the maximum Sr measured in the pelagic sediments at U1520 (**Fig. A9**). We note that the bottom boundary of 1300 µM Sr is a minimum value, as carbonate recrystallization will continue to add Sr to the pore water during subduction. We test fluid flow rates (q) that span order of magnitude estimates from our observations (0.2 – 2 cm/yr).

Table 2.1. Fault parameters for diffusional loss model

Fault	Fault Length (km)	h_0 (km)	φ (˚)	T_0 (˚C)	T_{base} (˚C)	Γ (˚C/km)	ϕ	C_0 (μM)	C_{base} (μM)
1	3	1.4	28	2	20	13	0.35	87	1300
2	6.9	2.8	24	2	30	10	0.25	87	1300
6	9.9	5	30	2	50	10	0.2	87	1300
8	9.9	8	54	2	150	18	0.1	87	1300

h_0 – depth of fault at $x = 0$; φ – fault dip; T_0 – temperature at $z = 0$; T_{base} – temperature at $x = 0$; Γ – undisturbed thermal gradient; ϕ – porosity; C_0 – Sr concentration at $z = 0$; C_{base} – Sr concentration at $x = 0$.

Using an along-fault fluid flow rate of 2 cm/yr, we find that complete diffusive loss of the high Sr signal does not occur in any of our four tested fault lengths (**Fig. 2.6d**). Only in modeling the longest, steepest-dipping tested fault (Fault 8, 9.9 km long) does the model predict considerable attenuation of the signal such that expected concentrations fall near the point of detectability of our methods. Testing a lower advection rate of 0.2 cm/yr predicts greater signal attenuation, but enhanced Sr concentrations are still detectable along Faults 1 and 2 near the deformation front (Fault 1 shown in **Fig. 2.6c**). The resulting persistent high Sr concentrations for representative Faults 1, 2, and 6 at an advection rate of 2 cm/yr, and Faults 1 and 2 at 0.2 cm/yr (**Fig. 2.6**) discount the hypothesis that diffusional loss alone causes the lack of deeply-sourced fluid signals in our seep samples or the lack of a signal along the Pāpaku Fault drilled at IODP Site U1518 (Wallace et al., 2019).

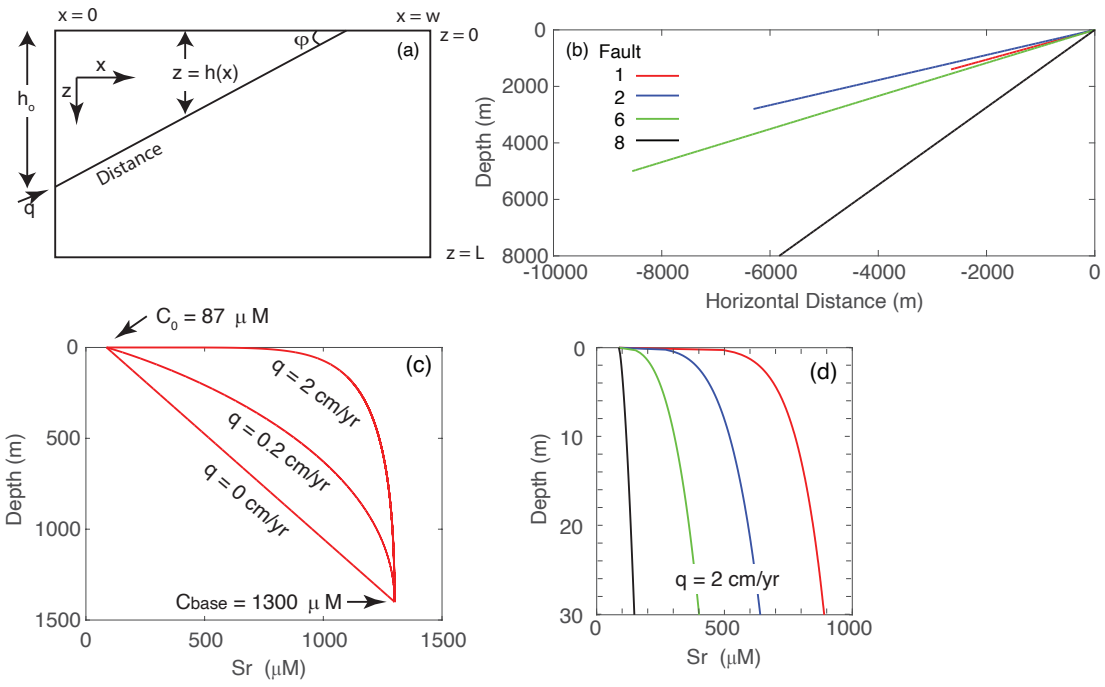

Figure 2.6. Model of geochemical signal attenuation due to diffusive loss along a flow path. (a) Geometry of 2-D fault model with fluid flow rate q (cm/yr). (b) Schematic for four fault geometries tested. (c) Sr concentration along Fault 1 given three different flow rates. (d) Sr concentration along faults near the seafloor for q = 2 cm/yr. Color scheme for (b) and (d) is same as that shown in Figure 2.2.

2.5.5 *Gas-driven processes generate mixed layers in shallow sediments*

When discussing our approach for modeling advection rates using NH_4 profiles, we noted that some of the cores collected at seep sites show near constant solute concentrations in the uppermost sediment, followed by the concave-down profiles below that are indicative of upward fluid advection beneath a mixed layer. For example, JPC01 (**Fig. 2.3, 2.7, A7**), collected from a seep site in the southern margin, shows concave-down profiles of Ca, S, Li, alkalinity, SO_4, and NH_4 beneath vertical profile segments at seawater concentrations that extend ~145 cmbsf. Overprinting the geochemical effects of in situ reactions and upward fluid advection, the vertical profiles in the upper sediments reflect rapid seawater irrigation. The thickness of the mixed layer observed at our seepage locations generally ranges from 4 to 235 cm (**Table A2**). As a result,

cores with shallow penetration (≤~200 cmbsf) often have near-vertical profiles with depth (e.g., JPC01_TC, **Fig. 2.7)** despite close proximity to seepage indicators because they do not penetrate deep enough to surpass the mixed layer.

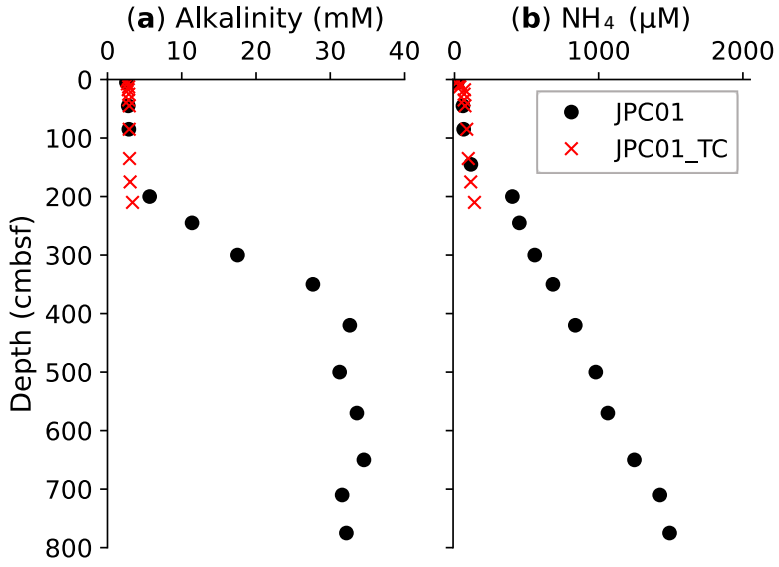

Figure 2.7. Shallow mixed layers in pore water profiles.
Pore water alkalinity (a) and ammonium (b) for piston core JPC01 and associated trigger core JPC01_TC. The trigger core did not penetrate deep enough to capture the advective signal observed in the piston core.

The kinked pore water profile shapes we observe in many seep cores (near-seawater solute concentrations in upper pore fluids and concave-down profiles below) indicate that the rate of seawater irrigation in the upper 10s of centimeters is greater than the rate of upward advection from depth. This phenomenon is ubiquitous at seep sites globally. Observations of mixing in the upper ~1 m sediment are documented, among others, in the Gulf of Mexico (e.g., Solomon et al., 2008), the Sea of Okhotsk (e.g., Haeckel et al., 2007), and in the Cascadia (e.g., Tryon et al., 1999), Svalbard (Hong et al., 2016), and Barbados (Henry et al., 1996) margins. Mixing of bottom water into the uppermost part of the sediment column has been attributed to bio-irrigation (e.g., Aller, 1982), recent, rapid emplacement of sediments (e.g., mass transport

deposits; Hensen et al., 2003; Hong et al., 2014), bubble irrigation (Haeckel et al., 2007), and gas-driven aqueous pumping (Solomon et al., 2008; Tryon et al., 1999). While a quantitative assessment of the rate and impact of such mixing is beyond the scope of this paper, it is likely important for the flux of many solutes across the sediment water interface at seeps worldwide, particularly those that are most impacted by early diagenetic reactions such as SO_4, Ca, Mg, and alkalinity.

2.5.6 *Implications for pore pressure accumulation and the occurrence of slow slip*

Fluids are sourced at depth along the Hikurangi margin through both sediment compaction and mineral dehydration. As observed at other subduction zones (e.g., Hensen et al., 2004; Martin et al., 1996; Philip et al., 2023; Ranero et al., 2008; Torres et al., 2004), we expected to see evidence of these fluids rapidly expelled at structurally-controlled seep sites, which are thought to serve as efficient flow paths from depth. We sampled sites of known fluid emission in the northern and southern margin and do not observe evidence of plate boundary drainage from any fault zone. There is no geochemical evidence of deeply-sourced fluids at our coring locations or along the Pāpaku Fault drilled at IODP Site U1518. Furthermore, the shallowly-sourced fluids we sampled are expelled at low rates (up to 2 cm/yr but generally ≤ 0.2 cm/yr), compatible with model scenarios of little to no fault zone permeability enhancement (Sun et al., 2020a). These observations imply that fluids along the plate boundary and in surrounding sediments (1) are draining laterally and exiting at as-yet unsampled seep sites seaward of the deformation front; (2) have limited vertical drainage and are accumulating in the wedge; or (3) are trapped at depth, causing high pore pressures along the plate boundary.

Lateral flow could occur along permeable sediment layers (e.g., the turbidites of Lithologic Unit III drilled at Site U1520) after vertical flow into the wedge, or possibly through

the fractured basalts of the incoming plate and subducting seamounts, which are likely more permeable than surrounding sediments (e.g., Solomon et al., 2009). If significant lateral drainage of fluid is occurring, the sites of fluid expulsion at the seafloor have not yet been sampled. Given the extent of our sampling program, which targeted all known seep sites identified during several surveys of the region (Watson et al., 2020), we argue that this scenario is unlikely landward of the deformation front. We cannot discount long-distance lateral drainage and fluid expulsion farther seaward. However, the longer flow pathways would not be as efficient as focused flow along splay faults and thus would not be as effective at regulating pore fluid pressure.

In scenario two, deeply-sourced fluids may be draining from the plate boundary, possibly aided by damage associated with seamount subduction in the northern margin (Sun et al., 2020b, Chesley at el., 2021), and stored within the overlying wedge. Fluid storage following drainage into the wedge is consistent with electromagnetic observations that identify regions of anomalous porosities in the lower wedge (Chesley et al., 2021), and seismic observations that identify areas of overpressure in portions of the wedge (e.g., Arnulf et al., 2021). This option is perhaps most compatible with drainage of the plate boundary and underthrust sediments via fault-valving (Sibson, 1990). In the fault-valve model, fluid pressures are cyclically accumulated and then released with fault slip that temporarily opens fluid migration pathways. This model is supported by several lines of geophysical evidence at northern Hikurangi, including the evolution of earthquake focal mechanisms (Warren-Smith et al., 2019), Vp/Vs and shear wave splitting delay times (Zal et al., 2020), and repeating earthquakes (Shaddox & Schwartz, 2019). However, transient fluid pulses from depth during this process would generate visible geochemical signals in our dataset if fault zones acted as efficient vertical pathways for fluid transport to the seafloor. As shown in other regions where fluid discharge is episodic, the pore water profiles will show

non-steady state characteristics that can last on the order of thousands of years (Hong et al., 2016). We postulate that trapping of fluids within the wedge could explain the lack of geochemical evidence for a previous discharge pulse despite geophysical inferences for fault-valving at northern Hikurangi.

At the southern margin, early, efficient drainage of the subducting sediments into the upper plate in the region of our southern margin sites has been inferred from seismic data (Crutchley et al., 2020). However, while several anomalous heat flow values near the deformation front (Sites 1S and 2S; **Fig. 2.1**, **A3**, **A4**) may be indicative of local fluid advection, pore fluid compositions at the sampled seeps do not reflect deep fluid sources. Instead, our geochemical results indicate that fluids draining from the plate boundary and subducting sediments do not reach the seafloor. Thus, fluids may remain trapped in the outer wedge at this portion of the southern margin. This interpretation is compatible with the presence of a low seismic velocity zone at the base of the frontal thrust fault in the lower wedge beneath Site HFA_S, which has been interpreted as a zone of high pore fluid pressure resulting from compressional deformation and upward drainage of subducting sediments (Crutchley et al., 2020).

A third scenario to explain our observations is that in the absence of efficient drainage, fluid input from the compaction and dehydration of the smectite-rich volcaniclastics that make up the lower subduction inputs, would lead to overpressure along the plate boundary. This interpretation is consistent with geophysical studies that have imaged high-reflectivity zones (Bell et al., 2010), high conductivity/low resistivity anomalies (Heise et al., 2017), and low Vp and high Vp/Vs (Eberhart-Phillips & Bannister, 2015) at northern Hikurangi. These observations have been interpreted as fluid-rich, overpressured zones along and surrounding the plate

interface in the region of slow slip. Numerical models that prescribe low splay fault and megathrust permeabilities are also in line with these interpretations, predicting high fluid pressures at depth and low fluid flow rates at the seafloor (Ellis et al., 2015; Sun et al., 2020a).

In summary, our results of shallowly-sourced, slow-flowing fluids at fault-hosted seeps indicate that splay fault and megathrust permeabilities at the Hikurangi margin are low, leading to relatively poor vertical drainage of the lower-wedge, plate boundary, and underthrust sediments to the seafloor. This in turn may result in the development of an overpressured system that spans from the deformation front to the upper slope. Initial results from the NZ3D seismic reflection experiment at the northern margin imaged high-velocity layers at the base of the hanging wall of faults in the outer forearc (Gase et al., 2023; Han et al., 2022), interpreted as low-permeability carbonate layers which disrupt BSR (bottom simulating reflector) continuity and potentially inhibit fluid flow along fault planes (Han et al., 2022). These findings provide one possible explanation for low splay fault permeability and poor fluid drainage along fault zones offshore northern Hikurangi.

However, there is evidence of deeply-sourced fluid venting landward of the upper slope region, at onshore seeps ~75 km landward of the deformation front. Previous studies that sampled onshore springs along the margin have reported signatures of deeply-sourced fluids as well as a systematic decrease in solute concentration from north to south (Barnes et al., 2019, Reyes et al., 2010). **Fig. 2.8** shows a cross plot of Li vs. Sr concentrations which showcases the composition of the onshore seep fluids. Unlike the offshore seeps sampled in this study, onshore forearc seeps (those plotted are from the northern margin only) exhibit highly altered fluid compositions with enhanced Li and Sr concentrations indicative of inputs from deep sources.

Barnes et al. (2019) attributed variation in seep composition along strike to changes in upper plate structural permeability rather than a systematic change in fluid source along the margin.

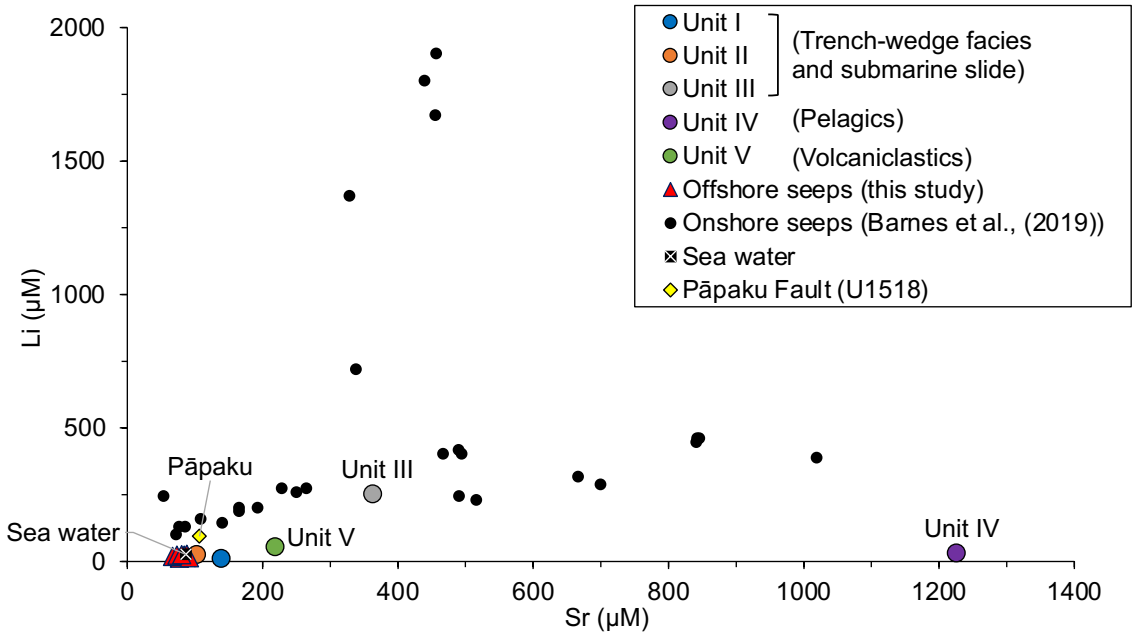

Figure 2.8. Cross plot comparison of onshore and offshore seep endmember compositions. Cross plot of Li vs. Sr concentrations at onshore seeps sampled in the northern margin (Barnes et al., 2019), endmember concentrations of IODP Site U1520 Lithologic Units I-V, the Pāpaku fault at IODP site U1518, and cores from the northern margin in this study.

The venting of fluids from deep sources at onshore seeps in the northern margin may be enabled by the transition from a compressional to extensional stress regime, which enhances upper-plate permeability (McNamara et al., 2021; Sibson & Rowland, 2003). A modeled enhancement in effective coefficient of friction at ~50 km landward of the deformation front based on heat flow measurements is consistent with the onset of extension in the upper plate marking the down-dip extent of overpressure along the plate boundary (Antriasian et al., 2019). The Tuaheni Seep Field (Site 5N in this study) on the shelf break at the northern margin, lies just seaward of this onset of extension. We did not sample deeply-sourced fluids at this site, but the active, dense fluid expulsion recorded at this location (>1700 seep indicators covering ~90 km^2;

Watson et al., 2020) suggests enhanced permeability. A tectonically-driven change in permeability structure likely explains the change from inefficient drainage of the plate boundary along faults in the offshore forearc to efficient drainage observed at onshore seeps, associated with the transition from compression to extension ~50 km landward of the deformation front.

2.6 CONCLUSIONS

We collected heat flow measurements and performed geochemical analyses on pore water of sediment cores taken at structurally-controlled seep sites spanning the continental slope of the southern and northern Hikurangi margin. We do not observe evidence for wide-spread warm fluid discharge, or deeply-sourced or dehydration-derived geochemical signals at our sample sites. Cl concentrations are at near seawater composition in all our cores even though the plate boundary is within the modeled temperature range for clay mineral dehydration. Additionally, near-seawater Li, B, and Sr concentrations in offshore seep fluids provide no evidence of contributions from the protolith material for the plate interface (the pelagic and volcaniclastic Units of the incoming section at IODP site U1520). Modeled upward fluid advection rates are relatively low, ranging from ~0.04 – 2 cm/yr. Overall, our results from offshore seeps show no evidence of appreciable drainage of the plate boundary along fault zones.

This result contrasts with observations at many other subduction zones of seep fluid geochemical signatures indicative of long-distance transport from plate boundary depths. Deep-sourced fluids have been identified at seeps along Barbados (Martin et al., 1996), Nankai (Pape et al., 2014; Toki et al., 2014), Costa Rica (Hensen et al., 2004, Ranero et al., 2008), Chile (Scholz et al., 2013), Marianas (Mottl et al., 2004), and Cascadia (Philip et al., 2023) using sediment cores with similar penetration depths to our samples. Instead, shallow fluid sources and

low flow rates at Hikurangi suggest that fault zones from the deformation front to the upper slope are relatively impermeable at depth and prevent efficient drainage of the megathrust and surrounding sediments to the seafloor. Our results are consistent with a plate boundary and/or lower wedge that is poorly drained and over-pressured, likely influencing the occurrence of slow slip.

2.7 Acknowledgments

This work is supported by NSF awards OCE-1753617 and OCE-1753665. MET acknowledges support from a fellowship by the Hanse-Wissenschaftskolleg Institute for Advanced Study (HWK), Germany. We thank the science party, captain and crew of the *R/V Revelle*, the Oregon State University coring facility (MARSSAM), and the ROV *Jason* team onboard during the 2019 expedition for making this work possible. Special thanks to Jess Hillman for assistance with onshore logistics and hydroacoustic surveys on the SAFFRONZ expedition, Valerie Stucker for providing laboratory space in New Zealand for cruise preparations, Brendan Philip for assistance with hydroacoustic surveys, and Theresa Whorley for assistance with pore water sampling. We are grateful to Gareth Crutchley and one anonymous reviewer whose thoughtful comments improved this manuscript.

2.8 Open Research

All pore water geochemistry data produced for this study are publicly available at https://doi.org/10.60520/IEDA/113176 (Aylward et al., 2024). Heat flow data are available at https://www.marine-geo.org/tools/files/31405 (Harris et al., 2023).

Chapter 3. SEAFLOOR FLUID FLOW TRANSIENTS LINKED TO SLOW SLIP AT THE NORTHERN HIKURANGI MARGIN

*This chapter will be submitted to a journal with the following author list:
I. Aylward, E.A. Solomon, L.M. Wallace

3.1 ABSTRACT

Mechanical and hydrogeologic processes are inextricably linked at subduction zones. Broad scale hydrogeologic conditions are often inferred from geophysical proxies or numerical models, whereas direct measurements are rare and often temporally static, limiting our understanding of the interrelationships between pore fluid pressure, fluid flow, and fault slip. Using continuous records of fluid flow rate from 10 seafloor flow meters from February to November 2019, we investigate the hydrologic responses to a large slow slip event (SSE) at the northern Hikurangi margin, New Zealand. Flow meter records at four diffuse flow locations indicate that creep characterizes the shallow megathrust during the inter-SSE period, with locking farther landward. Flow transients correlate temporally with the SSE, consistent with compressional volumetric strain (~0.1 microstrain) on the mid continental slope and dilatation (≤ –0.4 microstrain) near the deformation front. We propose that transients at two focused flow sites may reflect a temporary enhancement of shallow fault-zone permeability in response to the SSE. Flow records at four other focused flow sites are dominated by shallow gas-dynamics. This work provides the first set of direct measurements of seafloor fluid flow rates throughout a slow slip cycle at the Hikurangi margin, contributing to an improved understanding of offshore locking, shallow slow slip behavior, and margin dewatering.

3.2 INTRODUCTION

Observed at subduction zones globally, slow slip events (SSEs) are aseismic episodes of elevated fault slip rates lasting days to years (e.g., Sacks et al., 1978; Peng & Gomberg, 2010). Many geophysical and modeling studies indicate that low effective normal stress tied to pore fluid overpressure may promote conditional fault zone stability and encourage slow slip (Kitajima & Saffer, 2012; Kodaira et al., 2004; Liu & Rice, 2007; Saffer & Wallace, 2015). In addition, fault slip (seismic and aseismic) is thought to modulate fluid flow by inducing a poroelastic response to strain and generating non-elastic permeability changes (e.g., Roeloffs, 1996; Sibson, 1990). In these ways, fault zone hydrogeologic and mechanical processes are intimately linked: pore fluids regulate fault slip by bearing loads (reducing the effective normal stress), and fault slip affects pore fluid pressure and fluid flow by changing pore volume and permeability (Neuzil, 2003). Long-term fluid flow measurements at subduction zones provide a means to observe background flow conditions and record the hydrologic response to deformation, informing on the evolution of fault zone permeability, fluid pressure conditions, and the overall state of strain in the outer forearc (e.g., Brown et al., 2005).

At the northern Hikurangi margin, offshore the North Island of New Zealand (**Fig. 3.1)**, cyclic shallow SSEs have been detected every ~2 years since the onshore GNSS network GeoNet was established in 2002 (Wallace, 2020). Additional offshore instrumentation including two CORK borehole observatories (U1518 and U1519, Wallace and Saffer et al., 2019) and campaign deployments of seafloor pressor sensors and seismometers (Wallace et al., 2016; Woods et al., 2022) have greatly increased the resolution of slip distribution models and indicate that slow slip may propagate out to the trench. Geophysical (Basset et al., 2014; Bell et al., 2010; Eberhart-Phillips & Bannister, 2015; Heise et al., 2017) and numerical modeling (Ellis et al.,

2015) studies provide evidence for fluid-rich zones surrounding the plate interface in the source region of slow slip and support the hypothesis that overpressure enables this shallow slow slip behavior. Recent studies implicate hydrous subducting sediments and seamounts (Barnes et al., 2020; Bangs et al., 2023; Gase et al., 2023; Chesley et al., 2020; Sun et al., 2020) as well as low fault zone permeability in the wedge (Aylward et al., submitted; Cook et al., 2020; Han et al., 2022; Morgan et al., 2022) as primary mechanisms generating fluids at depth and preventing efficient fluid outflow. Previous studies based on temporal observations suggest that fluid flow, and therefore fluid pressures, evolve throughout the slow slip cycle via fault valving (Warren-Smith et al., 2019; Zal et al., 2020; Shaddox & Schwartz, 2020). In this fault valve model, fluids are accumulated during interslip periods and released when fault slip temporarily opens fluid migration pathways (Sibson, 1990). Despite abundant geophysical and modeling evidence suggesting significant ties between fluid accumulation and slow slip at northern Hikurangi, direct observations of fluid flow during slow slip are lacking.

Here we present a continuous record of seafloor fluid flow rates before, during, and after a large slow slip event at the northern Hikurangi margin. In early 2019, we deployed twelve flow meters offshore Gisborne (**Fig. 3.1**) to monitor the fluid flow response to slow slip. In March–June of 2019, a large SSE involving 150–200 mm of total slip occurred beneath the instrument array at 6–9 km depth (Woods et al., 2024). Flow meters located at diffuse flow settings allow us to observe the poroelastic response to the Gisborne event (i.e., the vertical flow induced by local volumetric strain). Flow meters located at seafloor seeps hosted by fault zones allow us to test the fault-valve model by detecting permeability changes during slip. This dataset provides a detailed picture of the hydrologic responses to the 2019 Gisborne SSE.

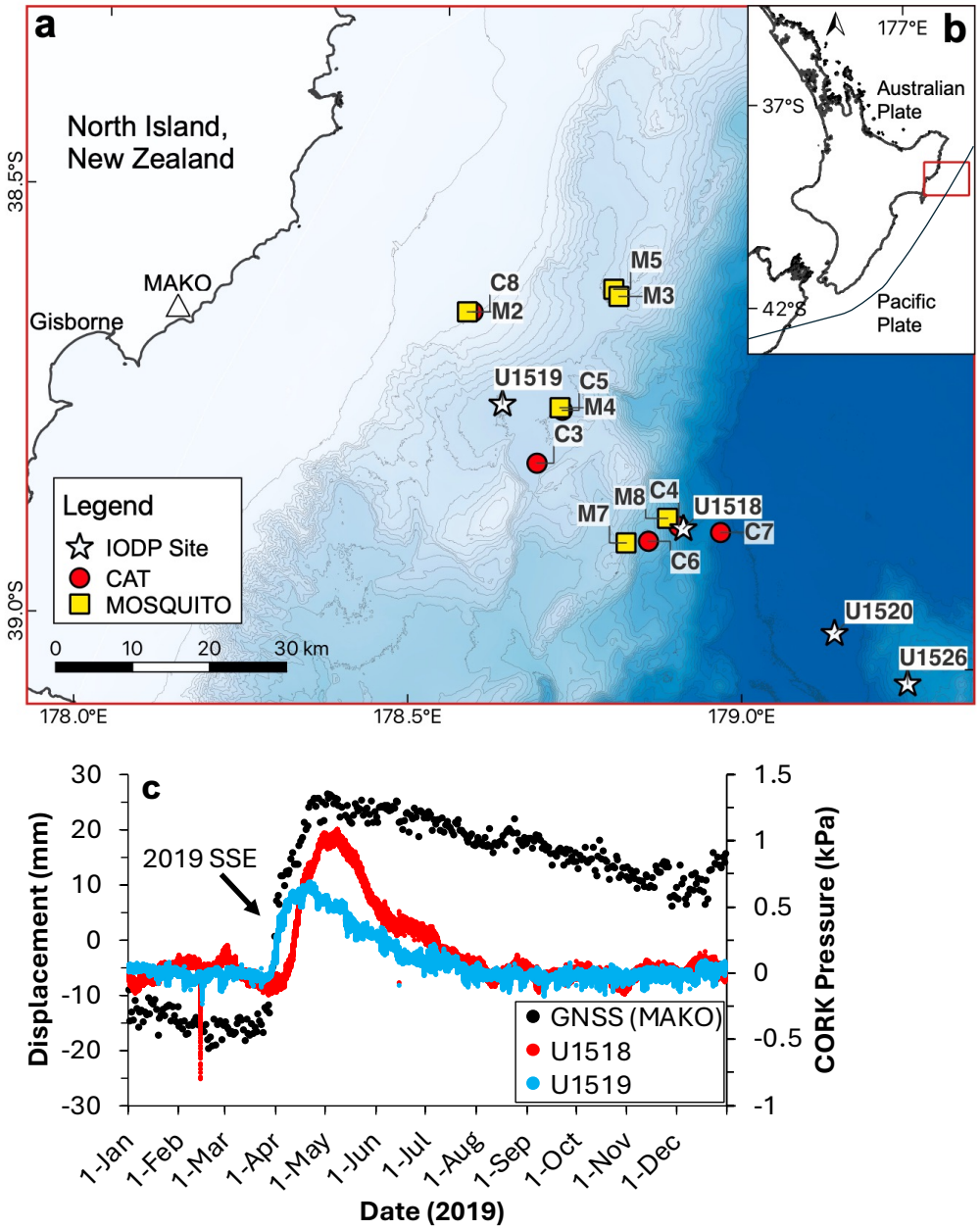

Figure 3.1. Bathymetric map and CORK and GNSS time-series at the northern Hikurangi margin.

(a) Instrument locations. (b) Regional map of the North Island of New Zealand. (c) 2019 time-series of eastward displacement (mm) of onshore GNSS station MAKO (https://www.geonet.org.nz) and borehole pressure (kPa) at IODP CORK Sites U1518 and U1519 (locations shown in a). CORK pressure data was detrended to account for drift of the pressure sensor, and a long-term (~1-year post drilling) borehole transient was removed. Oceanographic signal was filtered using the pressure sensor at the wellhead (e.g., Araki et al., 2017).

3.3 Fluid Flow Meters

We present flow rate data from two types of seafloor fluid flow meters (**Appendix B**): Chemical Aqueous Transport (CAT) meters (**Fig. B1**; Tryon et al., 2001) and Multiple Orifice Sampler and Quantitative Injection Tracer Observers (MOSQUITOs) (**Fig. B2**; Solomon et al., 2008). We deployed six CATs and six MOSQUITOs offshore Gisborne in January and February 2019. Deployment locations spanned the shelf break to the deformation front and targeted both diffuse flow (non-seep) and focused flow (seep) sites. The instruments remained on the seafloor for over two years, continuously collecting a mix of pore fluid and non-reactive tracer solution in their sample coils via osmotic pumps (Jannasch et al., 2004). We recoverd all instruments in March 2021. Upon instrument recovery, we systematically cut sample coils into discrete intervals and transferred the fluid contained in each tubing segment to individual bottles for preservation.

We time-stamped each sample given fixed end points of the time-series (the deployment and recovery dates) and assuming a constant pump rate throughout the deployment (methods). We analyzed a subset of samples for tracer concentration at the University of Washington (methods), excluding samples from two instruments that had problems during deployment or recovery (C8, M3). Concentrations of Li, B, Sr, and Ba were concurrently analyzed for CAT meter samples. We then modeled tracer concentrations to quantify flow rates over time (methods). In total we report flow rate (**Table 3.1, Fig. 3.2-3.3**) and concentration (**Fig. 3.5-3.12**) data from ~February to November 2019 for ten instruments: five CATs and five MOSQUITOs. This time window captures the 2019 SSE and several months following it.

3.4 FLUID FLOW OBSERVATIONS

The first order results of this study document that net flow polarity varies across strike, and that transient flow pulses occur before and during the bulk of SSE deformation as recorded by onshore GNSS stations and in borehole pressure records.

Diffuse flow records (CATs C4, C5, C6, C7) are generally characterized by two prominent flow rate peaks in the beginning of the deployment followed by a reduction in flow to near 0 cm/yr for the remainder of the analyzed period (**Fig. 3.2, Table 3.1**). Near the base of the continental slope, diffuse sites exhibit net downward flow of fluid into the sediment at CATs C4, C6, and C7. Downward flow transients occur in early March 2019, and again in April 2019, peaking at rates of < 1 cm/yr. Plots of the cumulative flow distance for C6 and C7 show these transients as step-like features relative to a steadier background (**Fig. 3.2**). Peaks in flow at C4 are not as discrete or step-like, likely due to a lower sampling resolution caused by decreased osmotic pump rate relative to the other CATs. These records sharply contrast to that of C5 located farther up-slope, which exhibits net upward fluid flow. Peaks in flow rate of ~0.2 cm/yr occur in mid-February and mid-March 2019. The C5 cumulative flow distance record mirrors those of the lower-slope sites (**Fig. 3.2**).

Focused flow records (C3, M2, M4, M5, M7, M8) are more variable (**Fig. 3.3, Table 3.1**). CAT C3 and MOSQUITO M4 on the mid-slope record overall net upward flow, while M2 (upper-slope), M5 (mid-slope), and M7 and M8 (lower-slope) record net downward flow. Flow records of C3 and M8 exhibit discrete periods of rapid upward flow that are temporally correlated with the SSE and associated with a sharp upward step in the cumulative flow record. Noisy, mixed-polarity signals characterize the flow rate records at M2 and M4; no significant flow event is correlated with the SSE at these sites. Fluid samples from M5 and M7 did not

contain any tracer solution indicating net downward flow persisted throughout the deployment. This prevents us from identifying fluid transients correlated with the SSE at these two sites, and thus they are not included in Figure 3.3.

Table 3.1. Summary of flow rate modeling results.
Negative flow rates are downwards (into the sediment), and positive flow rates are upwards (out of the sediment). Instantaneous flow rate results for MOSQUITOs are non-unique; we give peak flow estimates for both flow rate solutions shown in Fig. 3.3.

	Instrument	Lat.	Lon.	Analyzed Period	Net Flow Rate (cm/yr)	Net Flow Distance (cm)	Peak Flow During SSE (Date)	Peak Flow Rate During SSE (cm/yr)
Diffuse flow records	C7	-38.860	178.952	12 Mar - 31 Oct	-0.12	-0.08	1-Apr	-0.65
	C4	-38.857	178.889	6 Mar - 31 Oct	-0.018	-0.012	18-Apr	-0.05
	C6	-38.876	178.845	26 Feb - 30 Oct	-0.078	-0.053	4-Apr	-0.25
	C5	-38.730	178.704	20 Feb - 29 Oct	0.052	0.029	13-Mar	0.18
Focused flow records	M8	-38.848	178.871	2 Mar - 7 Oct	-15	-9.8	21-Apr - 6-June --	35 --
	C3	-38.794	178.671	19 Feb - 21 Oct	4.1	2.7	21-Mar	40
	M4	-38.727	178.700	2 Feb - 1 Nov	5.4	3.9	-- --	-- --
	M2	-38.622	178.554	17 Feb - 1 Nov	-7.8	-5.7	8-Apr - 16-May 9-Apr - 27-Apr	6 9
	M7	-38.880	178.812	21 Feb - 1 Nov	< 0	< 0	--	--
	M5	-38.586	178.769	19 Feb - 30 Oct	< 0	< 0	--	--
Not analyzed	M3	-38.594	178.778					
	C8	-38.622	178.562					

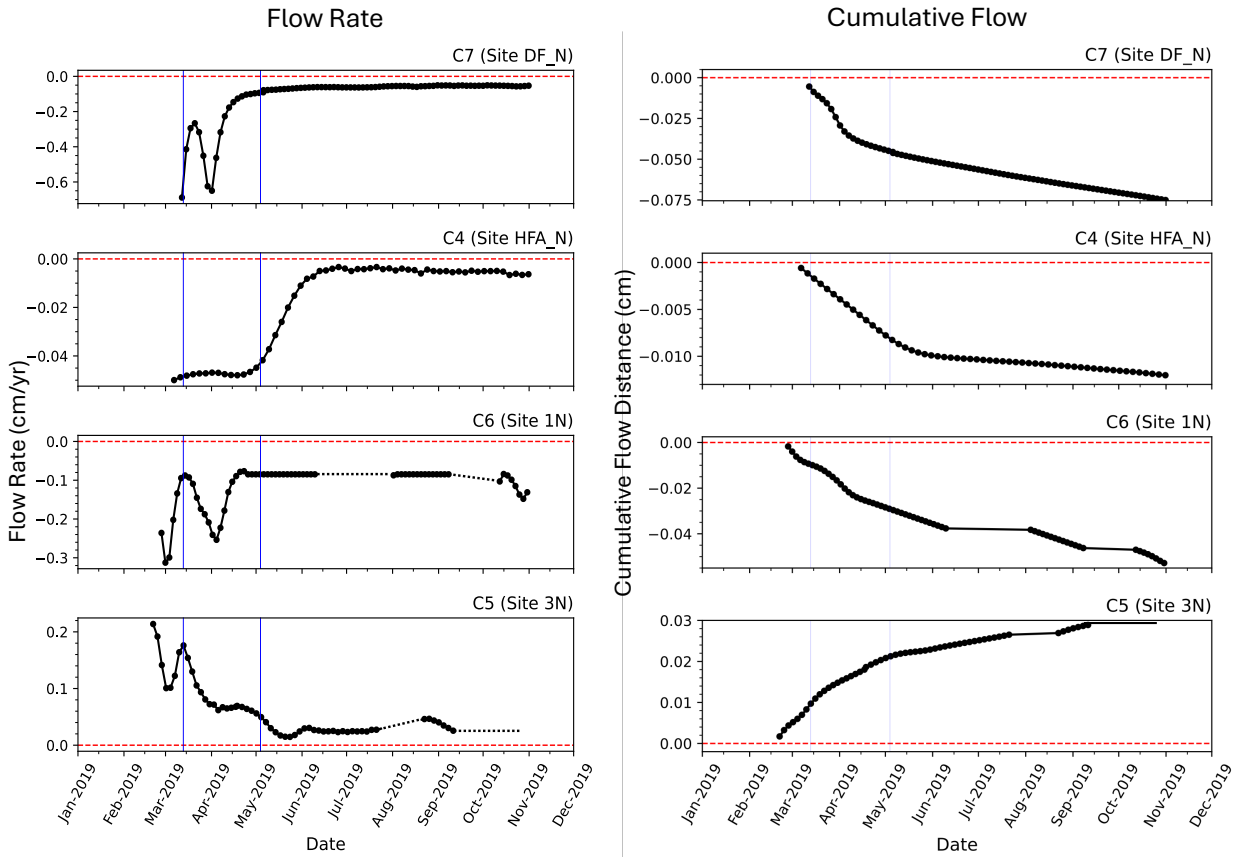

Figure 3.2. Flow rate and cumulative flow time-series of diffuse flow records.
Flow rate of 0 cm/yr and flow distance of 0 cm are shown as red dashed lines. Timing of the 2019 Gisborne SSE is shown with light blue lines. Dotted line segments in flow rate records of C5 and C6 represent discrete periods where instantaneous flow rates are not resolvable due to high-frequency flow oscillations.

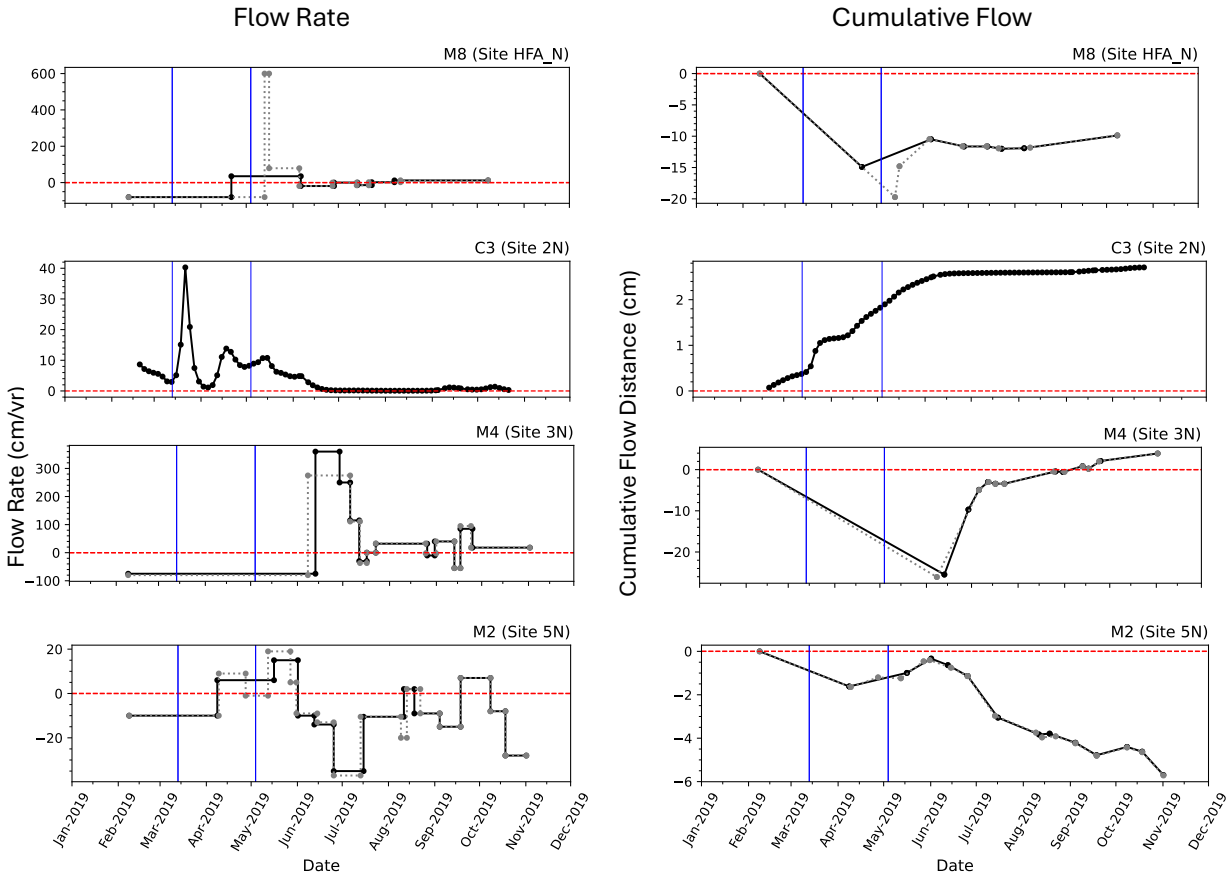

Figure 3.3. Flow rate and cumulative flow time-series of focused flow records. Flow rate of 0 cm/yr and flow distance of 0 cm are shown as red dashed lines. Timing of the 2019 Gisborne SSE is shown with light blue lines. Instantaneous flow rate results for MOSQUITOs are non-unique; two possible solutions are shown for each MOSQUITO. Note there is evidence of high frequency oscillations in the C3 record over a two-week period after the SSE; this does not impact the overall net flow or our interpretations.

3.5 Secular Strain

Downward flow throughout the analyzed period and negative net flow characterize diffuse flow records on the lower slope (C4, C6, C7). In contrast, C5 on the mid-slope records upward flow throughout the analyzed period and positive net flow. These results suggest broad-scale contrasting strain states across strike: dilatational on the lower-slope and compressional on the mid-slope from February to November 2019 (**Fig. 3.4**). Net compression on the mid-slope is consistent with previous interpretations of strong locking during the inter-SSE period and SSEs

accommodating the majority of plate motion in the slow slip source area (Wallace, 2020; Woods et al., 2024). Dilatation on the lower-slope and at the trench are consistent with creep on the shallow megathrust extending from the deformation front to landward of Site U1518, compatible with frequent small pressure transients recorded at Site U1518 (**Fig. 3.1b**). Unfortunately, the gap in instrumentation between the lower-slope and mid-slope regions (**Fig. 3.4**) prevents us from further defining the transition from the dominantly-locked to dominantly-creeping portions. Nonetheless, our long-term records of diffuse flow serve as highly sensitive indicators of secular strain, providing constraints on offshore interplate coupling that is not well resolved by onshore instrumentation and is essential for the assessment of seismic and tsunami hazards.

3.6 Poroelastic Response to Slow Slip

Based on our observations at diffuse flow locations, we postulate that rapid changes in fluid flow rate reflect transient strain signals caused by deformation of the upper few meters of sediment. A general conceptual model is that slip along a subseafloor fault causes a propagating dislocation. The associated stress field induces horizontal strain, impacting fluid pressure gradients and driving vertical flow into and out of the seafloor, akin to a saturated sponge being tectonically squeezed and released (Moore and Vrolijk, 1992). The induced horizontal strain and pore pressure changes are coupled and reversible, and hence are termed the “poroelastic” response (e.g., Kümpel, 1991).

Flow rate peaks first occur at the beginning of our record (mid-February to early-March; **Fig. 3.2**), concurrent with subtle eastward displacement on onshore GNSS time-series (**Fig. 3.1c**). These results are consistent with the initiation of the slip event in mid-February. Flow transients then occur in mid-March to April **(Fig. 3.2**), during the period of recorded maximum displacement at GNSS stations and observed pressure increases in borehole observatories. To

assess whether the flow transients we observe during the SSE at diffuse flow sites (C4, C5, C6, and C7) are compatible with slow slip strain signals, we do a basic calculation of the strain required to produce the observed flow (methods). We perform this calculation using the peak flow rate observed between 13-March – 4-May (**Table 3.1**), when the majority of SSE deformation is recorded at GNSS station MAKO (**Fig. 3.1c**). Assuming flow across the sediment water interface relieves the pore pressure changes caused by strain, we estimate a positive pressure step of 0.6 kPa at C5 and negative pressure steps of 0.1, 0.6 and 1.6 kPa at C4, C6 and C7, respectively. These pressure steps correspond to volumetric strains of +0.1, -0.03, -0.2, and -0.4 microstrain at C5, C4, C6, and C7, respectively. The magnitude of these estimates is comparable to the pressure steps observed at U1518 and U1519 (**Fig. 3.1c**) as well as pressure-strain calculations at other margins following slow slip (Davis et al., 2009; 2011). Thus, this first-order calculation supports our interpretation that flow transients are compatible with signals of volumetric strain.

The upward flow transients, and thus positive pressure and strain signals, at C5 on the mid-slope are consistent with the ~0.5 kPa pressure increase observed at Site U1519 during the SSE and indicative of compressional strain. However, downward flow transients (negative pressure and strain signals) over a large area on the lower-slope during the SSE, which indicate dilation, are inconsistent with the pressure increase at U1518 and appear counterintuitive in an accreting outer-wedge deforming via thrust faulting. Rather than propagating along the décollement out to the trench, this result could indicate that shallow slip occurs along a splay fault in the outer-wedge. If the lower-slope sites are located in the footwall of the slip plane, or if throw along the Pāpaku fault (drilled at U1518) reduces stress and lateral compression in the outer-wedge, we could envision dilatation resulting at the seafloor (e.g., Davis et al., 2015).

Alternatively, it is possible that the observed dilatation is a result (direct or indirect) of subduction of the Pāpaku Seamount, imaged beneath the mid-slope region (Bangs et al., 2023). Mixed lithologies and geometric complexity of the plate boundary (e.g., Barnes et al., 2020), as well as distributed deformation including pervasive brittle fracture of the upper plate and stress shadowing of trailing sediment are thought to result from seamount subduction (Wang and Bilek, 2014; Ruh et al., 2016; Bangs et al., 2023; Saffer and Wallace, 2015; Sun et al., 2020a, 2020b). Hence, seamount subduction leads to significant spatial variations in tectonic loading and stress field that we posit could manifest as dilatation near the trench. We postulate that these mechanisms might enable the downward flow transients observed at C4, C6, and C7, but note that a fully-coupled poroelastic model (e.g., LaBonte et al., 2009) is required to make robust quantitative estimates of the deformation that best explains the flow rate time-series.

Overlain on the background flow and resolvable transient strain signals, flow records from CATs C5 and C6 exhibit periods of high-frequency oscillations in instantaneous flow polarity that exceed our sampling resolution. While we have confidence in the net flow direction and qualitative flow magnitude during these intervals (C5 remains upward at low rates and C6 remains downward at low rates), we cannot resolve instantaneous flow rates. We infer that these signals are caused by bio-turbation/bio-irrigation. Because the CAT fluid collection chambers have a large seafloor footprint, they are vulnerable to organisms burrowing beneath them and disrupting flow signals. Clams observed during ROV operations at C5 and shrimp at C6 are potential culprits, as well as organisms with less apparent surficial expressions like urchins and polychaetes.

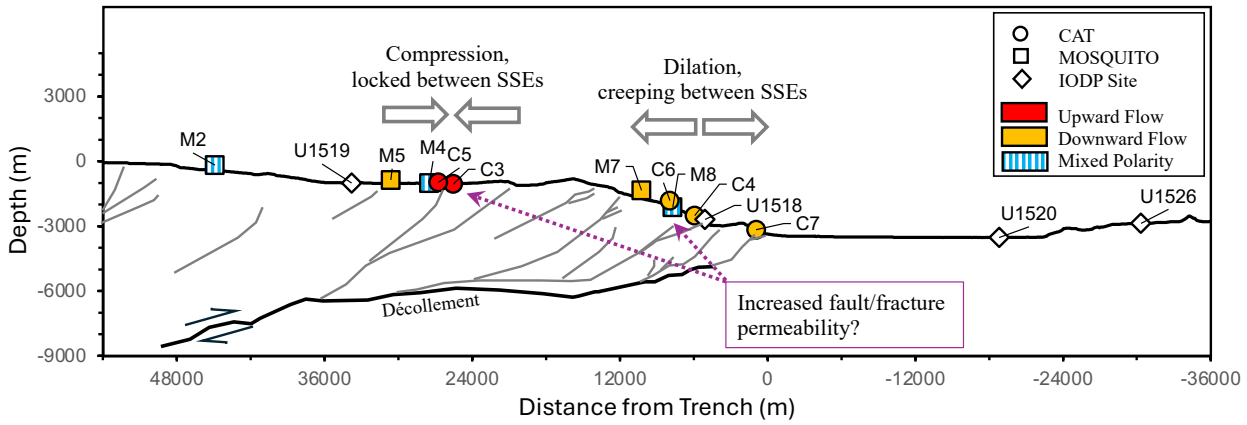

Figure 3.4. Cross section with interpretations.
Cross section based on seismic reflection line 05CM-04 along the IODP Exp. 375 drilling transect. Flow meter locations and interpretations projected onto the cross section. Structural interpretations from Barker et al., (2018), Wallace & Saffer et al., (2019).

3.7 Permeability Response to Slow Slip

At seep sites, fluid flow focused along permeable pathways (e.g., fault zones, fractures) is expelled at the seafloor at higher rates than permitted by typical slope sediments with low hydraulic conductivity (e.g., Sun et al., 2020, Lauer and Saffer, 2012). Several of our instruments measured flow rates in excess of diffusive or poroelastic signals (10s to 100s of cm/yr), indicative of focused flow. The observed transients likely reflect slip-related permeability changes and non-tectonic seep processes.

Flow rate records at MOSQUITOs M2, M4, M5, and M7 are likely dominated by non-tectonic shallow gas-seep dynamics. Observations of bubble streams emanating from the seafloor, seafloor carbonates, and macrofaunal colonies during ROV dives at these sites are indicative of active gas emission, supporting this interpretation. Records at M2 and M4 are relatively noisy and do not suggest a significant increase in upward flow during the SSE. At M5 and M7, fluid samples lack any tracer, indicating that net downward flow persisted from February to November 2019. We postulate that gas-driven aqueous pumping and/or bio-

irrigation drive rapid outflow and downflow at these sites, as has been observed at seeps elsewhere (Solomon et al., 2008; Tryon et al., 1999; Whorley, 2021). Overall, we cannot say with confidence that flow records from M2, M4, M5 or M7 provide evidence for fault-valving as a direct result of slow slip. If these sites had a permeability response to the SSE, it was masked by shallow gas-driven processes.

Upward flow observed at CAT C3 on the mid-slope peaks in late March at ~40 cm/yr, consistent with the compressional strain response we infer at C5 and an additional hydrologic contribution. We also observe a high-magnitude upward flow peak at MOSQUITO M8 on the lower-slope during or just after the SSE. Both sites lack water column and seafloor indicators of gas seepage, suggesting local fluid emission is water-dominated. Hence, flow rate records at these sites are less influenced by gas dynamics that likely complicate the records of M2, M4, M5, and M7. The peak flow at C3 and M8 exceed reasonable poroelastic signals and correlate temporally with the SSE (**Fig. 3.3, Table 3.1**). Thus, these signals may indicate a permeability response to the 2019 SSE. If these transients reflect enhanced permeability of deep-reaching faults, we could expect the fluids sampled to bear chemical signatures of high temperature/pressure alteration indicative of long-range transport. However, we observe near-seawater B, Li, and Sr concentrations at C3 throughout the 9-month period analyzed (**Fig. 3.5**). The fluid compositions at C3 are consistent with a shallow, compactive fluid source such that permeability changes are restricted to shallow depths and only impact drainage of the upper wedge. This interpretation is in line with those of an extensive sediment coring study that sampled seep sites at the northern margin (Aylward et al., submitted). Alternatively, shallow fluid sources may indicate that slip-related permeability enhancement does not occur regularly or has not been active long enough to drive deep-sourced fluid to the seafloor in this region.

Overall, our results at focused flow sites do not provide conclusive evidence of extensive fault-valving tied the 2019 slow slip event that permits drainage of deep-sourced fluids to the seafloor.

3.8 CONCLUSIONS

Net seafloor fluid flow rates at the northern Hikurangi margin from February to November 2019 suggest contrasting secular strain across strike: dilatational on the lower-slope and compressional on the mid-slope. These observations are consistent with creeping on the shallow megathrust and locking in the slow slip source region in the inter-SSE period. Continuous records of flow rate display transients correlated with the occurrence of a large slow slip event. We infer that these transients reflect local volumetric strain induced by the SSE at diffuse sites, and additionally non-tectonic gas-driven processes and possibly shallow permeability changes at focused flow sites. We postulate that downward flow on the lower-slope during the SSE may indicate that shallow slip propagates along a splay fault or could result from seamount subduction, but follow-on strain modeling is required to validate these hypotheses. We do not observe convincing evidence of wide-spread fault-valving or transport of deeply-sourced fluids to the seafloor during the monitored period, suggesting the 2019 event had a minimal impact on broad-scale megathrust drainage and chemical fluxes at the northern Hikurangi margin.

3.9 METHODS

3.9.1 *Instrument deployment, recovery, and sampling*

Descriptions, photos, and internal diagrams of the two types of benthic fluid flow meters used in this study (CATs and MOSQUITOs) are provided in **Appendix B**.

All CATs and MOSQUITOs included in this study were deployed using the remotely operated vehicle (ROV) *Jason* in early 2019 during expedition RR1901/RR1902 on the *R/V Roger Revelle*. All instruments were recovered using the ROV *ROPOS* in 2021 during expedition TN2102 on the *R/V Tangaroa*. Upon instrument recovery, coils were disconnected from the osmotic pumps, the tubing ends were capped, and coils were stored in a cold room at 4 ˚C. Sampling of each coil was performed at sea within ~1 day of recovery. Coils were systematically cut into discrete intervals 25 cm (CATs) or 45 cm (MOSQUITOs) in length. Fluid was expelled from each tubing interval into a microcentrifuge tube using a small air pump. Aliquots of every fifth sample were preserved in zinc-acetate solution for sulfate analysis. CAT samples were acidified to a pH of 2 with nitric acid; every tenth sample was not acidified. Salinity of every tenth sample for CATs (the non-acidified sample) and MOSQUITOs was measured using a handheld refractometer. Storage containers for MOSQUITO samples were wrapped in aluminum foil to prevent photodegradation of the fluorescein tracer.

3.9.2 *Time-stamping*

We calculate the time duration of a sample as the deployment period (deployment date minus recovery date) divided by the total number of samples up to the midpoint of the diffusive salinity tail (tail is a result of diffusive smearing between sample fluid and ultrapure water pre-filled in the sample coil). CAT meter sample durations range from ~1.4 – 2.2 days; MOSQUITO

sample durations range from ~3.3 – 6.4 days. Each sample is then time-stamped using the midpoint of the calculated duration. The start date of the flow rate records varies between instruments given different deployment dates and pump rates.

Diffusive smearing, which results in decreased temporal resolution, varies in extent both 1) within an individual sample coil (fluid collected early in the deployment period sits in the sample tubing longer and thus the diffusional length will be longer relative to fluid collected later in the deployment) and 2) between sample coils (depending on pump rate, in situ effective diffusion coefficient of the tracer, deployment duration, and sample tubing inner diameter; e.g., Jannasch et al., 2004). We estimate that a step change in tracer concentration would diffuse outward ~125 cm (5 samples) in either direction in CAT coils early in the deployment and ~100 cm (4 samples) at the end of the deployment. Throughout the deployment period, diffusive smearing in MOSQUITO coils impacts a maximum of ~2 samples on either side of a step change in concentration.

3.9.3 *Sample analyses*

CAT meter samples were diluted with 2% nitric acid solution and analyzed using a Perkin Elmer 8300 inductively coupled plasma optical emission spectrometer (ICP-OES) or a Thermo Scientific iCAP RQ inductively coupled plasma mass spectrometer (ICP-MS) for concentrations of Rb (tracer), B, Li, Sr, and Ba. Samples were spiked with In to correct for instrumental drift. Measurements were calibrated daily against a series of dilutions of an in-house multi-element solution prepared from certified reference standards. Analytical precision was generally <3% for all solutes based on replicate analyses of check standards. We do not report Ba data because low dissolved Ba concentrations were often below the detection limit of our method and because sampling in oxygenated conditions likely caused some dissolved Ba to

precipitate out as barite ($BaSO_4$). Every-other sample was analyzed for both coils of each CAT meter (temporal resolution of ~2.7-4.3 days without accounting for diffusion).

MOSQUITO samples were analyzed for fluorescein (tracer) concentration using a Cary Eclipse Fluorescein Spectrophotometer. Calibration using a series of dilutions of an in-house stock solution made from certified fluorescein sodium salt was performed daily. Analytical precision was typically <5%. Every sample of at least one coil was analyzed for each MOSQUITO (temporal resolution of ~3.3-6.4 days without accounting for diffusion).

3.9.4 *Flow rate and net flow*

Each CAT meter has two sample coils (**Fig. B1**) and hence two sample sets: one set from the coil located upstream of the tracer injection point and the other set from the coil downstream of tracer injection. The Rb (tracer) concentration in both sample sets will co-evolve through time with flow polarity and flow rate.

For periods of low flow (volumetric flow rate, q, is less than the osmotic pump rate of the upstream coil, P_x), we calculate flow rate, Q, as (Tryon et al., 2001):

$$Q = \frac{P_x}{A}(1 - f_x) \tag{3.1}$$

where A is the cross-sectional area of the collection chamber and f_x is the fraction of tracer in the sample from the upstream coil (C_{sample}/C_{tracer} where C is the tracer concentration).

For periods of higher flow (volumetric flow rate, q, is greater than the osmotic pump rate of the upstream coil, P_x), we calculate flow rate as (Tryon et al., 2001):

$$Q = \frac{1}{A}\left(\frac{P_x}{f_y} + \frac{P_y}{f_y} - P_y\right) \tag{3.2}$$

where P_y is the pump rate for the downstream coil and f_y is the fraction of tracer in the sample from the downstream coil.

We can use the above equations to calculate flow rate only when the following is true: a sample from one coil contains either no tracer solution or all tracer solution, and the corresponding sample from the other coil contains a mixture of tracer and pore water or seawater. Flow rates are unresolvable during time periods when corresponding samples from each coil of a CAT meter contain a mix of tracer and pore water or seawater. However, the difference in tracer concentration between corresponding samples can be used to determine dominant flow polarity. These periods likely reflect flow oscillations occurring at a higher frequency than our sampling resolution can resolve and are shown as dotted lines in flow rate plots (**Fig. 3.2**). There is evidence of similar high frequency oscillations in the C3 record over a two-week period after the SSE.

Following the method in Solomon et al., (2008), MOSQUITO flow rates are estimated for a given coil by matching the time-series of measured fluorescein (tracer) concentration to forward-modeled concentrations considering advection and diffusion. We model tracer concentration, C, as a function of depth and time as (Baetsle, 1969):

$$C(z,t) = \frac{C_0 V_0}{8(\pi t)^{\frac{3}{2}}\sqrt{D_s}} \times \exp\left(-\frac{(z-v_z t)^2}{4D_s t}\right) \quad (3.3)$$

where C_0 is the concentration of tracer injected; V_0 is the volume of tracer injected; t is time; D_s is the sediment diffusion coefficient; z is depth; and v_z is the flow rate in the vertical direction, which is solved for numerically. The depth, z, is the vertical distance from the injection point to the sampling port. The sediment diffusion coefficient, D_s, is calculated from the molecular diffusion coefficient, D_m, and tortuosity, θ^2, where D_m is estimated following Wilke and Chang (1955) and tortuosity is estimated from porosity following Boudreau, (1996). This approach assumes that tracer is injected as a point source mass into an infinite porous medium with no

other tracer sources or sinks. This 1-D analytical solution does not consider horizontal flow but does take into account horizontal diffusion.

All MOSQUITO tracer concentrations that were modeled had positive values of z. That is, the sampling port was located above the tracer injection point because the sampling needle was shorter than the injection needle (**Fig. B2**). As a result, instantaneous flow rate estimates are only possible once tracer has traveled upward (via diffusion and/or advection) and reached the sampling port. Thus, if net downward fluid flow occurs such that tracer arrives at the sampling port later than it would in a purely diffusive setting, we can only estimate the net downward flow rate during that period. Once tracer arrives at the sampling port, we can model instantaneous flow rates, but solutions are non-unique. We present two flow rate time-series solutions for each MOSQUITO (**Fig. 3.3**), both of which fit the measured tracer data (**Fig. 3.10-3.12)**.

For both CATs and MOSQUITOs, net flow distance is calculated as the product of the modeled flow rate and the duration of that flow rate, summed over the entire record. Notably, the net flow distance is a unique solution for MOSQUITO records even though instantaneous flow rate is non-unique.

3.9.5 *Strain calculations*

To assess whether the flow transients we observe at diffuse flow sites during the SSE are compatible with slow slip strain signals, we do a basic calculation of the strain required to produce the observed flow.

We first calculate the pressure gradient, $\frac{\partial P}{\partial z}$, at the seafloor during peak flow using Darcy's Law:

$$q = -\frac{k}{\mu} \cdot \frac{\partial P}{\partial z} \tag{3.4}$$

where q is the observed peak flow rate during the SSE (**Table 3.1**); μ is the in situ fluid viscosity calculated using water temperature measured by ROV during instrument recovery and using a typical fluid sample salinity of 34 measured shipboard using a handheld refractometer; k is the permeability calculated using a permeability-porosity relationship based on compaction experiments on IODP Sites U1519 and U1520 samples (D. Saffer, pers. comm.); P is pressure; and z is depth.

We then calculate the pressure step, P_0, required to generate the pressure gradient, $\frac{\partial P}{\partial z}$, calculated from Equation (3.4) from (Carslaw and Jaeger, 1959):

$$\frac{\partial P}{\partial z} = \frac{P_0}{\sqrt{\pi c t}} \tag{3.5}$$

where c is the hydraulic diffusivity calculated following equations in Wang and Davis (1996) and Van der Kamp and Gale (1983) and assuming a Poisson's ratio of 0.49 (Hamilton, 1979; L'Esperance et al., 2013); and t is time. We report results at $t = 0.75$ days, approximately the midpoint of one sample.

Finally, we calculate strain, θ, from the pressure step obtained from Equation (3.5) as (Davis et al., 2009):

$$\theta = \beta_m \left(\frac{1}{\gamma} - \alpha_m\right) P_0 \tag{3.6}$$

where β_m is the compressibility of the matrix frame calculated from the Bulk modulus, γ is the 3D loading efficiency, α_m is the effective stress coefficient, and P_0 is the pressure step. Elastic properties are calculated following equations in Wang and Davis (1996), Van der Kamp and Gale (1983), and Davis et al., (2009).

3.10 Acknowledgements

This work is supported by NSF award OCE-1753617. We thank the science parties, captains, and crews of the *R/V Revelle* and *R/V Tangaroa*, and the ROV *Jason* and ROV *ROPOS* teams for making the deployment and recovery of the flow meters possible. Special thanks to Theresa Whorley for assistance preparing flow meters for deployment, and Demian Saffer for advice on strain calculations. We thank Reese Miller and Maddy Chriest for helping with sample analyses. Thanks to Jess Hillman, Sarah Seabrook, and Neville Palmer for coordinating onshore logistics and assisting with shipboard sampling.

3.11 EXTENDED DATA

3.11.1 *CAT meter fluid chemistry*

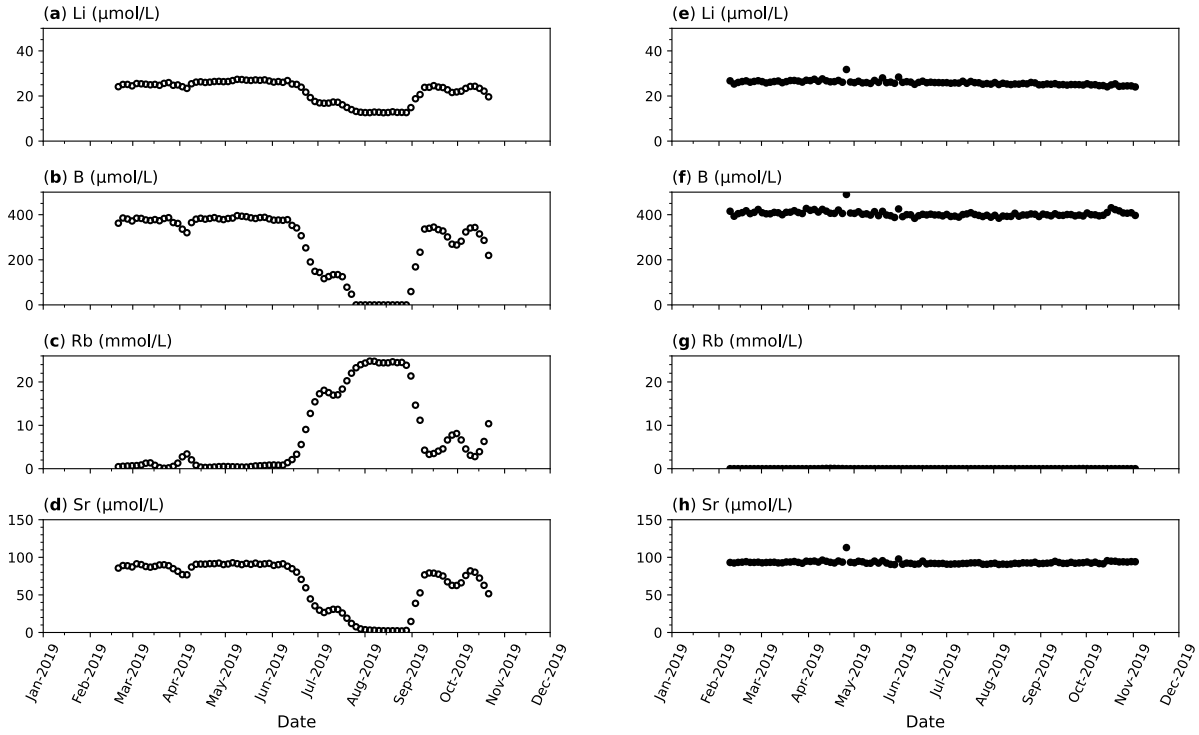

Figure 3.5. Fluid chemistry over time for CAT C3.

(a-d), Chemistry of Coil 1 (upper coil). (e-h), Chemistry of Coil 2 (lower coil). Rb concentration is used for flow rate modeling; the concentration of Rb in undiluted tracer solution is 25.4 mM. Note there is evidence of high frequency oscillations in the C3 record over a two-week period after the SSE; this does not impact the overall net flow or our interpretations.

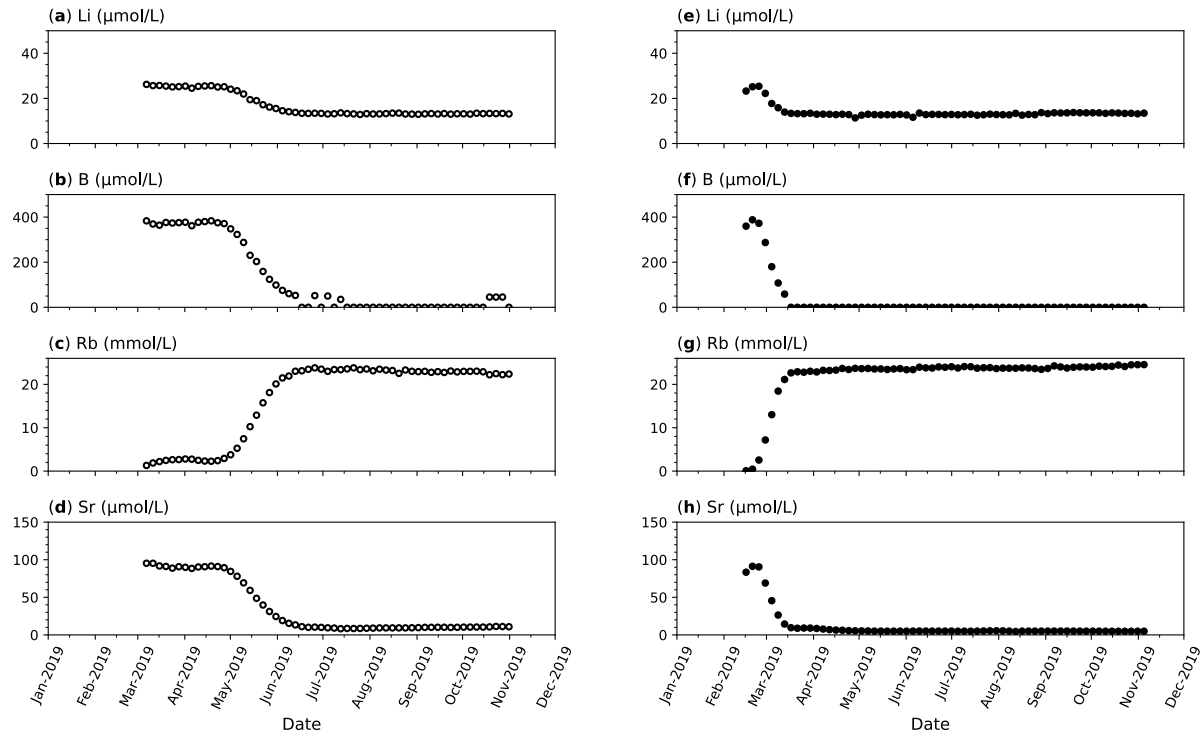

Figure 3.6. Fluid chemistry over time for CAT C4.
See caption of Figure 3.5 for further information.

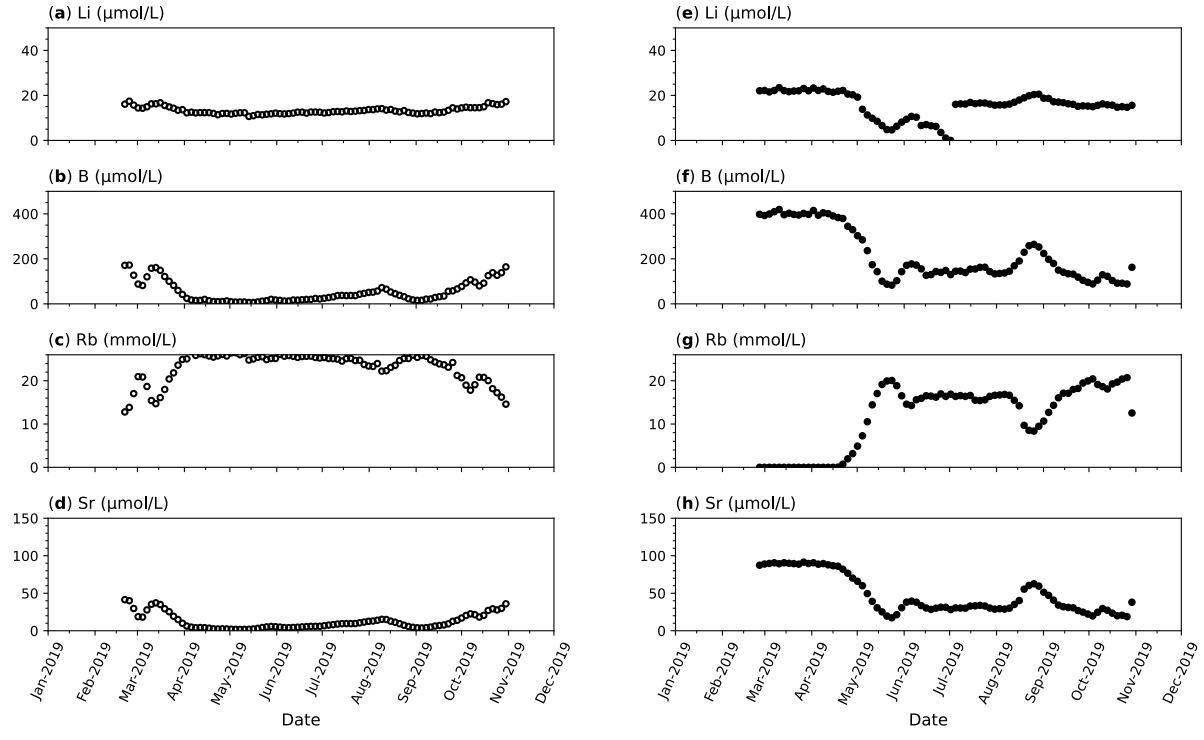

Figure 3.7. Fluid chemistry over time for CAT C5.
See caption of Figure 3.5 for further information.

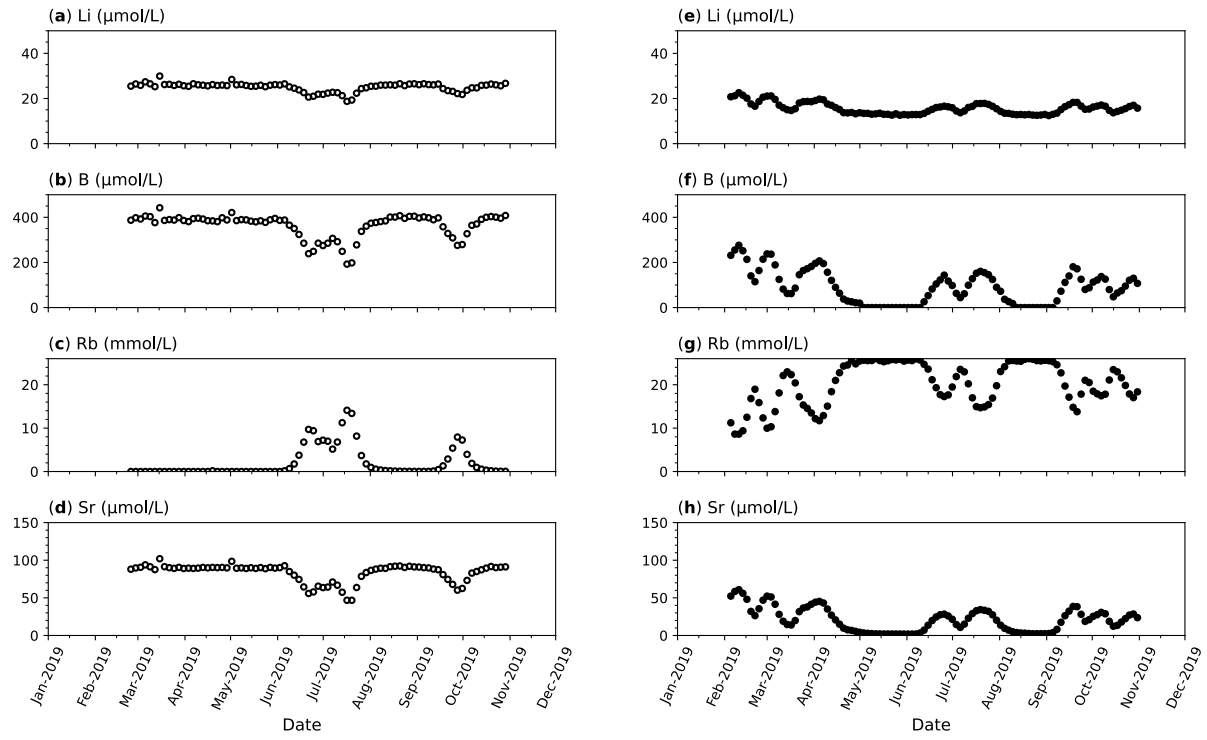

Figure 3.8. Fluid chemistry over time for CAT C6.
See caption of Figure 3.5 for further information.

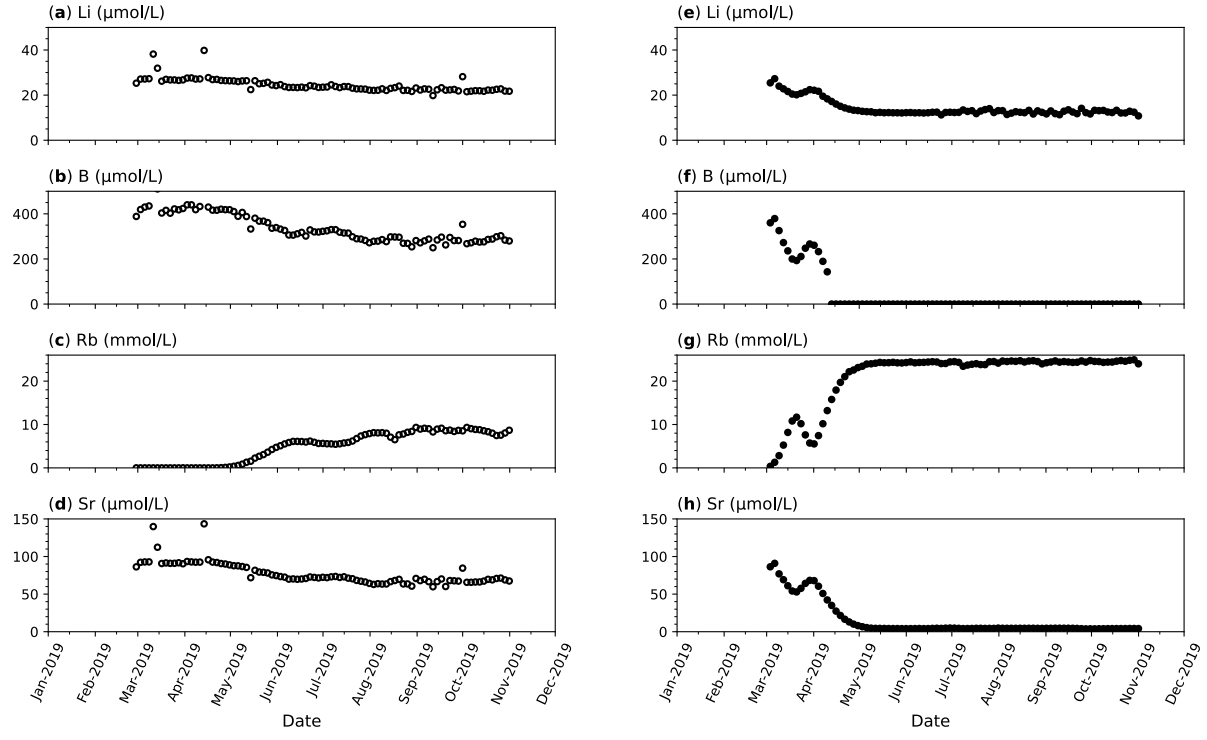

Figure 3.9. Fluid chemistry over time for CAT C7.
See caption of Figure 3.5 for further information.

3.11.2 *MOSQUITO fluid chemistry*

Chemistry data for MOSQUITOs M5 and M7 are not shown. Samples from these instruments did not contain any tracer.

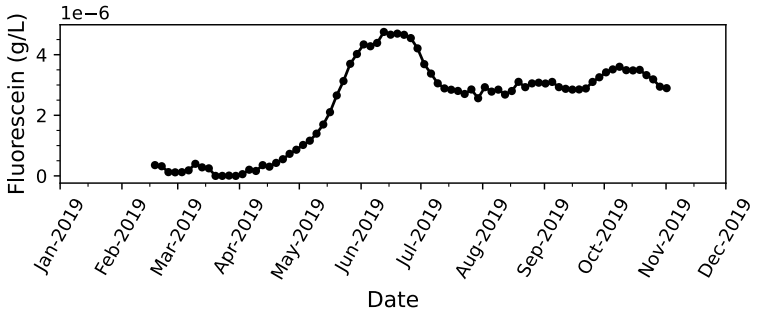

Figure 3.10. Fluorescein concentration over time for MOSQUITO M2 (Coil 1, 14.8 cm above tracer injection point).

Fluorescein concentration is used as the tracer for flow rate modeling; 0.05 mL of tracer with fluorescein concentration of 9.983 g/L was injected into the sediment upon instrument deployment.

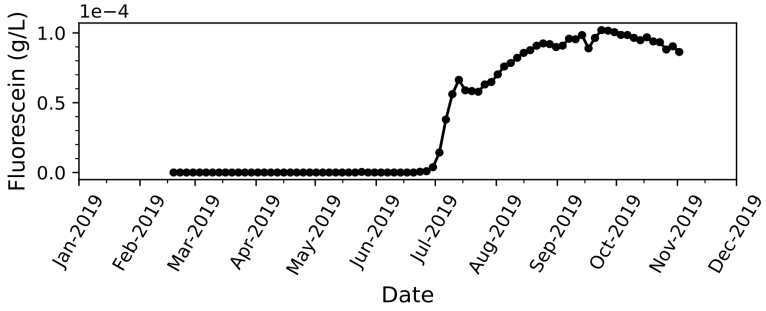

Figure 3.11. Fluorescein concentration over time for MOSQUITO M4 (Coil 3, 5 cm above tracer injection point).

See caption of Figure 3.10 for further information.

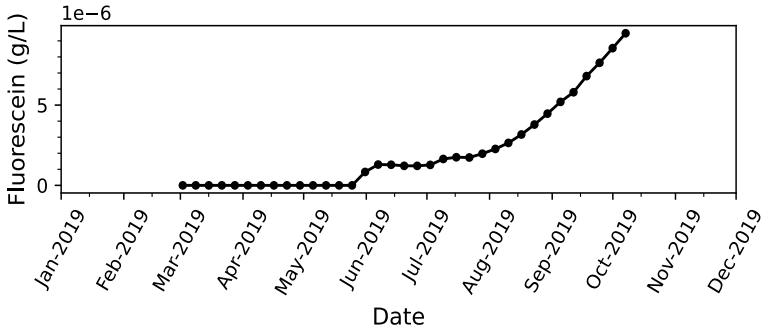

Figure 3.12. Fluorescein concentration over time for MOSQUITO M8 (Coil 3, 4.8 cm above tracer injection point).

See caption of Figure 3.10 for further information.

Chapter 4. RAPID DRAINAGE OF SUBDUCTING SEDIMENTS AT PYTHIA'S OASIS SEEP IMPACTS GEOMECHANICS AND FOREARC GEOCHEMICAL FLUXES AT THE CENTRAL CASCADIA MARGIN

*This chapter will be submitted to a journal with the following author list:
I. Aylward, E. A. Solomon, R. N. Harris, M. E. Torres, D. S. Kelley

4.1 ABSTRACT

Seeps are underwater springs where subsurface fluids are emitted at the seafloor. They are ubiquitous along the forearc of subduction zones worldwide. Chemical characterization of seep fluid compositions, in concert with visual and geophysical investigation, allows for assessment of their fluid sources and flow rates, and in so provides insight into broad scale hydrogeologic conditions, geochemical cycles, and geo-mechanical processes. This study presents geochemical and thermal data from the "Pythia's Oasis" seep site that indicate focused drainage of the megathrust and subducting sediment section within the Cascadia margin offshore of central Oregon. At the primary emission site ("Pythia"), warm (~12˚C), highly altered fluids are discharged at a rate of ~2–30 cm s^{-1}. Elevated heat flow values at Pythia (260 mW m^{-2}) and a near-by emission site called "Blow Out" (212 mW m^{-2}) are consistent with high water discharge. Geochemical analyses of the emitted fluids reveal extreme enrichment in B (6660 µM), Li (202 µM), and Sr (1190 µM), depletion in Cl (340 mM), non-radiogenic strontium ($^{87}Sr/^{86}Sr$ = 0.7066), crustal helium ($^{3}He/^{4}He \leq 0.67\ R_A$), and the presence of ethane and propane. These chemically and isotopically distinct values reflect fluid source temperatures of ~170 ˚C–250 ˚C, with fluids sourced above basement, within or below a carbonate-rich underthrust sediment

section (≥ 4 km depth). Persistent, rapid expulsion of highly altered fluids at Pythia's Oasis indicate that inefficient drainage of subducting sediments near the deformation front and/or funneling of fluid from a large catchment area into a high-permeability conduit (likely the Alvin Canyon Fault), result in long-distance focused fluid transport and significant solute fluxes to the ocean. Hence, high volumetric discharge at this mid-slope seep may be indicative of permeability changes that influence broad-scale margin characteristics and indicates that subduction zone seeps may be more important for marine geochemical cycles than previously considered.

4.2 Introduction

Marine cold seeps are the seafloor manifestation of focused fluid flow from the subsurface. Seeps occur globally along subduction zone forearcs (Suess et al., 2014), commonly coinciding with deep-reaching fault zones that in some instances provide pathways for focused fluid flow through low-permeability wedge sediments from plate boundary depths to the seafloor (e.g., Kastner et al., 2014; Lauer & Saffer, 2012; Moore et al., 1991; Ranero et al., 2008; Sun et al., 2020). Thus, seep fluid characteristics can be used to examine processes occurring both near the seafloor (e.g., geochemical fluxes across the sediment-water interface and sediment-animal-microbe interactions in vent ecosystems), and to infer processes occurring at depths that are out of reach of sampling and in situ measurements. Specifically, detailed geochemical, geophysical, and visual characterization of seeps and venting fluids can inform on the thermal structure of subduction megathrusts and wedge sediments, and the distribution and evolution of pore fluid pressure in the outer forearc (e.g., Suess et al., 1998).

The composition of pore fluids discharging at seeps are typically altered from seawater. While shallow, compaction-derived fluids are of seawater origin, chemical reactions, solute

diffusion along concentration gradients, and mixing with fluids of other sources (e.g., dehydration-derived fluids) alter their nature and composition during sediment diagenesis. The primary diagenetic reactions that modulate pore fluid composition in outer forearc settings include organic matter degradation, gas hydrate formation and dissociation, carbonate precipitation and recrystallization, ion exchange, opal and clay dehydration, and alteration of reactive silicates (e.g., volcanic ash) and upper oceanic crust (e.g., Kastner et al., 1991; Kastner et al., 2014). These processes progressively alter the composition of pore fluids during burial such that pore fluids become increasingly "exotic" with increasing depth and temperature. In general, typical characteristics of deeply-sourced fluids resulting from the above reactions include low Cl and K, high B and Li concentrations, the presence of thermogenic hydrocarbons, and anticorrelated oxygen and hydrogen isotope ratios (Kastner et al., 2014).

As fluids ascend toward the seafloor, diffusion, continued reaction, and mixing with shallow pore fluids further affect fluid composition, particularly at low fluid transport rates. Rapid transport along high-permeability conduits minimizes chemical over-printing by shallower signals. Thus, the chemical and isotopic composition of fluid expelled at seeps can be used to assess the fluid source (i.e., depth and temperature of formation) and transport path (i.e., subsequent changes experienced) from depth to the seafloor. Additionally, the shape of pore water solute profiles (i.e., changes in solute concentration with depth) can be used to quantify fluid flow rates. Heat flow data are complementary to the pore water geochemical profiles. Spatial variations in heat flow can be used to identify sites of active fluid ventilation that can then be targeted for geochemical sampling (e.g., Aylward et al., in press). Furthermore, heat flow data can be modeled to estimate fluid advection rates (e.g., Hutnak et al., 2007).

Collectively, pore water chemistry and heat flow data at seafloor seeps allow assessment of the origin, transport path, and rate of flow of seeping fluids. These data permit calculation of water and solute fluxes associated with focused fluid flow and provide constraints on subduction zone heat and water budgets. Understanding these budgets is critical: the magnitude and distribution of heat and water in subduction zones are recognized as primary factors in controlling the timing and mode of megathrust slip through their influence on frictional properties and effective stress (e.g., Saffer and Tobin, 2011; Saffer and Wallace, 2015). Further, the transfer of fluids to the ocean through seafloor seeps influences global elemental cycling (e.g., Suess, 2014; Kastner et al., 2014). Hence, chemical and thermal investigation of seafloor seeps afford insight into numerous broad scale processes of scientific and societal relevance.

Seep processes have been studied along the Cascadia subduction zone (CSZ) since the 1980's (e.g., Collier &Lilley, 2005; Han & Suess, 1989; Kulm et al., 1986; Merle et al., 2021; Riedel et al., 2018; Sample et al., 1993; Tobin et al., 1993). However, only a few seep sites have been studied in detail (e.g., Hydrate Ridge, Torres et al., 2002; 2004). A seep unlike any other yet discovered is Pythia's Oasis, located on the Oregon accretionary prism about 20 km landward of the deformation front of the central CSZ (**Fig. 4.1**; Philip et al., 2023). Discovered in 2014, Pythia's Oasis is a ~0.385 km^2 seepage area containing four sites of active fluid expulsion: Promontory, Pythia (also called "Orifice," Philip et al., 2023), Blow Out, and Moat. Preliminary investigations of venting sites at Pythia's Oasis, including limited fluid sampling during two remotely operated vehicle (ROV) dives of opportunity, revealed rapid expulsion of warm (~12 ˚C), highly altered fluids at Pythia, interpreted as focused drainage of overpressured fluids from plate boundary depths **(**Philip et al., 2023).

This study builds upon the initial results of Philip et al., (2023), presenting detailed geochemical and thermal datasets collected in 2019 during a dedicated research expedition on the *R/V Atlantis* (AT42-17). To gain a better understanding of the Pythia's Oasis hydrogeochemical system, fluids from the main vent (Pythia) were directly sampled, and gravity and push cores were collected at each of the four emission sites. In addition, extensive ROV, autonomous underwater vehicle (AUV), and heat flow surveys of Pythia's Oasis were conducted. In this study, the chemical composition of the venting fluid is used to constrain the source depth and fluid formation temperature. Spatial variations in the nature of seepage are then discussed, and estimates are made of water discharge and solute fluxes to the ocean using vent fluid compositions and modeled fluid flow rates. Finally, the implications of focused, long-range drainage are discussed for marine geochemical cycles, and the hydrogeologic conditions and water budget of the central CSZ.

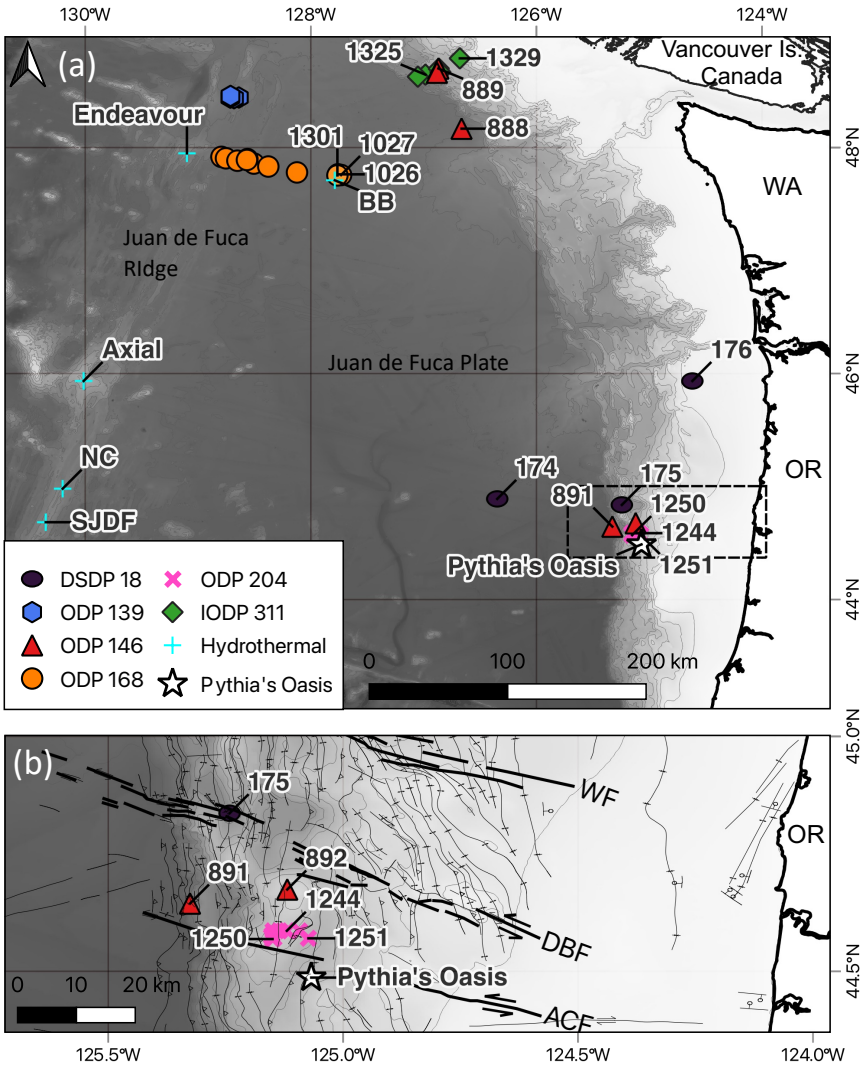

Figure 4.1. Regional map showing location of Pythia's Oasis.
(a) Locations of Pythia's Oasis and scientific ocean drilling and hydrothermal sites in the region. Baby Bare ("BB") is a low temperature hydrothermal site; North Cleft ("NC"), South Juan de Fuca ("SJDF"), Axial, and Endeavor are high temperature mid-ocean ridge hydrothermal sites. (b) Zoom in of area surrounding Pythia's Oasis (box in "a"). Near-by strike slip faults shown as bold black lines (WF = Wecoma Fault; DBF = Daisy Banks Fault; ACF = Alvin Canyon Fault). Structural interpretations from Goldfinger et al., (1992).

4.3 Geologic Setting and Previous Work

Along the CSZ, the Juan de Fuca (JDF) plate subducts eastward beneath North America (**Fig. 4.1a**) with a convergence rate of ~3–4 cm/yr (e.g., Wilson, 2002). A thick incoming

sediment section on the young, hot JDF plate results in a thick accretionary prism and no bathymetric trench. Much of the shallow megathrust along Cascadia is thought to be partially to fully locked, with very low background seismicity during the interseismic period since the last large (M9) megathrust earthquake, which occurred in January of 1700 CE (e.g., Atwater et al., 1995; Wang & Tréhu, 2016).

Pythia's Oasis is located offshore of central Oregon just south of 44.5 ˚N, and is likely co-located with the Alvin Canyon strike-slip fault. Although the Alvin Canyon fault (ACF) is poorly mapped in the region of Pythia's Oasis, the seep site lies within ~5 km of the fault zone, which has an estimated width up to 6 km (Goldfinger et al., 1997). The ACF is the southern-most of three left-lateral, NW-oriented strike-slip faults in central Cascadia (**Fig. 4.1b**). These faults offset both the oceanic crust and wedge sediments, and mark N-S changes in numerous major tectonic characteristics. Nearly full frontal sediment accretion, a deep décollement at the top of the oceanic crust, and a shallow (~4˚) plate dip near the deformation front occur offshore of northern Oregon and Washington (~44.75–47 ˚N; Carbotte et al., 2024; Han et al., 2017; MacKay et al., 1992). Atypical landward-vergent thrust faults (where vergence refers to the direction of transport of the overriding thrust sheet) also characterize this region. A jump up in décollement depth to ~1.5 km above basement, increased plate curvature near the deformation front, and a switch to seaward-vergent thrust faults occur at ~44.5 ˚N (Carbotte et al., 2024; Han et al., 2017). Offshore of Washington, accreted sediments are over-consolidated. In contrast, the thick sediment sequence subducting offshore of central Oregon is thought to be under-consolidated and fluid-rich (Han et al., 2017). These changes correlate with variations in interface seismicity and episodic tremor and slip, current locking fraction, and paleoslip indicators. Relative to northern Cascadia, modeled reduced locking or a narrower locking zone,

increased local microseismicity, decreased non-volcanic tremor, a possible higher frequency megathrust earthquake recurrence interval, and a modeled low-slip region at ~44.5 ˚N for the 1700 CE megathrust event characterize the central Oregon region where the Pythia's Oasis seep site is located (Hyndman and Wang, 1995; McCaffrey et al., 2013; Schmalzle et al., 2014; Walton et al., 2021; Wang and Tréhu 2016).

Pythia's Oasis was discovered in 2014 during a multibeam sonar survey as two bubble plumes rising hundreds of meters into the water column, separated by ~380 m (Philip et al., 2023). Subsequent surveys determined that the seep area hosts four fluid emission sites along a NW-SE trend. Seafloor investigations (Philip et al., 2023) in 2015 and 2016 using the ROVs *ROPOS* and *Jason,* respectively, revealed that Pythia (the primary emission site) is an ~5 cm-diameter orifice emitting warm (11.8 ˚C–12.6 ˚C), sediment-laden, freshened fluid. Fluids collected directly from within the Pythia orifice and pore water from two ROV push cores near the vent revealed a fluid composition that is significantly altered from seawater (e.g., extremely enriched in B and Li relative to sea water values). Analysis of a 2015 *ROPOS* video clip of Pythia indicated that water was being expelled at 10 – 30 cm s^{-1} (Philip et al., 2023). Bottom simulating reflector (BSR) anomalies consistent with long-lived expulsion, together with the anomalous fluid compositions, led Philip et al., (2023) to hypothesize that fluid flow may be channeled from plate boundary depths to the seafloor along the Alvin Canyon fault co-located with Pythia's Oasis. Moreover, calculations by Philip et al., (2023) of the CSZ water budget, and the pore pressures and permeabilities required to support the observed water discharge, implied that strike-slip faults may play a major role in regulating megathrust pore fluid pressure throughout the outer forearc in the central CSZ.

4.4 METHODS

4.4.1 *Sample collection and processing*

During a 2019 expedition onboard the *R/V Atlantis* (AT 42-17), Pythia's Oasis was extensively surveyed and sampled using a hull mounted Kongsberg EM122 multibeam sonar, high-resolution bathymetric mapping with the AUV *Sentry* utilizing a RESON multibeam sonar (400 kHz), photomosaic surveys by *Sentry* and the ROV *Jason*, visual seafloor investigation and vent sampling with *Jason*, gravity coring, and heat flow measurements (**Fig. 4.2, 4.3**). To obtain high resolution (~1 m) bathymetric maps of the area, *Sentry* was flown at an altitude of 30–60 m off bottom. During one ROV dive (J2-1227), *Jason* drove in a grid pattern at ~3–4 m above the seafloor to collect overlapping images of a ~7700 m^2 area centered around Pythia, allowing the production of a high-resolution photo mosaic of the area (**Fig. C1**).

Ten discrete fluid samples were collected from the Pythia vent using Isobaric Gas Tight samplers (IGTs; Seewald et al., 2001) co-registered with temperature and Major Fluid samplers (von Damm et al., 1985; **Fig. 4.2b**). Fluid samples were filtered through a 0.2 μm filter. Salinity was measured shipboard with a Reichert temperature-compensated handheld refractometer and pore water alkalinity was measured by Gran titration following Gieskes et al. (1991). The remaining filtered pore water was aliquoted for shore-based analysis and stored in a cold room at 4 ˚C. Aliquots for sulfate and dissolved Cl measurement were diluted 1:101 in a 0.4893 mM ZnAc solution. For major and minor elements and Sr isotope measurements, aliquots were acidified to a pH of 2 with HNO_3. Subsamples for $\delta^{13}C$ analyses of dissolved inorganic carbon (DIC) were preserved with $HgCl_2$. Untreated aliquots were stored in glass bottles for additional Cl measurements and Cl isotope analyses. Subsamples for $\delta^{18}O$ and δD determination were stored in flame-sealed glass ampoules. Gas samples for hydrocarbon and methane isotope

analyses were preserved in evacuated serum bottles. IGT gas samples for $^{3}He/^{4}He$ analysis were preserved in crimped copper tubes and stored in a cold room at 4 ˚C. The copper tubes were initially flushed with Ultra High Purity N_2 gas, then flushed with 1 volume of sample (~20 mL); the second sample volume was then crimp-sealed.

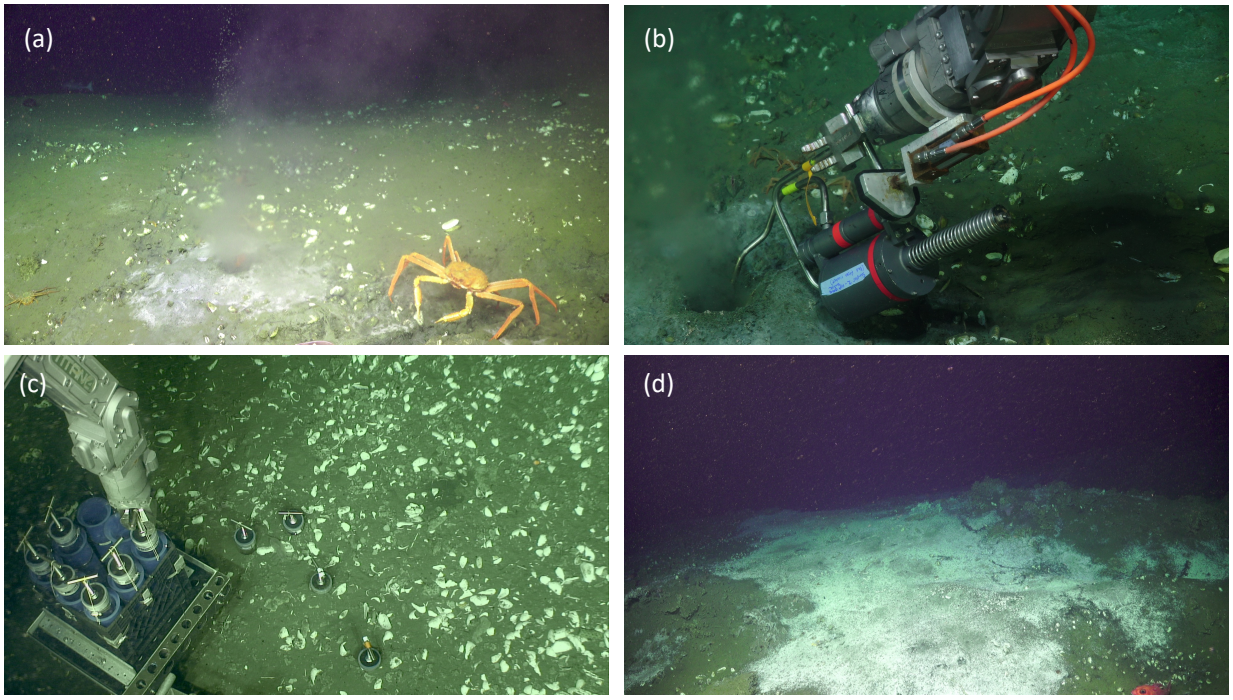

Figure 4.2. ROV *Jason* photos of Pythia's Oasis.
(a) The Pythia vent at the Pythia's Oasis seep site. (b) Sampling Pythia fluids using a Major sampler. (c) Push cores collected in a clam field near the Pythia vent. (d) Extensive bacterial mat and clams near the Blow Out site.

Utilizing the Oregon State University (OSU) MARSSAM coring facility, 21 successful gravity cores (**Table C1**) ranging from 0.4–4 m penetration targeted the four emission sites, with a focus on the area immediately surrounding Pythia. Using the ROV *Jason*, six push cores were collected, four around Pythia and two near the Blow Out emission site (**Table C1**). Gravity cores were cut into 150 cm sections, which were immediately labeled, capped, taped, and stored in a cold room at 4 ˚C until further processing. Sediment from all cores was extruded from the core liner in short intervals (2–10 cm) within ~12 hours of core collection. Two 3 mL sediment plugs

were collected from extruded sediment intervals using a cut-off syringe. Sediment plugs were stored in crimp-sealed glass bottles for follow-on porosity and headspace hydrocarbon analyses. Ten mL of saturated KCl solution were added to hydrocarbon samples, and bottles were stored upside-down. The remaining extruded sediments were squeezed for pore water using titanium squeezers and hydraulic presses. The extracted pore water was then filtered through a 0.2 μm filter. Salinity and alkalinity were measured shipboard, and remaining fluids were aliquoted and preserved for shore-based analysis as described for vent samples collected with IGTs and Major samplers.

Sixty-five heat flow measurements were collected along transects of each emission site using a "violin bow" style multi-penetration heat flow probe. The probe's thermistor string was 3.5-m long, housing 11 equally spaced thermistors that were inserted into the sediment at each measurement location. Heat flow determinations were made using in situ measurements of the thermal gradient and thermal conductivity, based on 1) the decay of frictional heating generated during insertion of the probe, and 2) the decay of a calibrated heat pulse generated by a heating wire in the thermistor string, respectively. All heat flow data were analyzed using SlugHeat (Stein and Fisher, 2001), an interactive set of processing tools. Measurements were conducted every ~80 m along NE-SW trending transects (~1000 m long) across each emission site. An additional ~2700-m-long E-W transect was conducted crossing Pythia (**Fig. 4.3, 4.5**).

4.4.2 *Onshore geochemical analyses*

Major (Ca, K, Mg, Na) and minor (B, Li, Fe, Mn, Sr, Si) constituents of pore water and vent fluid were measured at OSU using a Spectro Arcos ICP-OES. For major element analyses, samples were diluted 1:100 with a 1% nitric acid solution. Dilutions of IAPSO standard seawater were used as calibration standards. Analytical precision of major element analyses was <3%. For

minor element analyses, samples were diluted 1:25 in a 2% nitric acid solution. In-house standards prepared from certified reference standards were used for calibration. Precision of B, Li, Fe, and Mn were <5%, and precision of Sr and Si were ≤6%.

For strontium isotope analyses, acidified pore fluid aliquots were loaded directly onto columns containing EICHROM Sr-Spec® resin; samples from the columns were collected in acid-washed Teflon bottles, acidified with 2 mL of 3% HNO_3 and analyzed using the multi collector inductively coupled plasma-optical emission spectrometer (MC-ICPMS) located in the W.M. Keck Collaboratory for Plasma Spectrometry at OSU. $^{87}Sr/^{86}Sr$ ratios were normalized to the National Bureau of Standards 987 standard, with a $^{87}Sr/^{86}Sr$ value of 0.71025 ± 0.00005 (2σ mean; n=91). External error is represented through replicate analysis of an in-house standard yielding an $^{87}Sr/^{86}Sr$ ratio of 0.708170 ± 0.000051 (2σ mean; n=91). The stable isotopic composition ($\delta^{13}C$) of the dissolved inorganic carbon (DIC) was measured at OSU using a Gas-Bench II automated sampler interfaced to a gas source stable isotope mass spectrometer as described in Torres et al. (2005). The precision of the $\delta^{13}C$ measurements based on replicate analyses of a $NaHCO_3$ in-house standard is better than ±0.1‰.

Sulfate, chloride, hydrocarbons (C_1–C_6), and $\delta^{18}O$ and δD were measured at the University of Washington (UW). Sulfate and chloride were analyzed using a Metrohm 882 Compact ion chromatograph. Calibration standards were prepared from dilutions of IAPSO standard seawater. Analytical precision based on repeat measurements of check standards was <2% and <1.2% for SO_4 and Cl, respectively. For vent samples, Cl was also measured by titration with silver nitrate following the method in Gieskes et al. (1991). Samples were run in duplicate. Analytical precision based on repeat analyses of IAPSO was <0.4%. Hydrocarbon (C_1–C_6) concentrations were measured using a Hewlett Packard 5890 Series II gas

chromatograph. All analyzed headspace samples were collected well below the sulfate-methane transition zone (SMTZ) to ensure no effects from anaerobic methane oxidation. Samples were run in triplicate. Analytical precision was generally <2% for methane, <5% for ethane, and <10% for propane; no higher hydrocarbons were detected. $\delta^{18}O$ and δD (VSMOW) were measured on a Picarro liquid water cavity ring-down spectrometer (CRDS). Reproducibility based on repeat measurements of a reference standard was ±0.4‰ and ±0.09‰ for δD and $\delta^{18}O$, respectively. Sediment porosity was measured at UW for gravity and push core samples by weighing 3 mL sediment plugs before and after drying in an oven for 24 hours at 60 ˚C.

Methane isotope ratios ($\delta^{13}C$-CH_4, δD-CH_4) were measured for two samples at ETH Zurich using a Thermo Fisher Delta V isotope ratio mass spectrometer (IRMS). An in-house CH_4 reference standard was calibrated against Methane #1, #2, #5 and #7 (Biogeochemical Laboratories, Indiana University, USA). The reproducibility of the CH_4 standards was 0.4‰ for $\delta^{13}C$ and 1.3‰ for δD. Reproducibility was 0.6‰ for $\delta^{13}C$ for the IGT sample and 0.1‰ for the pore water sample (core BB2). For δD, the standard deviation was 0.4‰ for the IGT sample and 0.7‰ for the pore water sample. $\delta^{37}Cl$ was determined using the AgCl-CH_3Cl method (Godon et al., 2004) on a duel-inlet gas source mass spectrometer (ThermoFisher Delta XP or Delta V) at the Institut de Physique du Globe de Paris (IPGP). External reproducibility of the Atlantique 2 seawater Cl reference standard was ± 0.025‰.

$^3He/^4He$ was measured at Ohio State University. Gas samples were prepared by attaching the sampling container to an ultra-high vacuum steel line (total pressure $<3 \times 10^{-9}$ torr). Sample gas was purified in vacuo following methods described in Darrah and Poreda, (2012) and then introduced to a Thermo Fisher Helix Split Flight Tube (SFT) mass spectrometer for quantification of isotope abundances. Errors averaged ±0.0091 times the ratio of air (or 1.26 ×

10^{-8}) for $^{3}He/^{4}He$ as determined by measuring the Lake Erie atmospheric air reference material (Darrah et al., 2014) and Scripps Institute of Oceanography MM helium standard (Darrah and Poreda, 2012).

Pore water geochemistry data produced for this study are available through EarthChem Library (https://doi.org/10.26022/IEDA/112771; Aylward et al., 2023). Note that not every analysis was conducted on every sample. Following analyses, the endmember composition (i.e., the fluid composition below the shallow mixing zone) of the vent fluid collected using IGT and Major samplers was estimated based on the measured SO_4 concentrations and assuming conservative mixing between bottom water (SO_4 = 28.9 mM) and SO_4-depleted vent fluids (0 mM). Given that the regional SMTZ is <50 cmbsf, any sulfate in the venting fluid was assumed to reflect shallow fluid entrainment near the seafloor and/or dilution of vent fluid during sampling. Thus, solutes and isotopic ratios in the Majors and IGT samples were cross-plotted vs. SO_4 and endmember concentrations were estimated by extrapolating SO_4 to zero (**Table 4.1**).

4.4.3 *Fluid flow rate modeling*

Estimated fluid flow rates at Pythia were made using *Jason* 4K video collected during the 2019 expedition. The movement of sediment particles suspended within the fluid expelled from the orifice was tracked using *Tacker* 6.1.3, an open-source video analysis and modeling tool. Distances were calibrated using lasers mounted 10 cm apart on *Jason*. Five video clips were analyzed, in which a visible particle was tracked for 20–100 frames to calculate an average particle velocity.

Fluid advection rates outside of Pythia were estimated by modeling pore water Cl profiles from 18 sediment cores (16 gravity cores and two push cores; **Table C1, C2**) using a one-

dimensional finite-difference model (Berg, 2018) that solves the transient advection-diffusion equation run to steady-state,

$$\phi \frac{\partial C}{\partial t} = \frac{\partial}{\partial z}\left[\mathrm{D_s}\phi \frac{\partial C}{\partial z}\right] - \frac{\partial}{\partial z}[(\phi b + \phi v)C] \pm \phi R \qquad (4.1)$$

where C is solute concentration, t is time, z is depth, D_s is the sediment diffusion coefficient, ϕ is porosity, b is pore water burial rate, v is fluid advection rate, and R is the sum of the rates of in situ reactions.

Diffusion coefficients were calculated based on a reference diffusivity (Li & Gregory, 1974) adjusted for tortuosity (estimated from porosity), and a bottom water temperature of 3.3 ˚C (Philip et al., 2023). Sediment tortuosity (θ^2) was calculated from porosity using the following relationship (Boudreau, 1997):

$$\theta^2 = 1 - ln(\phi^2) \qquad (4.2)$$

where ϕ is porosity.

Several simplifying assumptions were made because the cores were relatively short (up to 4 m, but generally < 3 m). Diffusion coefficients were calculated assuming a constant temperature. Pore water burial flux was computed assuming a constant sedimentation rate of 0.015 cm/yr (Torres et al., 2004), and Cl was assumed to be conservative ($R = 0$). A complete list of input parameters is included in **Table C2**.

Estimates of the total volume of water discharged at Pythia were made by multiplying the flow rate by the cross-sectional area of the orifice (assuming a circular orifice of diameter 5 cm; **Fig. 4.2a, 4.2b**). For estimates of the water discharge distal to Pythia, the flow rates at discrete coring sites were extrapolated to the total seepage area. To estimate the total seepage area, visible seepage indicators were identified (bacterial mats, carbonate mounds, and macrofaunal colonies) in the *Jason* photomosaic covering an area of ~7700 m^2 centered at Pythia (**Fig. C1**).

The spatial area of each identified feature was estimated using QGIS (a free, open-source geographic information system software). The overall percentage of the photomosaic area covered by seepage features was then calculated. Using these values, the total seepage area was estimated as: 1) the number of identified seep features multiplied by the average area of each feature type, or 2) the area of hummocky topography surrounding Pythia and Blow Out (**Fig. C1**) multiplied by the calculated percentage of the photo-mosaic covered by seepage features. These two estimates of the spatial area of seepage were multiplied by the average flow rate modeled at coring sites to give an approximation of water discharge outside of Pythia.

4.5 RESULTS

ROV *Jason* temperature probe measurements within the Pythia orifice ranged from 10.7–11.5 ˚C during the 2019 expedition. Over 250 seafloor features indicative of past and/or present fluid seepage were identified during 2019 ROV surveys throughout Pythia's Oasis. These features include bacterial mats, carbonate nodules, pavements, and outcrops, macrofaunal communities (e.g., clams, snails, tubeworms), and bubbles issuing from the seafloor (**Fig. 4.2, 4.3**).

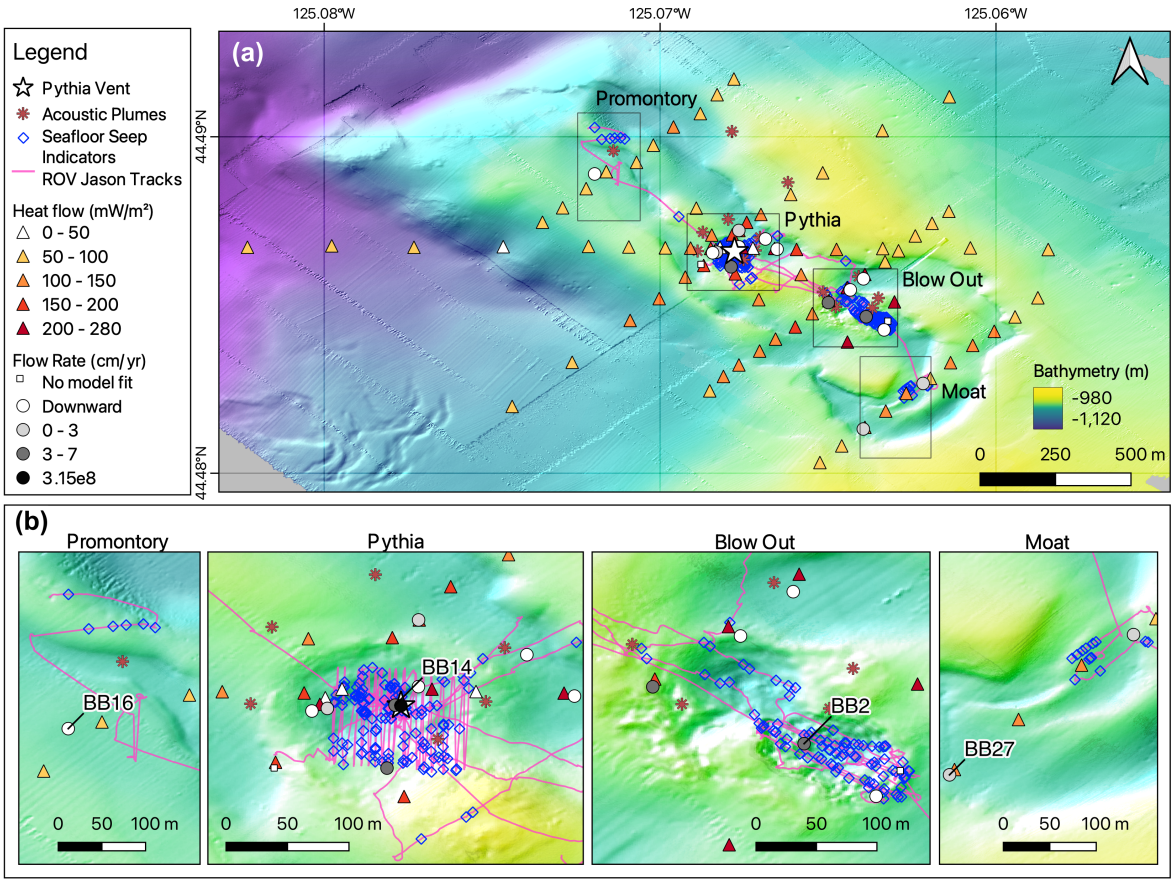

Figure 4.3. Bathymetric map of Pythia's Oasis summarizing observations and results. (a) Map view of Pythia's Oasis showing heat flow results, bubble plumes detected in multibeam surveys (acoustic plumes), and ROV track lines during the 2019 expedition. (b) Zoom-in on the four emission sites, showing flow rate results and observations of seafloor seepage indicators. Location of Pythia is from 2019 observations. Locations of the Promontory, Blow Out, and Moat sites from Philip et al., (2023). The four labeled cores are those shown in Figure 4.5.

A one-meter resolution bathymetric map of Pythia's Oasis compiled from AUV *Sentry* data delineates a nearly continuous depression oriented NW-SE encompassing the four emission sites, covering an area of ~0.385 km^2 (**Fig. 4.3, C1**). Within the depression, gentle hummocky topography surrounds the Pythia and Blow Out sites, whereas the seafloor around the Promontory and Moat sites is relatively smooth (**Fig. 4.3, C1**). Using multibeam data, 14 bubble plumes were identified within and just outside the seep area as defined by the bathymetric depression. These observations, along with the locations of the four emission sites identified in

2015 (Philip et al., 2023), track-lines of all *Jason* dives, and heat flow and fluid flow rate modeling results are summarized in **Fig. 4.3**.

The composition of fluid discharging at Pythia is significantly altered from seawater. Vent fluids are highly enriched in Ca, Sr, B, Li, Mn, Si, and Fe, and depleted in K, Mg, Na, and Cl (**Table 4.1**). The fluids are also isotopically distinct from seawater, with elevated $\delta^{18}O$ and $\delta^{13}C$-DIC, and depleted $\delta^{37}Cl$, δD, and $^{87}Sr/^{86}Sr$ values. In **Figure 4.4,** Sr, Li, and B concentrations and $^{87}Sr/^{86}Sr$ of the Pythia SO_4-depleted endmember are compared with pore water from scientific drilling in the region and vent fluids from several hydrothermal systems located on the JDF plate and spreading center. Despite the shallow sampling depth at Pythia's relative to drilling samples and low fluid temperatures relative to hydrothermal sites, Pythia's fluid compositions are anomalous.

Table 4.1. SO_4-depleted endmember fluid composition from the Pythia vent orifice.
Fluid sampled from the Pythia vent orifice with IGT and Major samplers during ROV dives in 2019. The top and bottom sections display analytes that are enriched or depleted relative to seawater, respectively.

Enriched	**Ca (mM)**	**Sr (µM)**	**Alk (mM)**	**B (µM)**	**Li (µM)**	**Mn (µM)**	**Si (µM)**	**Fe (µM)**	**$\delta^{18}O$ (‰)**	**$\delta^{13}C$ DIC (‰)**
Vent Concentration	51.9	1190	7.35	6660	203	8.27	1045	398	0.118	19.0
SW Concentration	10.55	87	2.325	450	26	0.0003	<100	0.0008	0	0

Depleted	**K (mM)**	**Mg (mM)**	**Na (mM)**	**Cl (mM)**	**$\delta^{37}Cl$ (‰)**	**δD (‰)**	**$^{87}Sr/^{86}Sr$**
Vent Concentration	0.702	4.65	230	341	-0.562	-9.97	0.7066
SW Concentration	10.44	54	480	559	0	0	0.7092

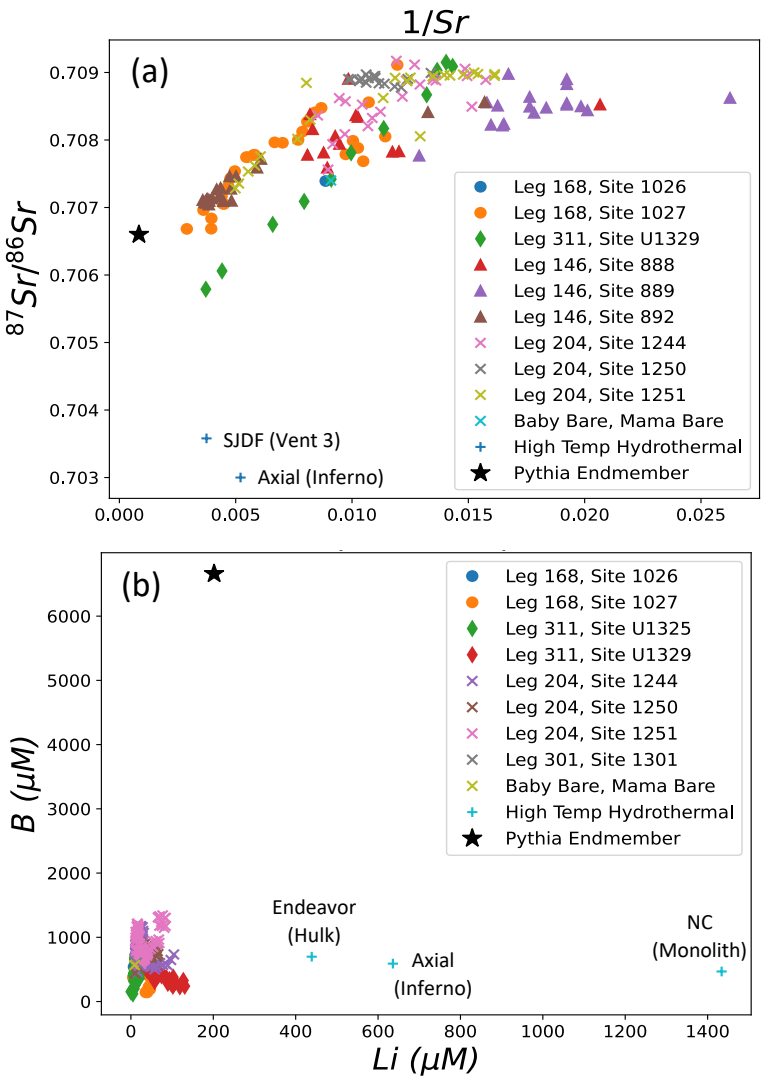

Figure 4.4. Comparison of Pythia fluids with scientific ocean drilling sites and hydrothermal systems in the region.

(a) $^{87}Sr/^{86}Sr$ vs. 1/Sr and (b) B vs. Li of the Pythia SO_4-depleted endmember (Table 4.1), pore waters from scientific ocean drilling sites, and hydrothermal vent fluids in the region. Locations of ODP/IODP sites relative to Pythia's Oasis are shown in Figure 4.1. Note not all sites in Fig. 4.1 have Sr, B, and Li data, so not all are included here. Data are from the following references: Leg 168, Baby Bare (Fisher et al., 2000), Leg 311 (Riedel et al., 2010), Leg 146 (Carson et al., 1992), Leg 204 (Tréhu et al., 2006), Leg 301 (Fisher et al., 2004), SJDF (Von Damm, 1990), Endeavor (Butterfield et al., 1994), Axial (Butterfield et al., 1990), NC (Butterfield & Massoth, 1994).

Hydrocarbon (C_1-C_3) concentrations are enriched relative to seawater. The highest measured pore water (core BB2) concentrations of methane, ethane, and propane are ~5 mM,

0.02 mM, and 0.006 mM, respectively. IGT samples have similar or lower ethane and propane concentrations, but higher methane concentrations (up to ~60 mM). No hydrocarbons heavier than propane were detected. $C_1/(C_2+C_3)$ ratios of all analyzed samples range from ~130 to ~7400. Methane isotopes were analyzed for one pore water sample ($\delta^{13}C\text{-}CH_4$ = -47.6 ‰ and $\delta D\text{-}CH_4$ = -171‰) and one IGT sample ($\delta^{13}C\text{-}CH_4$ = -50.1‰ and $\delta D\text{-}CH_4$ = -178‰). $^3He/^4He$ ratios for IGT gas samples relative to an atmospheric ratio of 1.388×10^{-6} (Wiersberg et al., 2018) ranged from 0.24–0.67 R_A.

The linear flow rate at Pythia is ~2–21 cm s^{-1} based on particle tracking of five video clips from the 2019 expedition (**Table 4.2**). Upward fluid flow rates near the Pythia orifice and from the Blow Out site (estimated by modeling pore water Cl profiles from sediment cores) are ~2–6 cm/yr (**Fig. 4.3, 4.5, Table C1**). Slightly lower rates were estimated at the Moat site (cores BB22 and 27) compared to Pythia and Blow Out. Approximately half of the sediment core sites show evidence of downward fluid flow or irrigation with seawater (concave-up pore water Cl profiles) and are not modeled for flow rate (e.g., BB16 shown in **Fig. 4.5**). Of the cores in which upward fluid flow was modeled, pore water compositions from sediment cores generally trend toward the SO_4-depleted endmember values of Pythia vent fluids with depth. In most profiles, alteration from seawater composition occurs within the top ~10 cmbsf of upward-flow sites (**Table C1**).

Heat flow measured at Pythia's Oasis is anomalously high, with values up to 260 mW m^{-2} relative to background values of 80 mW m^{-2}. Elevated heat flow values tend to occur within the bathymetric depression, with the highest values centered at the Pythia and Blow Out emission sites. Values at the Promontory and Moat sites are only slightly elevated from background (**Fig. 4.3, 4.5**).

4.6 DISCUSSION

4.6.1 *Spatial variations in the nature of seepage*

Variations in heat flow, modeled fluid flow rate, and fluid composition occur throughout Pythia's Oasis. Along the Pythia and Blow Out transects, heat flow values are low outside of the bathymetric depression, then increase to peak values centered roughly on the known emission sites, consistent with focused discharge of warm water (**Fig. 4.3, 4.5**). These observations are consistent with modeled fluid flow rates from sediment core pore water Cl profiles; high upward rates (4.5 – 6 cm/yr) occur near Pythia and the Blow Out (e.g., BB14 and BB2 in Fig. 4.3, **Table C1**). Additionally, four cores taken near Pythia and Blow Out have near-vertical pore water alkalinity profiles near the SO_4-depleted endmember of the vent samples (7.35 mM) and high Ca concentrations throughout the core or increasing with depth (e.g., BB14, BB2 in Fig. 4.5). These profile characteristics indicate that upward advection of low-alkalinity, high-Ca fluids dominates the pore water composition at these sites over ongoing in situ reactions (e.g., anaerobic methane oxidation and carbonate precipitation) and physical circulation processes (i.e., gas-driven irrigation and bioturbation).

In contrast, heat flow increases only slightly within the bathymetric depression along the Promontory and Moat transects with no clear central peak (**Fig. 4.3, 4.5**), indicating diffuse water flow. The two sediment cores taken near the Moat have lower modeled velocities (2–3 cm/yr) than at Pythia and the Blow Out (e.g., BB27 in Fig. 4.5), and the one sediment core taken at Promontory has vertical or concave-upward pore water solute profiles (BB16 in Fig. 4.5), indicating this site is dominated by downward water flow. Low heat flow, along with downward or reduced upward modeled fluid flow rates at the Promontory and Moat sites suggest gas is primarily emitted at these sites and that shallow irrigation of the surface sediment with bottom

water dominates over focused long-range upward advection. The three cores taken near the Promontory and Moat, and downward flow cores outside Pythia and Blow Out, also exhibit increasing pore water alkalinity concentrations with depth (up to 34 mM in BB27, Fig. 4.5) and Ca concentrations that decrease or remain near seawater (e.g., BB16 and BB27 in Fig. 4.5). These characteristics do not reflect focused upward advection of altered fluids, but instead are consistent with gas-dominated emission, shallow seawater circulation, and reactions driven by anaerobic methane oxidation.

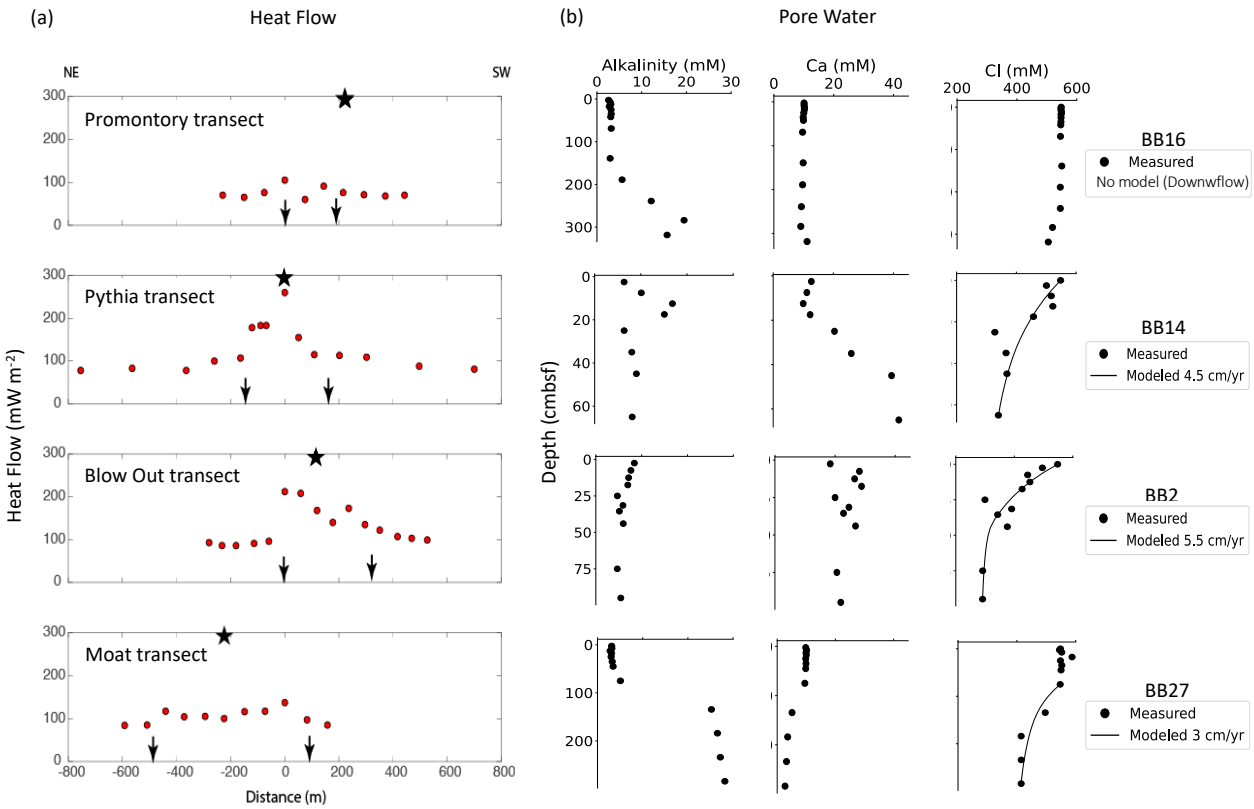

Figure 4.5. Heat flow, select pore water profiles, and flow rate model results at the four emission sites.

(a) Heat flow transects across the four emission sites. Arrows correspond to the edges of the bathymetric depression and stars denote the estimated seafloor locations of bubble plumes. (b) Example pore water alkalinity, Ca, and Cl profiles from sediment cores collected at the four emission sites. Cl profiles show modeled advection rates. Core locations are shown in Fig. 2.3; core locations, model parameters, and model results are included in Tables C1 and C2.

The spatial distribution of heat flow and fluid flow at Pythia's Oasis likely reflects a dynamic shallow permeability structure controlled by the complex interactions of gas hydrate formation, gas-driven fracturing and transient gas emission, shallow seawater circulation, and tectonic forcing, similar to other sites (Bangs et al., 2011; Liu and Flemings, 2006; Solomon et al., 2008; Torres et al., 2002; Tryon et al., 2002). The high flow rate and water-dominated emissions at Pythia and the Blow Out site imply that water transported along the Alvin Canyon fault is focused into discrete, high-permeability (i.e., highly fractured) zones near the seafloor (**Fig. 4.6**). To create water relative permeability that is much higher than gas relative permeability, water funneling must begin well below the base of hydrate stability, where gas saturation is relatively low. Additional funneling within the hydrate stability zone (above the BSR) may continue to focus water flow beneath Pythia and Blow Out (**Fig. 4.6**). Gas-dominated emission at Promontory and Moat implies a cyclic shallow buildup of gas below the BSR until critical buoyancy is reached (i.e., gas pressure reaches lithostatic stress and drives fracturing) and gas can break through, forming a column of free gas migration to the seafloor (e.g., Tréhu et al., 2004; You and Flemmings, 2019). Because of the high gas saturation, water relative permeability is low beneath Promontory and Moat and the flux of gas exceeds the flux of water.

In both the water-dominated and gas-dominated portions of Pythia's Oasis, downward fluid flow and convection of seawater in shallow sediments are also occurring (**Fig. 4.6**), driven by gas dynamics (e.g., Solomon et al., 2008; Tryon et al., 1999) and potentially salinity contrasts between the venting fluid and seawater (e.g., Henry et al., 1996). At locations away from the Pythia vent, vertical pore water profiles at seawater concentration or concave-up profiles indicative of downward flow, indicate the amount of water crossing the seafloor due to shallow seawater circulation is greater than that from long-rage upward flow. However, directly at

Pythia, the chemistry of the venting fluid is similar to, or more altered, than pore water sampled from gravity cores that penetrated below the zone of shallow seawater circulation (upper ~1 mbsf; e.g., Hong et al., 2016). This indicates that shallow circulation is not vigorous enough to significantly dilute the venting fluids, and the upward flow from depth dominates the venting fluid composition at Pythia.

4.6.2 *Fluid source and formation temperature*

The elevated temperatures (10.7–12.6 ˚C at Pythia) and highly altered compositions of fluids discharging at the water-dominated emission sites at Pythia's Oasis indicate a high-temperature source. Based on limited geochemical analyses of two vent fluid samples and two push cores collected in 2015, Philip et al., (2023) estimated a minimum source temperature of 150˚C to 250˚C, placing fluid formation at or near the plate boundary. To confirm and further constrain the source depth and range of possible fluid formation temperatures of Pythia fluids, a full suite of geochemical analyses were conducted on numerous vent and sediment core samples collected during the 2019 *R/V Atlantis* expedition. Source fluids for Pythia's Oasis were constrained by 1) comparing the chemical and isotopic composition of the Pythia's Oasis fluids to pore water chemistry of scientific ocean drilling sites and hydrothermal sites in the region, and results of laboratory experiments, and 2) by utilizing established theoretical and empirical geothermometers.

Dissolved Sr concentrations and Sr isotope results provide the clearest insight into the source depth of the fluids expelled at Pythia's Oasis. Potential source materials of the excess Sr measured at Pythia's Oasis (concentrations are over 13 times higher than seawater values) include continental detritus, ash, biogenic carbonates, and oceanic crust. Given that each potential source of Sr has distinct isotopic signatures, and that there is no measurable

fractionation of $^{87}Sr/^{86}Sr$ during fluid-rock reactions, Sr is recognized as a powerful indicator of fluid source (e.g., Kastner et al., 1995; Solomon et al., 2009; Hensen et al., 2015; Ayres et al., 2020; Teichert et al., 2005).

The $^{87}Sr/^{86}Sr$ ratio of Pythia SO_4-depleted endmember fluid is 0.7066, lower than seawater and most pore water samples from scientific ocean drilling expeditions along the CSZ, but higher than basalt-hosted hydrothermal sites (**Fig. 4.4**). Continental detritus is discounted as the dominant Sr source because it would result in $^{87}Sr/^{86}Sr$ ratios higher than seawater. For example, radiogenic (0.70975–0.71279) $^{87}Sr/^{86}Sr$ ratios measured for authigenic carbonate cement contained in sedimentary rocks collected at the seafloor along a fault zone northwest of Pythia's Oasis are thought to reflect recrystallization of terrestrial clay minerals (Sample et al., 1993). Further, radiogenic (0.7120–0.7156) average $^{87}Sr/^{86}Sr$ ratios have been measured for the Columbia and Fraser rivers (Goldstein and Jacobsen, 1987; Wadleigh et al., 1985), which currently dominate sediment delivery to the Cascadia margin (Underwood, 2007).

Fluid interaction with basaltic rock (i.e., oceanic basement) and the dissolution and alteration of ash are commonly invoked to explain increased Sr concentrations and low (non-radiogenic) $^{87}Sr/^{86}Sr$ ratios of marine pore waters in Cascadia and elsewhere (Joseph et al., 2012; Ayres et al., 2020; Riedel et al., 2010; Torres et al., 2020). However, while both sources could explain the low $^{87}Sr/^{86}Sr$ ratios at Pythia's Oasis, neither can account for the extremely elevated dissolved Sr concentrations. Strontium concentrations of hydrothermal vent fluids at temperatures up to ~350 ˚C are commonly above seawater values, but do not exceed ~300 μM (Butterfield et al., 1990, Butterfield et al., 1994, Von Damm, 1990), about four times lower than the 1190 μM Pythia SO_4-depleted endmember. Thus, basaltic interaction with fluids, even at high temperatures, is discounted as the dominant source of excess Sr at Pythia's Oasis. If ash was

the dominant source of Sr, the $^{87}Sr/^{86}Sr$ of Pythia fluids would be significantly lower. This is illustrated by a simple mass balance calculation: summing the products of 1) seawater Sr concentration (87 μM) with seawater $^{87}Sr/^{86}Sr$ ratio (0.7092), and 2) the remaining approximately 1103 μM Sr assumed to come from ash with an ash $^{87}Sr/^{86}Sr$ ratio of ~0.7037 (Cascadia volcanics from the GEOROC database), gives a $^{87}Sr/^{86}Sr$ ratio of ~0.7041 for the 1190 μM-Sr fluids at Pythia's. Thus, an ash-dominant Sr source is also discounted and an additional Sr source is required to account for high Sr concentrations at Pythia's Oasis.

The recrystallization of biogenic carbonate towards dolomite releases Sr into the pore water, which can cause dissolved Sr concentrations to reach over 1000 μM (e.g., Ayres et al., 2020; Baker et al., 1982; Fantle and DePaolo, 2006; Kimura et al., 1997; Richter and DePaolo, 1987). Given that the $^{87}Sr/^{86}Sr$ ratio of seawater has not been below 0.7077 for at least 35 Ma (Paytan et al., 2021), this mechanism can account for the Pythia's dissolved Sr concentrations, but does not explain the $^{87}Sr/^{86}Sr$ ratio of 0.7066. Therefore, both carbonate recrystallization and either ash dissolution or fluid-basalt interaction are required to explain the Sr data at Pythia's Oasis.

Based on the Sr data alone, fluid-basalt interactions cannot be discounted as the cause for the non-radiogenic $^{87}Sr/^{86}Sr$ signal. However, ash dissolution is a more likely explanation because it does not require fluid transport from basalt into overlying sediments, which typically have permeabilities several orders of magnitude lower than the underlying basement (Spinelli et al., 2004). Elevated dissolved B concentrations at Pythia's (6660 μM), which greatly exceed those at basalt-hosted hydrothermal vent sites (<1000 μM; **Fig. 4.4**), also do not align with a basement source and $^{3}He/^{4}He$ ratios of 0.24–0.67 R_A in the venting fluids are inconsistent with a significant basaltic contribution. $^{3}He/^{4}He$ ratios at Pythia's are similar to values measured at

other seeps in Cascadia that have been interpreted to lack mantle He input (0.1–0.3 R_A; Baumberger et al., 2018; Collier and Lilley, 2005). In contrast, two samples collected at seeps southwest of the Coquille Bank in Cascadia (~42.7 ˚N; Baumberger et al., 2018), as well as seeps and scientific drilling sites at other subduction margins (e.g., Wiersberg et al., 2018; Füri et al., 2010) that have $^3He/^4He$ ratios above 1 R_A have been interpreted to contain mantle-derived helium (indicative of fluid-basalt interaction). Thus, fluid-basalt interaction (including with JDF crust or the accreted Siletzia large igneous province) is unlikely to significantly affect the fluids venting at Pythia's Oasis, and a combination of carbonate recrystallization and ash dissolution best explain the observed Sr data.

The Pythia Sr data implies a fluid source above basement, within or below a section of biogenic carbonate. However, modern inputs to the central CSZ are dominated by terrestrial fan deposits with low carbonate content (e.g., Underwood, 2007). It is therefore hypothesized that Pythia's fluids are traveling from a carbonate-rich underthrust section (**Fig. 4.6**) that pre-dates the onset of the Astoria Fan (~1.3–1.4 Ma; McNeil et al., 2000). This interpretation is consistent with results from Deep Sea Drilling Program Site 174 on the incoming JDF plate, ~100 km west of Pythia's (**Fig. 4.1)**. The two major stratigraphic units drilled at Site 174 were late Pleistocene to Pliocene in age, dominantly consisting of Astoria Fan sands (Unit 1) atop abyssal plain silts (Unit 2; Kulm & von Huene et al., 1973; **Fig. 4.6**). At this site, the deepest cores of Unit 2 (Core 39 at 705 mbsf, Core 40 at 766 mbsf, and within the drill bit pulled from 879 mbsf), recovered limestone beds containing up to 80% micritic carbonate ~160–30 m above the basement depth of 911 mbsf (Kulm & von Huene et al., 1973). The cores were interpreted as a section of pelagic sediment (inferred to be ~8 Ma) underlying the modern terrestrial deposits (von Huene & Kulm, 1973).

Beneath Pythia's, this pelagic section may comprise a more significant portion of the sediment section. A crustal age of ~9 Ma (Green & Harry, 1999; Han et al., 2018, Wilson, 2002) beneath Pythia's indicates that this portion of the plate likely subducted well before the onset of Astoria Fan sedimentation. Based on interpretations of multichannel seismic reflection images (Carbotte et al., 2024; Han et al., 2017), the décollement is relatively shallow offshore of central Oregon (~1.4–1.7 km above basement) such that this deep carbonate-rich section would be included in the subducting section, as opposed to accreted. Thus, the Sr data provide convincing evidence for fluid transport from the underthrust section, indicating a minimum source depth of ~4000 mbsf and minimum source temperature of ~170 ˚C (Carbotte et al., 2024; Philip et al., 2023; **Fig. 4.6**).

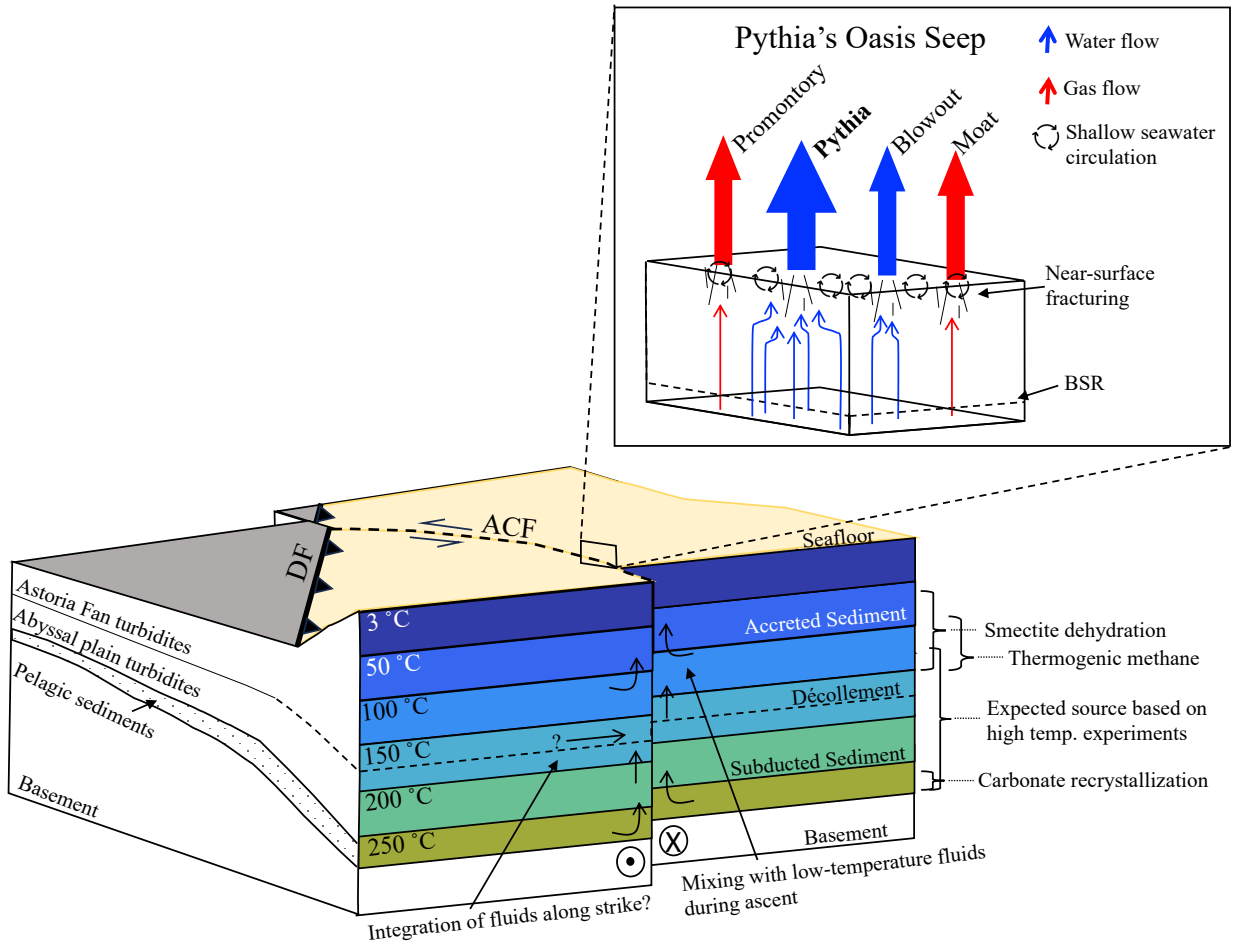

Figure 4.6. Conceptual diagram summarizing interpretations.

Water migrating from depth is funneled to a focused region near the seafloor. Gas and water discharge are partitioned; Pythia and Blow Out are dominated by water flow, whereas the Promontory and Moat sites are dominated by gas flow. The Alvin Canyon Fault (ACF) likely facilitates long-range fluid transport. Temperatures with depth from Philip et al., (2023). Incoming stratigraphic section based on DSDP Site 174 results (Kulm & von Huene et al, 1973; von Huene & Kulm, 1973).

A high-temperature fluid source is also supported by the molecular and isotopic composition of hydrocarbon gases in Pythia's Oasis vent and headspace samples. IGT samples and headspace samples from sediment cores below the sulfate-methane transition zone (SMTZ) contain methane (C_1), ethane (C_2), and propane (C_3), with no detectable higher hydrocarbons. $C_1/(C_2+C_3)$ ratios of ~130–7500, δ^{13}C-CH_4 values of -48 – -50‰, and δD-CH_4 values of -171– -178‰ in the measured samples are inconsistent with a purely microbial origin (e.g., Bernard et

al., 1977; Milkov & Etiope, 2018). The, elevated concentrations of ethane and propane along with relatively heavy methane isotopes indicate a mixture of microbial and thermogenic gas sources. Formation of thermogenic hydrocarbons occurs in the 80 – 150 ˚C range (e.g., Claypool & Kvenvolden, 1983; Kastner et al., 2014; Pape et al., 2014). Thus, a thermogenic gas component also requires upward migration of fluids from zones of elevated temperatures.

Comparison of Pythia vent fluids with the results of published high-temperature laboratory experiments further constrain formation temperatures required to produce the measured vent fluid compositions (**Table C3**). High-temperature experiments have been conducted on a range of sediment types to mimic the chemical changes associated with fluid-rock reactions in ridge-flank and subduction zone settings (You et al., 1996, James et al., 2003, Wei, 2007). Sediments tested include terrigenous turbidites and muds from the Escanaba Trough on the JDF plate (James et al., 2003), hemipelagic mudstone from the décollement zone in the Nankai Trough (You et al., 1996), and detrital smectite from the Barbados margin with and without a component of basaltic ash from the Lau Basin (Wei, 2007).

Elevated dissolved Li concentrations at Pythia's Oasis in this study and those reported by Philip et al., (2023) range from 202–275 μM, corresponding to temperatures between 125 and 250 ˚C (average ~180 ˚C) across the sedimentary results of the three experimental studies (**Table C3**). Similarly, Ca and Mg values at Pythia correspond to temperatures of 243˚C–298 ˚C, and 171˚C–250 ˚C, respectively. Despite the wide temperature range (up to 350 ˚C) tested in the three laboratory studies, several of the solutes measured (Sr, B, K) in these experiments never reached the concentrations measured at Pythia. Although B is mobilized at high temperatures in the experiments, B concentrations at Pythia (6660 μM) far exceed those achieved experimentally (~2000 μM), and those at hydrothermal vents (<1000 μM; **Fig. 4.4**). These differences are

largely due to the short-term nature of the experiments (days-months) and differing sediment compositions. Nevertheless, these experiments point to source temperatures ranging from 125 – 298 ˚C. Experiments conducted on the incoming material at Cascadia (James et al., 2003), which are likely the most representative, point to a source temperature range of ~200–250 ˚C (**Table C3**), consistent with input from the subducting section (**Fig. 4.6**).

The low Cl and K concentrations, slightly enriched $\delta^{18}O$, and depleted δD values (relative to seawater) of Pythia fluids indicate that a component of the fluids are sourced from smectite dehydration (Philip et al., 2023). The smectite to illite transition reaction reaches peak fluid production between 60–150 ˚C (e.g., Pytte and Reynolds, 1989; Kastner et al., 1991). Following Hensen et al., (2004), oxygen and hydrogen isotopic relationships were used to approximate the formation temperature of the outflowing freshened fluids (**Fig. C2**). The results indicate an estimated temperature of between 60 ˚C and 206 ˚C (**Fig. C2**, **Table C3**). The low $\delta^{18}O$ (0.3047 ‰) of the Cl-depleted endmember fluids indicates a low degree of fractionation between clay and surrounding pore water, consistent with high temperatures in the upper portion of this range. However, the temperature-dependent fractionation factor equations for δD from Yeh (1980) and Capuano (1992) used in this method are only validated for temperatures below 120 ˚C and 150 ˚C, respectively.

Additional established geothermometers utilize temperature-dependent relationships of fluid-rock Si, Mg, Li, Na, K and Ca contents. Si geothermometers are based on the solubility of quartz, chalcedony, cristobalite, and amorphous silica (e.g., Fournier, 1977; Fournier, 1981; Kharaka & Mariner, 1989). At Pythia's Oasis, the competition between quartz and clay formation, as well as retrograde reactions after fluid formation likely all impact Si concentrations such that one mineral phase is not controlling the dissolved silica concentration. K

geothermometers are similarly problematic given the strong influence of phyllosilicate formation on dissolved K concentrations. Thus, Si and K geothermometers are likely inappropriate and other major cations must be looked to as geothermometers.

Empirical geothermometers for sedimentary settings that utilize Li, Na, and Mg relationships were applied to estimate subsurface fluid formation temperatures (**Table C3**). The Li– Mg geothermometer from Kharaka & Mariner (1989), developed using a database of formation waters from oil and gas fields in North America, gives an estimated formation temperature of 74 ˚C. Na– Li geothermometers for saline fluids in sedimentary basins and geothermal systems give estimates of 135 ˚C (Fouillac & Michard, 1981) and 92 ˚C (Kharaka & Mariner 1989). A later revision of the Fouillac & Michard, (1981) geothermometer (Verma & Santoyo, 1997) results in an estimate of 132 ˚C.

The wide spread of temperature estimates from various geothermometers is not surprising. Major discrepancies can be caused by continued water-rock reactions during fluid migration, mixing between multiple fluid sources, disequilibrium between the fluid and host rock at depth, and application of geothermometers that are not representative of the system of interest. To demonstrate the potential inaccuracies of chemical geothermometers, the above Li, Na, and Mg empirical calculators were applied to data from two International Ocean Discovery Program (IODP) drilling sites where deep pore fluid samples were collected at moderate temperatures. Using Li, Na, and Mg pore fluid compositions from IODP Exp. 370 Site C0023 on the Muroto Transect (Heuer et al., 2017), empirical geothermometers overestimate in situ temperature at the top of the décollement (763 mbsf; ~86 ˚C) by ~10–55 ˚C. At the bottom of Hole U1546A (304 mbsf) drilled during IODP Exp. 385 in the Guaymas Basin (Teske et al., 2021), the same

geothermometers better predict the in situ temperature, but still encompass a large range of 62–109 ˚C where the measured temperature was ~67 ˚C.

In summary, many geochemical lines of evidence and several geothermometry techniques were used to constrain the source depth and formation temperature of the fluids expelled at Pythia's Oasis. The methods give a wide range of possible source temperatures from ~60–300 ˚C. The most consistent indicators (Sr signals, hydrocarbons, high-temperature laboratory experiments conducted on representative sediments) are the most reliable. They do not depend as heavily on major assumptions, including equilibrium between pore water and surrounding minerals at depth with minimal mixing or re-equilibration during ascent. Thus, the best estimate is a source depth within the underthrust section, ≥ 4 km below the seafloor, and fluid source temperatures of ~170–250 ˚C (**Fig. 4.6**).

4.6.3 *Volumetric discharge and implications for central CSZ hydrogeology and the water budget*

Using modeled fluid flow rates and SO_4-depleted endmember fluid compositions, the volumetric discharge and solute fluxes at Pythia's Oasis are estimated. A volumetric discharge of water from Pythia of 8.05 x 10^3 m^3/yr is estimated based on the flow rates modeled using particle tracking in this study, the range of flow rates presented in Philip et al., (2023), and a 5-cm orifice diameter (**Table 4.2**). Outside of Pythia, a volume flux of 60 m^3/yr is estimated based on modeled flow velocities from pore water Cl profiles and an approximate area of seepage of ~1700 m^2. The total volume flux estimated for the Pythia's seepage area is then ~8.11 x 10^3 m^3/yr (~8.27 x 10^6 kg/yr), where the Pythia vent constitutes the bulk of the discharge for the entire seepage area (**Table 4.2**).

Assuming that chloride behaves conservatively in this system, diluted dissolved Cl concentrations (341 mM) at Pythia relative to bottom water (548 mM) indicate that ~38% of the fluid outflowing at the Pythia vent is derived from mineral dehydration (**Table 4.2**). The deepest pore fluid samples for two sediment cores (BB2 near Blow Out and BB14 near Pythia) have even lower Cl concentrations than those of Pythia vent fluid, consistent with a larger dehydration-derived component (~47%). Thus, ~53 – 62% of the discharging fluid is sourced sediment compaction within the wedge and the underthrust sediments, not from dehydration (**Fig. 4.6)**. Because the composition of Pythia fluids is not substantially different from the composition of fluids below the zone of shallow seawater mixing in the cores, only a small fraction of this percentage is likely sourced from shallow seawater circulation (in the upper meter of the sediment column).

Table 4.2. Summary of modeled flow rates and estimated discharge at Pythia's Oasis.

	Estimates from Philip et al., (2023)		**Estimates from this study**		**Best estimate**
	Min	Max	Min	Max	
Pythia linear flow rate (cm/s)	10	30	2	21	13
Water discharge (m^3/yr)	6.18×10^3	1.86×10^4	1.23×10^3	1.30×10^4	8.05×10^3
Linear flow rate outside Pythia (cm/yr)	-	-	1.5	6	3.5
Appx. area of active seepage (m^2)	-	-	400	3000	1700
Appx. water discharge outside Pythia (m^3/yr)	-	-	6	180	60
Appx. total water discharge (m^3/yr)	**6.18×10^3**	**1.86×10^4**	**1.24×10^3**	**1.32×10^4**	**8.11×10^3**
% of total that is contributed by Pythia	-	-	99.5%	98.6%	99%
% of total that is contributed by flow outside Pythia	-	-	0.5%	1.4%	1%
% of fluid that is compaction-derived	62%	-	53% (BB2)	62% (IGT)	62%
Volume of fluid that is compaction-derived (m^3/yr)	4.00×10^3	1.10×10^4	6.59×10^2	8.20×10^3	5.04×10^3
% of total pore fluid input into central CSZ (per km trench length)	18%	50%	3%	37%	23%

Estimated compaction-derived fluid discharge at Pythia's Oasis ranges from 6.59×10^2 m^3/yr to $1.10\ 10^4$ m^3/yr, with an average of $5.04\ 10^3$ m^3/yr over the 4 years of observations (**Table 4.2**). This range corresponds to ~3% – 50% of the annual pore fluid input for the accreted and underthrust sections in central Cascadia per kilometer trench length (~2.2×10^4 m^3/yr; Philip et al., 2023; **Table 4.2**). This estimate indicates that a significant percentage of the subducting pore water at the central CSZ is accounted for by a single seep site. As indicated by other studies showing flow rates that are significantly higher than steady-state modeled values, the enhanced flow at Pythia's Oasis may reflect transient fluid release (e.g., Bekins & Screaton, 2007; Saffer & Bekins, 1999). Indeed, abundant evidence indicates that shear failure may temporarily increase fault permeability, permitting transient flow (e.g., Sibson 1990; Roeloffs, 1996; Solomon et al., 2009; Warren-Smith, 2019). At Pythia's Oasis, the rapid discharge directly observed since 2015, abundant seafloor seepage indicators, and shoaling of the regional BSR

consistent with sustained flow for ~1500 years (Philip et al., 2023) indicate long-lived discharge and that fluid flow persists at high rates beyond the earthquake recurrence interval (~500 years; Atwater & Hemphill-Haley, 1997; Goldfinger et al., 2012; Walton et al., 2021). Thus, high discharge at Pythia's Oasis is not solely due to transience.

While conventional models predict that pore fluids in the underthrust sediments are expelled relatively early in the subduction process (e.g., Moore & Vrolijk, 1992; Saffer & Tobin, 2011), sustained, high-volume discharge from the underthrust sediments at Pythia's Oasis (~20 km landward of the deformation front) implies that a significant amount of subducted water reaches the mid-slope region. A lack of drainage of underthrust sediments during initial subduction is consistent with inferred under-consolidation of the underthrust section in this region (Han et al., 2017) and could indicate that low permeability conditions characterize the central CSZ outer wedge. This scenario implies that elevated pore fluid pressures and therefore reduced effective stresses occur in the outer wedge, conceivably playing an important role in the reduced locking, increased seismicity, and other changing margin characteristics in this region. Alternatively, efficient drainage of underthrust sediment seaward of Pythia's Oasis may occur. For example, seeps on the ACF NW of Pythia's Oasis and/or seeps reported near the deformation front on the Wecoma fault (Tobin et al., 1993) could host efficient fluid flow from the underthrust section to the seafloor. In this scenario, rapid discharge at Pythia's Oasis may be sustained by significant horizontal transport of fluids along the megathrust and relatively permeable stratigraphic horizons into the ACF. This mechanism implies that the ACF is very permeable at depth underneath Pythia's relative to the megathrust and surrounding sediments and thus acts as a preferred drainage pathway. A combination of these scenarios offers a third explanation.

Overall, the hydrogeologic conditions that permit sustained, rapid fluid discharge at Pythia's Oasis (i.e., poor drainage beneath the outer wedge and/or a highly permeable and interconnected ACF funneling fluid from a large area along strike) may have broad impacts on the distribution and magnitude of pore fluid pressure, sediment consolidation, and effective stress across and along strike. Given that fault strength and stability are highly sensitive to pore fluid pressure and effective stress, high-volume discharge at this mid-slope seep may be indicative of permeability variations that play a major role in the changing margin characteristics and slip behavior that occur across the central Cascadia strike-slip faults. Further, enhanced drainage at the mid-slope region leads to expulsion of highly altered fluids that have experienced high-temperature reactions beyond those occurring nearer to the deformation front. Thus, focused, long-range fluid transport manifested at Pythia's Oasis are important for both geo-mechanical processes and geochemical cycles in the central CSZ.

4.6.4 *Solute fluxes and implications for geochemical cycling*

Given the high volume, highly altered composition, and elevated temperature of expelled fluid, the solute and heat fluxes associated with water discharge at Pythia's Oasis are comparable to those at both high- and low-temperature hydrothermal vent sites. For context, solute and heat fluxes at Pythia's are compared to three well-studied, high-flux hydrothermal systems: 1) Dorado Seamount; 2) Baby Bare Seamount; and 3) Inferno vent at Axial Seamount (**Table 4.3**). Dorado and Baby Bare are basaltic outcrops that serve as sites of focused low-temperature hydrothermal discharge, located on the eastern flank of the East Pacific Rise (Cocos Plate) and the eastern flank of the JDF Ridge (JDF plate), respectively. Fluid discharge at Baby Bare is ~2.8 x 10^8 kg/yr (Mottl et al., 1998). At Dorado, discharge is far greater at ~9.5 x 10^{10} kg/yr (Wheat & Fisher, 2008). Inferno is a high-temperature (>300 ˚C) black smoker chimney in the ASHES

hydrothermal vent field in the caldera of Axial Seamount on the JDF Ridge. Discharge of high-temperature, highly altered fluids from Inferno is ~3.56 x 10^7 kg/yr (calculated based on data from Rona and Trivett, 1992), which is lower than discharge at Dorado or Baby Bare, but ~1 order of magnitude greater than that at Pythia's.

Table 4.3. Pythia's Oasis solute fluxes compared with high and low temperature hydrothermal sites.

Pythia's Oasis solute fluxes estimated from compositions (Table 1) and total Pythia's Oasis water discharge (Q) calculated in this study (Table 3). Dorado Seamount (Cocos Plate) fluxes calculated from concentrations in Wheat et al. (2017) and volume and heat fluxes in Wheat & Fisher (2008). Baby Bare (JDF Ridge Flank) fluxes calculated from concentrations in Wheat et al. (2003) and volume and heat fluxes in Mottl et al. (1998). Inferno (ASHES Vent Field on Axial Seamount, JDF Ridge) fluxes calculated from concentrations in Butterfield et al. (1990) and volume and heat fluxes in Rona and Trivett (1992). Solute fluxes are calculated as $F = (C_{vent} - C_{SW}) \times Q$. Negative values indicate that the vent fluid concentration is lower than seawater. Heat flux at Pythia's is calculated as $H = Q \times \nu_p C_p \Delta T$, where ν_p is density of the vent fluid, C_p is specific heat capacity, and ΔT is the temperature difference between seawater and vent source temperature. Dashes indicate that measurements were below detection (Mn, Fe for Dorado and Baby Bare) or concentrations were negative after extrapolating to Mg = 0 (Alk for Inferno).

	C Seawater	C Pythia	Units (/kg)	F Pythia's Oasis (mol/yr)	F Dorado Seamount (mol/yr)	F Baby Bare Seamount (mol/yr)	F Inferno (ASHES field) (mol/yr)	% Dorado	% Baby Bare	% Inferno
Na	469	227.16	mmol	-2.0E+06	-3.8E+08	1.1E+06	1.1E+06	0.5%	-180%	-187%
Li	25.9	199.83	µmol	1.4E+03	-7.6E+04	-4.7E+03	2.2E+04	-2%	-31%	7%
K	10.2	0.69	mmol	-7.9E+04	-7.6E+06	-9.2E+05	5.9E+05	1%	9%	-13%
Mg	52.7	4.59	mmol	-4.0E+05	-4.7E+07	-1.4E+07	-1.9E+06	0.8%	3%	21%
Ca	10.27	51.16	mmol	3.4E+05	-8.5E+06	1.2E+07	1.3E+06	-4%	3%	26%
Sr	89	1174	µmol	9.0E+03	-9.5E+04	5.8E+03	3.7E+03	-9%	154%	245%
SO_4	28.2	0	mmol	-2.3E+05	-8.7E+07	-2.9E+06	-1.0E+06	0.3%	8%	23%
Alk	2.27	7.25	mmol	4.1E+04	1.9E+07	-5.1E+05	-	0.2%	-8%	-
Si	100	1031	µmol	7.7E+03	9.3E+06	7.2E+04	5.3E+05	0.1%	11%	1%
B	416	6572	µmol	5.1E+04	-1.1E+06	4.3E+04	6.2E+03	-4%	119%	823%
Mn	0.00036	8.16	µmol	6.7E+01	-	8.0E+02	4.1E+04	-	8%	0.2%
Fe	0.00054	393	µmol	3.2E+03	-	-	3.8E+04	-	-	9%
Volume Flux (kg/yr)				8.27E+06	9.46E+10	2.77E+08	3.56E+07			
Vent Fluid Temperature (˚C)				10.7 - 12.6	12.3	25	326			
Heat Flux (MW)				0.2	100-210	2-3	1.5	0.13%	8.0%	13%

The magnitudes of solute fluxes at Pythia's Oasis comprise a significant fraction of these hydrothermal fluxes despite the lower discharge volume (**Table 4.3**). In particular, the Sr and B fluxes at Pythia's exceed those at Baby Bare and Inferno despite a fluid discharge one to two orders of magnitude less. The volumetric discharge at Dorado is ~four orders of magnitude greater than Pythia's, yet B and Sr fluxes at Pythia's reach ~4% of Dorado. The Fe flux at Pythia's Oasis reaches almost 10% of the Fe flux at Inferno, possibly resulting from ash alteration and implying that reducing conditions or perhaps complexation with humic substances allows Fe to exit the vent without oxidizing. This is worth noting because extreme enrichment of Fe in high temperature hydrothermal vent fluids like those expelled at Inferno is recognized as a primary source of Fe to the ocean (e.g., German and Seyfried, 2013; Horner et al., 2015) but low temperature hydrothermal circulation is not a significant source of Fe to the ocean. Heat flux estimated at Pythia's, which is likely a minimum value because it doesn't account for the conductive component, reaches ~8% of the heat flux at Baby Bare and ~13% of the flux at Inferno.

Although no other warm seeps with similar solute fluxes to Pythia's Oasis have been reported in Cascadia, abundant seepage occurs along the ACF and other strike-slip faults offshore of central Oregon (Tobin et al., 1993; Carson et al., 1994; Goldfinger et al., 1997; Sample et al., 1993) indicating that Pythia's Oasis may not be unique. During this study's 2019 expedition, four seeps were detected NW of Pythia's and 27 emission sites SE of Pythia's along the ACF projection based on multibeam acoustic plume identification. An ROV seafloor survey of an area of abundant bubble plumes ~16 km SE of Pythia's confirmed seafloor seepage indicators (bacterial mats, carbonates, bivalves, and tubeworm colonies). On the lower continental slope, linear patterns of authigenic carbonates parallel to the fault trace have been

interpreted as the product of venting of methane-rich pore fluids (Carson et al., 1994, Goldfinger et al., 1997). Venting of deeply-sourced (>2 km depth) fluids has also been observed along the Wecoma fault, ~40 km north of the ACF (Sample et al., 1993; Tobin et al., 1993). Perhaps most notably, a warm seep was recently discovered offshore of southern Oregon that could accommodate similar fluxes to Pythia's Oasis (Beeson et al., 2022). However, without thorough geochemical investigation of these sites, their discharge and solute fluxes remain unknown.

If these or other seeps do host similar solute fluxes to Pythia's Oasis, conventional modest estimates of the impact of subduction zone seeps on marine geochemical cycles could be severely unrepresentative. If, for example, 10 seeps similar to Pythia's Oasis existed along the three strike-slip faults (or perhaps hosted by forearc thrust faults), B fluxes from the combined seep discharge would dwarf those from Baby Bare and Inferno (12 times greater and 80 times greater, respectively), and reach half the magnitude of the Dorado B flux. Sr fluxes would be over 15 times greater those at Baby Bare and Inferno and would match Dorado. Additionally, heat fluxes from the combined discharge would match those at Baby Bare and Inferno.

In summary, significant heat fluxes and fluxes of Li, Ca, Si, Mn, and Fe occur at Pythia's Oasis, and B and Sr fluxes rival those at high-temperature hydrothermal vents and low-temperature ridge-flank hydrothermal sites (**Table 4.3**). Estimated fluxes at Pythia's Oasis, and the intriguing possibility that similar high-volume seeps may exist in Cascadia, support the hypothesis that the transfer of seep fluids to the ocean may influence regional elemental cycling. If Pythia's Oasis is representative of a fraction of the mid-slope seepage globally, solute fluxes at subduction zone seeps could be more important for global marine geochemical cycles than previously considered. Further, advective heat transfer at high-flux seeps could perturb temperature estimates at the plate boundary by a substantial amount at Cascadia and elsewhere

(e.g., Harris et al., 2017; Spinelli & Wang, 2008). Continued investigation of Pythia's and detailed characterization of other Cascadia seeps and fault-hosted seeps at other subduction zones are necessary to further explore these possibilities. However, given that much of the water flow at Pythia's Oasis is focused to a single orifice (Pythia), assessing the fluid discharge and geochemical fluxes for this seep is likely simpler than at seafloor seeps where water flow is more broadly distributed. Thus, additional sampling and surveying techniques, and denser arrays of sediment core sampling and heat flow determinations may be required to fully characterize fluxes and the importance of other seeps.

4.7 CONCLUSION

This study presents a detailed examination of the Pythia's Oasis seep area, including ROV and AUV survey data, heat flow determinations, and geochemistry of sediment pore waters and discrete vent fluid samples. The results constitute an in-depth characterization of a dynamic, complex seep where fluids transported from plate boundary depths along the Alvin Canyon strike-slip fault are rapidly expelled at the seafloor, ~20 km landward of the deformation front at the central Cascadia subduction zone.

Rapid expulsion (~2-30 cm s^{-1}) of 11.8 ˚C–12.6 ˚C highly altered fluid occurs at the Pythia primary emission site. Expelled fluids are significantly enriched in Ca, Sr, B, Li, Mn, Si, and Fe, and depleted in K, Mg, Na, and Cl relative to seawater. Elevated $\delta^{18}O$ and $\delta^{13}C$ DIC, depleted $\delta^{37}Cl$, δD, and $^{87}Sr/^{86}Sr$, crustal $^{3}He/^{4}He$ ($R_a \leq 0.67$), and the presence of ethane and propane also characterize the venting fluids. These geochemical signatures indicate a component of the fluid is sourced from within the subducting sediment section below the megathrust (≥4 km below seafloor) at temperatures of ~170–250 ˚C. Anomalously high heat flow values (up to 260 mW m^{-2}) measured near Pythia and the near-by emission site Blow Out are consistent with

focused outflow of warm water. Elevated heat flow, rapid fluid flow rates, and highly altered fluid compositions at the Pythia and Blow Out sites are consistent with focused, long-range upward fluid advection.

Long-lived, rapid fluid discharge may be driven by inefficient drainage of subducting sediments nearer the deformation front and/or funneling of fluid horizontally over a large area and vertically into the permeable fault plane, and thus could have broad scale geo-mechanical impacts in central Cascadia. Long-distance transfer of fluids along the ACF in the mid-slope region of the Cascadia margin results in significant solute fluxes into the ocean (particularly B and Sr) at Pythia's Oasis. If similar solute fluxes occur at other mid-slope seeps globally, subduction zone seeps may play an important role in the cycles of many elements and isotope ratios in the ocean.

4.8 ACKNOWLEDGMENTS

This work is supported by NSF award OCE-1902446. We thank the science party, captain, and crew of the *R/V Atlantis*, the ROV *Jason* and AUV *Sentry* teams, and the Oregon State University coring facility (MARSSAM) onboard during the 2019 expedition for making this work possible. Special thanks to Marv Lilley for conducting analyses of $\delta^{13}C$ and δD of methane, Pierre Agrinier for providing $\delta^{37}Cl$ data, and Brent Lary for providing $^{3}He/^{4}He$ data. Thank you to Mitch Elend for constructing the photomosaic.

Chapter 5. CONCLUSIONS

5.1 Key Findings and Final Thoughts

Much of the populated world lies on or near a subduction zone where one tectonic plate dives beneath another along a megathrust fault. Given that subduction zone faults generate earthquakes and tsunamis, even incremental improvements in understanding the mechanisms of their behavior are of critical societal importance. This dissertation provides a geochemical investigation of seep sites and diffuse flow locations at the Hikurangi and Cascadia subduction zones to assess the links between hydrogeologic, geochemical, and geo-mechanical processes.

In the studies presented, fault-hosted seep sites were located using hydroacoustic surveys, heat flow measurements, and ROV visual seafloor surveys at extant seep locations. This multifaceted approach allowed for the discovery of new seep sites and detailed investigation of previously discovered seeps. Seep fluids were then sampled via sediment coring with subsequent pore water extraction, Isobaric Gas Tight and Major samplers (Seewald et al., 2001; von Damm et al., 1985), and benthic fluid flow meters (Solomon et al., 2008; Tryon et al., 2001). Diffuse flow locations were also surveyed and sampled using many of the same techniques. Fluid compositions were then determined, and fluid sources were inferred. Modeling of fluid compositions with depth (sediment cores) or tracer concentrations over time (fluid flow meters), were used for quantification of fluid flow rates. By assessing fluid sources and fluid flow rates at seeps and diffuse sites, the results presented here inform on permeability and fluid migration pathways, the state and evolution of pore fluid pressures, the influence of forearc seepage on geochemical cycling, the impact of slip on margin dewatering, and overall outer forearc water budgets at the Hikurangi and Cascadia margins.

Chapters 2 targeted seep sites spanning the continental slope at the northern and southern Hikurangi margin, offshore of the North Island of New Zealand, with focus on seepage associated with deep-reaching thrust faults. Key findings are that: 1) fluid compositions of recovered pore water samples do not exhibit major alteration from seawater, indicating they are sourced shallowly, from sediment compaction within the wedge; 2) low flow rates estimated from pore water data indicate fault zones are relatively impermeable, particularly deep within the wedge; and 3) comparison of offshore seep data from this study with onshore seep results from previous studies show clear geochemical changes across strike, supporting previous evidence for a shift in stress regime and a variable state of overpressure. Collectively, these results suggest that drainage of the plate boundary and surrounding sediments is inefficient in the region of slow slip. Thus, the accumulation of pore pressure due to low permeability faults at depth in the offshore portion of the forearc may act as a control on slow slip activity.

Chapter 2 is novel because it sampled all major known seeps associated with thrust faults from the shelf break to the deformation front at the northern and southern Hikurangi subduction zone; the number and spatial coverage of sediment cores retrieved for this study is remarkable. Despite the multifaced approach used to locate and sample seep sites, no evidence of thermal or geochemical signatures indicative of long-distance fluid transport from plate boundary depths to the seafloor was observed. This result was somewhat unexpected and contrasts with observations at several other subduction zones, highlighting the absolute need for direct measurements to identify the intricacies and deviations from model projections of fault-hosted fluid flow at individual subduction zones.

Chapter 3 temporally expands the findings of Chapter 2 using continuous records of fluid flow rate from 10 seafloor flow meters before, during, and after a large slow slip event. This

effort tested the fault-valve model at the northern Hikurangi margin and contributes to an improved understanding of offshore locking and shallow slow slip behavior. Key findings are that: 1) net flow polarity varies across strike, consistent with creep on the shallow megathrust and locking in the slow slip source area in the inter-slow slip period; 2) flow rate transients at diffuse flow locations temporally correlate with the slow slip event and are compatible with signals of local volumetric strain; and 3) flow transients at seeps may indicate shallow permeability changes but do not provide convincing evidence of wide-spread fault-valving and transport of deeply-sourced fluids to the seafloor during the monitored period.

This novel work fills a crucial data gap by providing the first direct measurements of seafloor fluid flow rates throughout a slow slip cycle at the Hikurangi margin. The long-term records of diffuse flow serve as highly sensitive indicators of secular strain, providing constraints on offshore interplate coupling that is not well resolved by onshore instrumentation and is essential for the assessment of seismic and tsunami hazards. The timing of seafloor flow rate transients reveal that offshore strain occurs during and prior to the majority of strain recorded at onshore GNSS sites. The occurrence of downward flow transients during the slow slip event near the deformation front is surprising, and may have broad implications for how slow slip propagates near the trench. Finally, while flow transients at two seep sites are indicative of a shallow permeability response to the 2019 slow slip event, wide-spread long-range fluid transport is not observed despite geophysical indication of fault-valving at northern Hikurangi. Hence, these direct, long-term, offshore measurements test model projections and provide an invaluable contribution to onshore and indirect observations.

Chapter 4 focuses on a seep site offshore of central Oregon called Pythia's Oasis, which rapidly expels highly altered fluids. This study presents an in-depth characterization of this

dynamic, complex seep where fluids transported from plate boundary depths along the Alvin Canyon strike-slip fault are rapidly expelled at the seafloor, ~20 km landward of deformation front at the central Cascadia subduction zone. Key findings are that: 1) heat flow, modeled fluid flow rates, and pore water solute profiles vary within the seep area, consistent with focused, long-range upward fluid advection at the Pythia and Blow Out sites vs. gas emission and shallow seawater circulation dominating at the Promontory and Moat sites; 2) fluid compositions suggest a component of the seep fluid is sourced from the subducting sediment at temperatures of 170-250 ˚C; 3) sustained, rapid fluid discharge at Pythia's Oasis may imply elevated pore pressures occur beneath the outer wedge, and/or that the Alvin Canyon Fault is highly permeable beneath Pythia's Oasis, funneling fluid from a large area vertically and along strike; 4) solute fluxes associated with water discharge at Pythia's Oasis are comparable to the solute fluxes at both high- and low-temperature hydrothermal discharge sites.

The high-resolution bathymetric mapping, numerous visual (ROV) surveys, dense array of sediment core samples and heat flow determinations, and full suite of geochemical analyses performed on venting and pore fluids for this study comprise a remarkably detailed characterization of the Pythia's Oasis seep. The results of this study suggest that focused, long-range fluid transport manifested at Pythia's Oasis may be important for both geo-mechanical processes and geochemical cycles in the central CSZ . Given that fault strength and stability are highly sensitive to pore fluid pressure and effective stress, high-volume discharge at this mid-slope seep may be indicative of permeability variations that play a major role in the changing margin characteristics and slip behavior that occur across the central Cascadia strike-slip faults. Further, if Pythia's Oasis is representative of a fraction of the mid-slope seepage globally, solute fluxes at subduction zone seeps could be more important for global marine geochemical cycles

that previously considered. Perhaps these powerful, wide-reaching implications will promote further detailed investigation of mid-slope seeps at Cascadia and elsewhere in future studies.

This dissertation used visual, geophysical, and chiefly geochemical methods to investigate seafloor seeps and diffuse flow sites at the northern and southern Hikurangi and central Cascadia subduction zones. The investigative techniques employed here were quite comprehensive, yet future work re-visiting these locations would certainly provide new insights into the interrelationships between hydrogeologic and mechanical process given that the many processes governing the expression of seafloor fluid flow are variable across even small spatial and temporal scales. In-depth studies of focused and diffuse fluid transport in the outer forearc of other subduction zones globally also deserves continued attention to address remaining questions and explore those yet to be identified. Overall, by directly sampling subduction zone fluids and assessing in situ hydrogeologic conditions at the Hikurangi and Cascadia margins, this dissertation advances our understanding of the interrelationship between mechanical and hydrogeologic processes in subduction zones, and thus affords insight into numerous broad scale processes of scientific and societal relevance.

BIBLIOGRAPHY

Aller, R. C. (1982). The Effects of Macrobenthos on Chemical Properties of Marine Sediment and Overlying Water. In Animal-sediment relations: the biogenic alteration of sediments (pp. 53–102). Springer US. https://doi.org/10.1007/978-1-4757-1317-6_2

Antriasian, A., Harris, R. N., Tréhu, A. M., Henrys, S. A., Phrampus, B. J., Lauer, R., Gorman, A. R., Pecher, I. A., & Barker, D. (2019). Thermal regime of the Northern Hikurangi margin, New Zealand. Geophysical Journal International, 216(2), 1177–1190. https://doi.org/10.1093/gji/ggy450

Arnulf, A. F., Biemiller, J., Lavier, L., Wallace, L. M., Bassett, D., Henrys, S., Pecher, I., Crutchley, G., & Faverola, A. P. (2021). Physical conditions and frictional properties in the source region of a slow-slip event. Nature Geoscience, 14, 334–340. https://doi.org/10.1038/s41561-021-00741-0

Atwater, B. F., & Hemphill-Haley, E. (1997). Recurrence Intervals for Great Earthquakes of the Past 3,500 Years at Northeastern Willapa Bay, Washington. United States Geological Survey Professional Paper, P 1576, 108 pp.

Atwater, B. F., Nelson, A. R., Clague, J. J., Carver, G. A., Yamaguchi, D. K., Bobrowsky, P. T., Bourgois, J., Darienzo, M. E., Grant, W. C., Hemphill-Haley, E., Kelsey, H. M., Jacoby, G. C., Nishenko, S. P., Palmer, S. P., Peterson, C. D., & Reinhart, M. A. (1995). Summary of coastal geologic evidence for past great earthquakes at the Cascadia subduction zone. Earthquake Spectra, 11(1), 1–18. https://doi.org/10.1193/1.1585800

Aylward, I., Solomon, E. A., Philip, B. T., Torres, M. E., Harris, R. N., Collier, R. W., & Kelley, D. S. (2023). Marine sediment porosity and pore water chemistry from Pythia's Oasis Seep on the continental margin offshore Oregon, USA. Interdisciplinary Earth Data Alliance (IEDA). https://doi.org/10.26022/IEDA/112771

Aylward, I., Solomon, E. A., Torres, M. E., & Harris, R. N. (2024). Geochemical and Thermal Constraints on the Hikurangi Subduction Zone Hydrogeologic System and its Role in Slow Slip. Geochemistry Geophysics Geosystems, [in press].

Aylward, I., Solomon, E. A., Torres, M. E., Harris, R. N., & Whorley, T. L. (2024). Marine sediment porosity and pore water chemistry from the Hikurangi margin, offshore the North Island of New Zealand. Interdisciplinary Earth Data Alliance (IEDA). https://doi.org/10.60520/IEDA/113176

Aylward, I., Solomon, E. A., Whorley, T. L., Miller, R., Hillman, J. I. T., Seabrook, S., Palmer, N., & Wallace, L. M. (2023). The evolution of fluid flow throughout the slow slip cycle: testing the hydrologic response to SSEs at the Hikurangi subduction zone. AGU Fall Meeting.

Ayres, C., Torres, M. E., Haley, B., & Luo, M. (2020). Data report: 87Sr/86Sr in pore fluids from IODP Expeditions 372 and 375, Hikurangi margin. 372(March), 1–5. https://doi.org/10.14379/iodp.proc.372b375.202.2020

Baetsle, L. H. (1969). Migration of radionuclides in porous media. In A. M. F. Duhamel (Ed.), Progress in Nuclear Energy XII, Health Physics (pp. 707–730). Pelargonium Press.

Baker, P. A., Gieskes, J. M., & Elderfield, H. (1982). Diagenesis of carbonates in deep-sea sediments - evidence from Sr/Ca ratios and interstitial dissolved Sr2+ data. Journal of Sedimentary Petrology, 52(1), 0071–0082.

Bangs, N. L. B., Hornbach, M. J., & Berndt, C. (2011). The mechanics of intermittent methane venting at South Hydrate Ridge inferred from 4D seismic surveying. Earth and Planetary Science Letters, 310(1–2), 105–112. https://doi.org/10.1016/j.epsl.2011.06.022

Bangs, N. L. B., Moore, G. F., Gulick, S. P. S., Pangborn, E. M., Tobin, H. J., Kuramoto, S., & Taira, A. (2009). Broad, weak regions of the Nankai Megathrust and implications for shallow coseismic slip. Earth and Planetary Science Letters, 284(1–2), 44–49. https://doi.org/10.1016/j.epsl.2009.04.026

Bangs, N. L. B., Morgan, J. K., Bell, R. E., Han, S., Arai, R., Kodaira, S., Gase, A. C., Wu, X., Davy, R., Frahm, L., Tilley, H. L., Barker, D. H. N., Edwards, J. H., Tobin, H. J., Reston, T. J., Henrys, S. A., Moore, G. F., Bassett, D., Kellett, R., … Fry, B. (2023). Slow slip along the Hikurangi margin linked to fluid-rich sediments trailing subducting seamounts. Nature Geoscience, 16(6), 505–512. https://doi.org/10.1038/s41561-023-01186-3

Barker, D. H. N., Henrys, S., Caratori Tontini, F., Barnes, P. M., Bassett, D., Todd, E., & Wallace, L. (2018). Geophysical constraints on the relationship between seamount subduction, slow slip, and tremor at the north Hikurangi subduction zone, New Zealand. Geophysical Research Letters, 45(23), 12,804-12,813. https://doi.org/10.1029/2018GL080259

Barnes, J. D., Cullen, J., Barker, S., Agostini, S., Penniston-Dorland, S., Lassiter, J. C., Klügel, A., & Wallace, L. (2019). The role of the upper plate in controlling fluid-mobile element (Cl, Li, B) cycling through subduction zones: Hikurangi forearc, New Zealand. Geosphere, 15(3), 642–658. https://doi.org/10.1130/GES02057.1

Barnes, P. M., Wallace, L. M., Saffer, D. M., Bell, R. E., Underwood, M. B., Fagereng, A., Meneghini, F., Savage, H. M., Rabinowitz, H. S., Morgan, J. K., Kitajima, H., Kutterolf, S., Hashimoto, Y., Engelmann De Oliveira, C. H., Noda, A., Crundwell, M. P., Shepherd, C. L., Woodhouse, A. D., Harris, R. N., … LeVay, L. J. (2020). Slow slip source characterized by lithological and geometric heterogeneity. Science Advances, 6(13). https://doi.org/10.1126/sciadv.aay3314

Bartlow, N., Wallace, L. M., Elliott, J., & Schwartz, S. (2021). Slipping and Locking in Earth's Earthquake Factories. Eos, 102. https://doi.org/10.1029/2021eo155885

Bassett, D., Sutherland, R., & Henrys, S. (2014). Slow wavespeeds and fluid overpressure in a region of shallow geodetic locking and slow slip, Hikurangi subduction margin, New Zealand. Earth and Planetary Science Letters, 389, 1–13. https://doi.org/10.1016/j.epsl.2013.12.021

Baumberger, T., Embley, R. W., Merle, S. G., Lilley, M. D., Raineault, N. A., & Lupton, J. E. (2018). Mantle-Derived Helium and Multiple Methane Sources in Gas Bubbles of Cold Seeps Along the Cascadia Continental Margin. Geochemistry, Geophysics, Geosystems, 19(11), 4476–4486. https://doi.org/10.1029/2018GC007859

Beeson, J., Baumberger, T., Merle, S. G., Antriasian, A., Butterfield, D. A., Buck, N. J., Lu, G.-S., & Roe, K. K. (2022). OSB42B-1198 Initial Results from E/V Nautilus Expedition NA128 “Cascadia Margin Seep Exploration”: Cascadia Margin Mapping, High-Resolution ROV Multibeam, and Gas/Fluid Sampling. AGU Fall Meeting.

Behl, R. J., & Garrison, R. E. (1994). The origin of chert in the Monterey Formation of California. 29th International Geological Congress, 29, 101–132.

Bekins, B. A., & Screaton, E. J. (2007). Convergent Margin Structure , Fluids , and Subduction Thrust Evolution. In T. H. Dixon & J. C. Moore (Eds.), The Seismogenic Zone of Subduction Thrust Faults. Columbia University Press. https://www.jstor.org/stable/10.7312/dixo13866.9%0AJSTOR

Bell, R., Sutherland, R., Barker, D. H. N., Henrys, S., Bannister, S., Wallace, L., & Beavan, J. (2010). Seismic reflection character of the Hikurangi subduction interface, New Zealand, in the region of repeated Gisborne slow slip events. Geophysical Journal International, 180(1), 34–48. https://doi.org/10.1111/j.1365-246X.2009.04401.x

Berg, R. D. (2018). Quantifying the deep: The importance of diagenetic reactions to marine geochemical cycles [Doctoral Dissertation, University of Washington]. http://hdl.handle.net/1773/43434

Bernard, B., Brooks, J. M., & Sackett, W. M. (1977). A geochemical model for characterization of hydrocarbon gas sources in marine sediments. Proceedings of the Annual Offshore Technology Conference, 1977-May(December), 435–438. https://doi.org/10.4043/2934-ms

Berner, R. A. (1964). An idealized model of dissolved sulfate distribution in recent sediments. Geochimica et Cosmochimica Acta, 28(9), 1497–1503. https://doi.org/10.1016/0016-7037(64)90164-4

Berner, R. A. (1980). Early diagenesis: A Theoretical Approach (H. D. Holland, Ed.). Princeton University Press.

Bilek, S. L., & Lay, T. (2002). Tsunami earthquakes possibly widespread manifestations of frictional conditional stability. Geophysical Research Letters, 29(14), 1–4. https://doi.org/10.1029/2002GL015215

Bland, K. J., Uruski, C. I., & Isaac, M. J. (2015). Pegasus Basin, eastern New Zealand: A stratigraphic record of subsidence and subduction, ancient and modern. New Zealand Journal of Geology and Geophysics, 58(4), 319–343. https://doi.org/10.1080/00288306.2015.1076862

Boetius, A., Ravenschlag, K., Schubert, C. J., Rickert, D., Widdel, F., Gleseke, A., Amann, R., Jørgensen, B. B., Witte, U., & Pfannkuche, O. (2000). A marine microbial consortium apparently mediating anaerobic oxidation methane. Nature, 407(6804), 623–626. https://doi.org/10.1038/35036572

Boudreau, B. P. (1997). Diagenetic models and their implementation: modelling transport and reactions in aquatic sediments. Springer-Verlag.

Brantley, S. L., Evans, B., Hickman, S. H., & Crerar, D. A. (1990). Healing of microcracks in quartz: Implications for fluid flow. Geology, 18(2), 136–139. https://doi.org/10.1130/0091-7613(1990)018<0136:HOMIQI>2.3.CO;2

Brown, K. M., Saffer, D. M., & Bekins, B. A. (2001). Smectite diagenesis, pore-water freshening, and fuid flow at the toe of the Nankai wedge. Earth and Planetary Science Letters, 194(1–2), 97–109.

Brown, K. M., Tryon, M. D., DeShon, H. R., Dorman, L. R. M., & Schwartz, S. Y. (2005). Correlated transient fluid pulsing and seismic tremor in the Costa Rica subduction zone. Earth and Planetary Science Letters, 238(1–2), 189–203. https://doi.org/10.1016/j.epsl.2005.06.055

Burdige, D. J. (1993). The biogeochemistry of manganese and iron reduction in marine sediments. Earth Science Reviews, 35(3), 249–284. https://doi.org/10.1016/0012-8252(93)90040-E

Burdige, D. J. (2006). Geochemistry of Marine Sediments. Princeton University Press.

Butterfield, D. A., & Massoth, G. J. (1994). Geochemistry of north Cleft segment vent fluids: temporal changes in chlorinity and their possible relation to recent volcanism. Journal of Geophysical Research, 99(B3), 4951–4968. https://doi.org/10.1029/93JB02798

Butterfield, D. A., Massoth, G. J., McDuff, R. E., Lupton, J. E., & Lilley, M. D. (1990). Geochemistry of Hydrothermal Fluids From Axial Seamount Hydrothermal Emissions Study Vent Field, Juan de Fuca Ridge: Subseafloor Boiling and Subsequent Fluid-Rock Interaction. 95(90).

Butterfield, D. A., McDuff, R. E., Mottl, M. J., Lilley, M. D., Lupton, J. E., & Massoth, G. J. (1994). Gradients in the composition of hydrothermal fluids from the Endeavour segment vent field: phase separation and brine loss. Journal of Geophysical Research, 99(B5), 9561–9583. https://doi.org/10.1029/93JB03132

Capuano, R. M. (1992). The temperature dependence of hydrogen isotope fractionation between clay minerals and water: Evidence from a geopressured system. Geochimica et Cosmochimica Acta, 56(6), 2547–2554. https://doi.org/10.1016/0016-7037(92)90208-Z

Carbotte, S. M., Boston, B., Han, S., Shuck, B., Beeson, J., Canales, J. P., Tobin, H., Miller, N., Nedimovic, M., Tréhu, A., Lee, M., Lucas, M., Jian, H., Jiang, D., Moser, L., Anderson, C., Judd, D., Fernandez, J., Campbell, C., … Gahlawat, R. (2024). Subducting plate structure

and megathrust morphology from deep seismic imaging linked to earthquake rupture segmentation at Cascadia. Science Advances, 10(23), 1–19. https://doi.org/10.1126/sciadv.adl3198

Carslaw, H. S., & Jaeger, J. C. (1959). Conduction of Heat in Solids (Second Ed.). Oxford University Press.

Carson, B., & Screaton, E. J. (1998). FLUID FLOW IN ACCRETIONARY PRISMS: EVIDENCE FOR FOCUSED, TIME-VARIABLE DISCHARGE. Reviews of Geophysics, 36(3), 329–351.

Carson, B., Seke, E., Paskevich, V., & Holmes, M. L. (1994). Fluid expulsion sites on the Cascadia accretionary prism: mapping diagenetic deposits with processed GLORIA imagery. Journal of Geophysical Research, 99(B6). https://doi.org/10.1029/94jb00120

Carson, B., Westbrook, G. K., Musgrave, R. J., Ashi, J., Baranov, B., Brown, K. M., Camerlenghi, A., Caulet, J.-P., Chamov, N., Clennell, M. B., Cragg, B. A., Dietrich, P., Foucher, J.-P., Housen, B., Hovland, M., Jarrad, R. D., Kastner, M., Kopf, A., Mackay, M. E., … Zellers, S. D. (1992). Proceedings of the Ocean Drilling Program, 146 Part 1 Scientific Results. https://doi.org/10.2973/odp.proc.sr.146-1.1995

Chesley, C., Naif, S., Key, K., & Bassett, D. (2021). Fluid-rich subducting topography generates anomalous forearc porosity. Nature, 595, 255–260. https://doi.org/10.1038/s41586-021-03619-8

Claypool, G. E., & Kaplan, I. R. (1974). The origin and distribution of methane in marine sediments. In I. R. Kaplan (Ed.), Natural gases in marine sediments (pp. 99–139). Plenum Press.

Claypool, G. E., & Kvenvolden, K. A. (1983). Methane and other hydrocarbon gases in marine sediment. Annual Review of Earth & Planetary Sciences, 11, 299–327.

Collier, R. W., & Lilley, M. D. (2005). Composition of shelf methane seeps on the Cascadia Continental Margin. Geophysical Research Letters, 32(6), 1–4. https://doi.org/10.1029/2004GL022050

Condit, C. B., Guevara, V. E., Delph, J. R., & French, M. E. (2020). Slab dehydration in warm subduction zones at depths of episodic slip and tremor. Earth and Planetary Science Letters, 552, 116601. https://doi.org/10.1016/j.epsl.2020.116601

Cook, A. E., Paganoni, M., Clennell, M. B., McNamara, D. D., Nole, M., Wang, X., Han, S., Bell, R. E., Solomon, E. A., Saffer, D. M., Barnes, P. M., Pecher, I. A., Wallace, L. M., LeVay, L. J., & Petronotis, K. E. (2020). Physical Properties and Gas Hydrate at a Near-Seafloor Thrust Fault, Hikurangi Margin, New Zealand. Geophysical Research Letters, 47(16), 1–11. https://doi.org/10.1029/2020GL088474

Crundwell, M. P., & Woodhouse, A. (2022). Biostratigraphically constrained chronologies for Quaternary sequences from the Hikurangi margin of north-eastern Zealandia. New Zealand

Journal of Geology and Geophysics, 1–21. https://doi.org/10.1080/00288306.2022.2101481

Darrah, T. H., Vengosh, A., Jackson, R. B., Warner, N. R., & Poreda, R. J. (2014). Noble gases identify the mechanisms of fugitive gas contamination in drinking-water wells overlying the Marcellus and Barnett Shales. Proceedings of the National Academy of Sciences of the United States of America, 111(39), 14076–14081. https://doi.org/10.1073/pnas.1322107111

Davis, D., Suppe, J., & Dahlen, F. A. (1983). Mechanics of Fold-and-Thrust Belts and Accretionary Wedges. Journal of Geophysical Research: Solid Earth, 89(B2), 1153–1172. https://doi.org/10.1029/JB089iB12p10087

Davis, E. E., Becker, K., Wang, K., & Kinoshita, M. (2009). Co-seismic and post-seismic pore-fluid pressure changes in the Philippine Sea plate and Nankai decollement in response to a seismogenic strain event off Kii Peninsula, Japan. Earth, Planets and Space, 61(6), 649–657. https://doi.org/10.1186/BF03353174

Davis, E. E., Heesemann, M., & Wang, K. (2011). Evidence for episodic aseismic slip across the subduction seismogenic zone off Costa Rica: CORK borehole pressure observations at the subduction prism toe. Earth and Planetary Science Letters, 306(3–4), 299–305. https://doi.org/10.1016/j.epsl.2011.04.017

Davis, E. E., Sun, T., Heesemann, M., Becker, K., & Schlesinger, A. (2023). Long-Term Offshore Borehole Fluid-Pressure Monitoring at the Northern Cascadia Subduction Zone and Inferences Regarding the State of Megathrust Locking. Geochemistry, Geophysics, Geosystems, 24(6), 1–25. https://doi.org/10.1029/2023GC010910

Davis, E. E., Villinger, H., & Sun, T. (2015). Slow and delayed deformation and uplift of the outermost subduction prism following ETS and seismogenic slip events beneath Nicoya Peninsula, Costa Rica. Earth and Planetary Science Letters, 410, 117–127. https://doi.org/10.1016/j.epsl.2014.11.015

Dragert, H., Wang, K., & James, T. S. (2001). A silent slip event on the deeper Cascadia subduction interface. Science, 292(5521), 1525–1528. https://doi.org/10.1126/science.1060152

Dutilleul, J., Bourlange, S., Géraud, Y., & Stemmelen, D. (2020). Porosity, pore structure, and fluid distribution in the sediments entering the northern Hikurangi margin, New Zealand. Journal of Geophysical Research: Solid Earth, 125(11), 1–21. https://doi.org/10.1029/2020JB020330

Eberhart-Phillips, D., & Bannister, S. (2015). 3-D imaging of the northern Hikurangi subduction zone, New Zealand: Variations in subducted sediment, slab fluids and slow slip. Geophysical Journal International, 201(2), 838–855. https://doi.org/10.1093/gji/ggv057

Elderfield, H., Wheat, C. G., Mottl, M. J., Monnin, C., & Spiro, B. (1999). Fluid and geochemical transport through oceanic crust: A transect across the eastern flank of the Juan

de Fuca Ridge. Earth and Planetary Science Letters, 172(1–2), 151–165. https://doi.org/10.1016/S0012-821X(99)00191-0

Ellis, S., Fagereng, Å., Barker, D., Henrys, S., Saffer, D., Wallace, L., Williams, C., & Harris, R. (2015). Fluid budgets along the northern Hikurangi subduction margin, New Zealand: The effect of a subducting seamount on fluid pressure. Geophysical Journal International, 202(1), 277–297. https://doi.org/10.1093/gji/ggv127

Eslinger, E. V., & Yeh, H. W. (1981). Mineralogy, O18/ O16 and D/H ratios of clay-rich sediments from Deep Sea Drilling Project Site 180, Aleutian Trench. Clays & Clay Minerals, 29(4), 309–315. https://doi.org/10.1346/ccmn.1981.0290409

Fagereng, Å., Diener, J. F. A., Ellis, S., & Remitti, F. (2018). Fluid-related deformation processes at the up- and downdip limits of the subduction thrust seismogenic zone: What do the rocks tell us? Special Paper of the Geological Society of America, 534(12), 187–215. https://doi.org/10.1130/2018.2534(12)

Fantle, M. S., Barnes, B. D., & Lau, K. V. (2020). The Role of Diagenesis in Shaping the Geochemistry of the Marine Carbonate Record. Annual Review of Earth and Planetary Sciences, 48, 549–583. https://doi.org/10.1146/annurev-earth-073019-060021

Fantle, M. S., & DePaolo, D. J. (2006). Sr isotopes and pore fluid chemistry in carbonate sediment of the Ontong Java Plateau: Calcite recrystallization rates and evidence for a rapid rise in seawater Mg over the last 10 million years. Geochimica et Cosmochimica Acta, 70(15), 3883–3904. https://doi.org/10.1016/j.gca.2006.06.009

Fisher, A. T., Davis, E. E., Firth, J. V, Andersson, E. M., Aoike, K., Becker, K., Brown, K. A., Buatier, M. D., Constantin, M., Elderfield, H., Gonçalves, C. A., Grigel, J. S., Hunter, A. G., Inoue, A., Lawrence, R. M., Macdonald, R. D., Marescotti, P., Martin, J. T., Monnin, C., … Firth, J. V. (2000). Hydrothermal Circulation in the Oceanic Crust: Eastern Flank of the Juan De Fuca Ridge. In A. T. Fisher, E. E. Davis, & C. Escutia (Eds.), Proceedings of the Ocean Drilling Program, 168 Scientific Results. https://doi.org/10.2973/odp.proc.sr.168.2000

Fisher, A. T., Urabe, T., & Klaus, A. (2004). The hydrogeologic architecture of basaltic oceanic crust : compartmentalization , anisotropy , microbiology , and crustal-scale properties on the eastern flank of Juan de Fuca Ridge. In Integrated Ocean Drilling Program Scientific Prospectus, 301. https://doi.org/10.2204/iodp.pr.301.2004

Fouillac, C., & Michard, G. (1981). Sodium/lithium ratio in water applied to geothermometry of geothermal reservoirs. Geothermics, 10(1), 55–70. https://doi.org/10.1016/0375-6505(81)90025-0

Fournier, R. O. (1977). Chemical geothermometers and mixing models for geothermal systems. Geothermics, 5(1–4), 41–50. https://doi.org/10.1016/0375-6505(77)90007-4

Fournier, R. O. (1981). Application of water geochemistry to geothermal exploration and reservoir engineering. In L. Rybach & L. J. P. Muffler (Eds.), Geothermal Systems: Principles and Case Histories (pp. 109–143). John Wiley.

Froelich, P. N., Klinkhammer, G. P., Bender, M. L., Luedtke, N. A., Heath, G. R., Cullen, D., Dauphin, P., Hammond, D., Hartman, B., & Maynard, V. (1979). Early oxidation of organic matter in pelagic sediments of the eastern equatorial Atlantic: suboxic diagenesis. Geochimica et Cosmochimica Acta, 43(7), 1075–1090. https://doi.org/10.1016/0016-7037(79)90095-4

Füri, E., Hilton, D. R., Tryon, M. D., Brown, K. M., McMurtry, G. M., Brückmann, W., & Wheat, C. G. (2010). Carbon release from submarine seeps at the Costa Rica fore arc: Implications for the volatile cycle at the Central America convergent margin. Geochemistry, Geophysics, Geosystems, 11(4). https://doi.org/10.1029/2009GC002810

Gamage, K., & Screaton, E. (2006). Characterization of excess pore pressures at the toe of the Nankai accretionary complex, Ocean Drilling Program sites 1173, 1174, and 808: Results of one-dimensional modeling. Journal of Geophysical Research: Solid Earth, 111(B4), 1–13. https://doi.org/10.1029/2004JB003572

Gase, A. C., Bangs, N. L., Saffer, D. M., Han, S., Miller, P. K., Bell, R. E., Arai, R., Henrys, S. A., Kodaira, S., Davy, R., Frahm, L., & Barker, D. H. N. (2023). Subducting volcaniclastic-rich upper crust supplies fluids for shallow megathrust and slow slip. Science Advances, 9(33), eadh0150. https://doi.org/10.1126/sciadv.adh0150

German, C. R., & Seyfried, W. E. (2013). Hydrothermal Processes. In Treatise on Geochemistry: Second Edition (2nd ed., Vol. 8). Elsevier Ltd. https://doi.org/10.1016/B978-0-08-095975-7.00607-0

Gieskes, J., Gamo, T., & Brumsack, H. (1991). Chemical Methods for Interstitial Water Analysis aboard JOIDES Resolution. Ocean Drilling Program Technical Note 15, 1–60. https://doi.org/10.2973/odp.tn.15.1991

Goldfinger, C., Kulm, L. D., Yeats, R. S., McNeill, L., & Hummon, C. (1997). Oblique strike-slip faulting of the central Cascadia submarine forearc. Journal of Geophysical Research: Solid Earth, 102(B4), 8217–8243. https://doi.org/10.1029/96jb02655

Goldfinger, C., Kulm, L. V. D., Yeats, R. S., Mitchell, Cl., Weldon II, R., Peterson, C., Darienzo, M. E., Grant, W. C., & Priest, G. R. (1992). Neotectonic map of the oregon continental margin and adjacent abyssal plain: Vol. Open-File.

Goldfinger, C., Nelson, C. H., Morey, A. E., Johnson, J. E., Patton, J. R., Karabanov, E., Gutierrez-Paston, J., Eriksson, A. T., Gracia, E., Dunhill, G., Enkin, R. J., Dallimore, A., & Vallier, T. (2012). Turbidite Event History — Methods and Implications for Holocene Paleoseismicity of the Cascadia Subduction Zone.

Goldstein, S. J., & Jacobsen, S. B. (1987). The Nd and Sr isotopic systematics of river-water dissolved material: Implications for the sources of Nd and Sr in seawater. Chemical Geology, 66(3–4), 245–272.

Green, N. L., & Harry, D. L. (1999). On the relationship between subducted slab age and arc basalt petrogenesis, Cascadia subduction system, North America. Earth and Planetary Science Letters, 171(3), 367–381. https://doi.org/10.1016/S0012-821X(99)00159-4

Haeckel, M., Boudreau, B. P., & Wallmann, K. (2007). Bubble-induced porewater mixing: A 3-D model for deep porewater irrigation. Geochimica et Cosmochimica Acta, 71(21), 5135–5154. https://doi.org/10.1016/j.gca.2007.08.011

Hamilton, E. L. (1979). Vp/Vs and Poisson's ratios in marine sediments and rocks. October, 66(4), 1093–1101.

Han, M. W., & Suess, E. (1989). Subduction-induced pore fluid venting and the formation of authigenic carbonates along the cascadia continental margin: Implications for the global Ca-cycle. Palaeogeography, Palaeoclimatology, Palaeoecology, 71(1–2), 97–118. https://doi.org/10.1016/0031-0182(89)90032-1

Han, S., Bangs, N. L., Carbotte, S. M., Saffer, D. M., & Gibson, J. C. (2017). Links between sediment consolidation and Cascadia megathrust slip behaviour. Nature Geoscience, 10(12), 954–959. https://doi.org/10.1038/s41561-017-0007-2

Han, S., Bangs, N. L., Gase, A., Bell, R. E., Arai, R., Kodaira, S., Barker, D. H. N., Henrys, S. A., Tobin, H. J., Moore, G. F., Davy, R., & Frahm, L. (2022). Low Permeability Faults Inhibit Fluid Expulsion from the Northern Hikurangi Subduction Margin.

Han, S., Carbotte, S. M., Canales, J. P., Nedimović, M. R., & Carton, H. (2018). Along-Trench Structural Variations of the Subducting Juan de Fuca Plate From Multichannel Seismic Reflection Imaging. Journal of Geophysical Research: Solid Earth, 123(4), 3122–3146. https://doi.org/10.1002/2017JB015059

Harris, R. N., Torres, M. E., & Solomon, E. A. (2023). Heat flow data from the Hikurangi subduction zone, 2019 (RR1901, RR1902). Marine Geoscience Data System (MGDS). https://doi.org/10.26022/IEDA/331405

Hedges, J. I., & Keil, R. G. (1995). Sedimentary organic matter preservation: an assessment and speculative synthesis. Marine Chemistry, 49(2–3), 81–115. https://doi.org/10.1016/0304-4203(95)00011-F

Heise, W., Caldwell, T. G., Bannister, S., Bertrand, E. A., Ogawa, Y., Bennie, S. L., & Ichihara, H. (2017). Mapping subduction interface coupling using magnetotellurics: Hikurangi margin, New Zealand. Geophysical Research Letters, 44(18), 9261–9266. https://doi.org/10.1002/2017GL074641

Henry, P., Pichon, X. Le, Lallemant, S., Lance, S., Martin, J. B., Foucher, J.-P., Fiala-Médioni, A., Rostek, F., Guilhaumou, N., Pranal, V., & Castrec, M. (1996). Fluid flow in and around

a mud volcano field seaward of the Barbados accretionary wedge: Results from Manon cruise. Journal of Geophysical Research, 101(B9), 20297–20323.

Hensen, C., Scholz, F., Nuzzo, M., Valadares, V., Gràcia, E., Terrinha, P., Liebetrau, V., Kaul, N., Silva, S., Martínez-Loriente, S., Bartolome, R., Piñero, E., Magalhães, V. H., Schmidt, M., Weise, S. M., Cunha, M., Hilario, A., Perea, H., Rovelli, L., & Lackschewitz, K. (2015). Strike-slip faults mediate the rise of crustal-derived fluids and mud volcanism in the deep sea. Geology, 43(4), 339–342. https://doi.org/10.1130/G36359.1

Hensen, C., Wallmann, K., Schmidt, M., Ranero, C. R., & Suess, E. (2004). Fluid expulsion related to mud extrusion off Costa Rica - A window to the subducting slab. Geology, 32(3), 201–204. https://doi.org/10.1130/G20119.1

Hensen, C., Zabel, M., Pfeifer, K., Schwenk, T., Kasten, S., Riedinger, N., Schulz, H. D., & Boetius, A. (2003). Control of sulfate pore-water profiles by sedimentary events and the significance of anaerobic oxidation of methane for the burial of sulfur in marine sediments. Geochimica et Cosmochimica Acta, 67(14), 2631–2647. https://doi.org/10.1016/S0016-7037(03)00199-6

Hesse, R., & Harrison, W. E. (1981). Gas hydrates (clathrates) causing pore-water freshening and oxygen isotope fractionation in deep-water sedimentary sections of terrigenous continental margins. Earth and Planetary Science Letters, 55(3), 453–462. https://doi.org/10.1016/0012-821X(81)90172-2

Hesslein, R. H. (1976). An in situ sampler for close interval pore water studies. Limnology and Oceanography, 21(6), 912–914. https://doi.org/10.4319/lo.1976.21.6.0912

Heuer, V. B., Inagaki, F., Morono, Y., Kubo, Y., Maeda, L., Bowden, S., Cramm, M., Henkel, S., Hirose, T., Homola, K., Hoshino, T., Ijiri, A., Imachi, H., Kamiya, N., Kaneko, M., Lagostina, L., Manners, H., McClelland, H.-L., Metcalfe, K., … Yang, K. (2017). Site C0023. Proceedings of the International Ocean Discovery Program Volume 370. https://doi.org/10.14379/iodp.proc.370.103.2017

Hickman, S., Sibson, R., & Bruhn, R. (1995). Introduction to Special Section: Mechanical Involvement of Fluids in Faulting. Journal of Geophysical Research: Solid Earth, 100(B7), 12831–12840. https://doi.org/10.1029/95jb01121

Hirose, H., Hirahara, K., Kimata, F., Fujii, N., & Miyazaki, S. (1999). A slow thrust slip event following the two 1996 Hyuganada earthquakes beneath the Bungo Channel, southwest Japan. Geophysical Research Letters, 26(21), 3237–3240. https://doi.org/10.1029/1999GL010999

Hong, W. L., Sauer, S., Panieri, G., Ambrose, W. G., James, R. H., Plaza-Faverola, A., & Schneider, A. (2016). Removal of methane through hydrological, microbial, and geochemical processes in the shallow sediments of pockmarks along eastern Vestnesa Ridge (Svalbard). Limnology and Oceanography, 61(S1), S324–S343. https://doi.org/10.1002/lno.10299

Hong, W. L., Solomon, E. A., & Torres, M. E. (2014). A kinetic-model approach to quantify the effect of mass transport deposits on pore water profiles in the Krishna-Godavari Basin, Bay of Bengal. Marine and Petroleum Geology, 58(Part A), 223–232. https://doi.org/10.1016/j.marpetgeo.2014.06.014

Horner, T. J., Williams, H. M., Hein, J. R., Saito, M. A., Burton, K. W., Halliday, A. N., & Nielsen, S. G. (2015). Persistence of deeply sourced iron in the Pacific Ocean. Proceedings of the National Academy of Sciences of the United States of America, 112(5), 1292–1297. https://doi.org/10.1073/pnas.1420188112

Hubbert, M. K., & Rubey, W. W. (1959). Role of Fluid Pressure in Mechanics of Overthrust Faulting. In Geological Society of America Bulletin (Vol. 70, Issue 2). https://doi.org/10.1130/0016-7606(1959)70[115:rofpim]2.0.co;2

Hutnak, M., Fisher, A. T., Harris, R., Stein, C., Wang, K., Spinelli, G., Schindler, M., Villinger, H., & Silver, E. (2008). Large heat and fluid fluxes driven through mid-plate outcrops on ocean crust. Nature Geoscience, 1(9), 611–614. https://doi.org/10.1038/ngeo264

Hyndman, R. D., & Wang, K. (1995). The rupture zone of Cascadia great earthquakes from current deformation and the thermal regime. Journal of Geophysical Research, 100(B11), 22,133-22,154.

Iversen, N., & Jorgensen, B. B. (1985). Anaerobic methane oxidation rates at the sulfate-methane transition in marine sediments from Kattegat and Skagerrak (Denmark). Limnology and Oceanography, 30(5), 944–955. https://doi.org/10.4319/lo.1985.30.5.0944

James, R. H., Allen, D. E., & Seyfried, J. E. (2003). An experimental study of alteration of oceanic crust and terrigenous sediments at moderate temperatures (51 to 350°C): Insights as to chemical processes in near-shore ridge-flank hydrothermal systems. Geochimica et Cosmochimica Acta, 67(4), 681–691. https://doi.org/10.1016/S0016-7037(02)01113-4

Jannasch, H. W., Wheat, C. G., Plant, J. N., Kastner, M., & Stakes, D. S. (2004). Continuous chemical monitoring with osmotically pumped water samplers: OsmoSampler design and applications. Limnology and Oceanography: Methods, 2(4), 102–113. https://doi.org/10.4319/lom.2004.2.102

Joseph, C., Torres, M. E., Martin, R. A., Haley, B. A., Pohlman, J. W., Riedel, M., & Rose, K. (2012). Using the 87Sr/86Sr of modern and paleoseep carbonates from northern Cascadia to link modern fluid flow to the past. Chemical Geology, 334, 122–130. https://doi.org/10.1016/j.chemgeo.2012.10.020

Kang, M., Christian, S., Celia, M. A., Mauzerall, D. L., Bill, M., Miller, A. R., Chen, Y., Conrad, M. E., Darrah, T. H., & Jackson, R. B. (2016). Identification and characterization of high methane-emitting abandoned oil and gas wells. Proceedings of the National Academy of Sciences of the United States of America, 113(48), 13636–13641. https://doi.org/10.1073/pnas.1605913113

Kastner, M., Elderfield, H., & Martin, J. B. (1991). Fluids in convergent margins: what do we know about their composition, origin, role in diagenesis and importance for oceanic chemical fluxes? Philosophical Transactions of the Royal Society B, 243–259.

Kastner, M., Keene, J. B., & Gieskes, J. M. (1977). Diagenesis of siliceous oozes-I. Chemical controls on the rate of opal-A to opal-CT transformation-an experimental study. Geochimica et Cosmochimica Acta, 41(8). https://doi.org/10.1016/0016-7037(77)90099-0

Kastner, M., Sample, J. C., Whiticar, M. J., Hovland, M., Cragg, B. A., & Parkes, J. R. (1995). Geochemical Evidence for Fluid Flow and Diagenesis at the Cascadia Convergent Margin. Proceedings of the Ocean Drilling Program, 146 Part 1 Scientific Results, 146(1994). https://doi.org/10.2973/odp.proc.sr.146-1.243.1995

Kastner, M., Solomon, E. A., Harris, R. N., & Torres, M. E. (2014). Fluid origins, thermal regimes, and fluid and solute fluxes in the forearc of subduction zones. In Developments in Marine Geology (Volume 7, pp. 671–733). Elsevier. https://doi.org/10.1016/B978-0-444-62617-2.00022-0

Kharaka, Y. K., & Mariner, R. H. (1989). Chemical Geothermometers and Their Application to Formation Waters from Sedimentary Basins. In N. D. Naeser & T. H. McCulloh (Eds.), Thermal History of Sedimentary Basins (pp. 99–117). Springer-Verlag. https://doi.org/10.1007/978-1-4612-3492-0_6

Kimura, G., Silver, E. A., & Blum, P. (1997). Site 1039. Proceedings of the Ocean Drilling Program, 170 Initial Reports, January. https://doi.org/10.2973/odp.proc.ir.170.103.1997

Kitajima, H., & Saffer, D. M. (2012). Elevated pore pressure and anomalously low stress in regions of low frequency earthquakes along the Nankai Trough subduction megathrust. Geophysical Research Letters, 39(23), 1–5. https://doi.org/10.1029/2012GL053793

Kluesner, J. W., Silver, E. A., Bangs, N. L., McIntosh, K. D., Gibson, J., Orange, D., Ranero, C. R., & Von Huene, R. (2013). High density of structurally controlled, shallow to deep water fluid seep indicators imaged offshore Costa Rica. Geochemistry, Geophysics, Geosystems, 14(3), 519–539. https://doi.org/10.1002/ggge.20058

Kodaira, S., Iidaka, T., Kato, A., Park, J. O., Iwasaki, T., & Kaneda, Y. (2004). High pore fluid pressure may cause silent slip in the Nankai Trough. Science, 304(5675), 1295–1298. https://doi.org/10.1126/science.1096535

Kulm, L. D., Suess, E., Moore, J. C., Carson, B., Lewis, B. T., Ritger, S. D., Kadko, D. C., Thornburg, T. M., Embley, R. W., Rugh, W. D., Massoth, G. J., Langseth, M. G., Cochrane, G. R., & Scamman, R. L. (1986). Oregon subduction zone: Venting, fauna, and carbonates. Science, 231(4738), 561–566. https://doi.org/10.1126/science.231.4738.561

Kulm, L. D., & von Huene, R. (1973). Site 174. Initial Reports of the Deep Sea Drilling Project, 18, 1. https://doi.org/10.2973/dsdp.proc.18.105.1973

Kümpel, H. -J. (1991). Poroelasticity: parameters reviewed. Geophysical Journal International, 105(3), 783–799. https://doi.org/10.1111/j.1365-246X.1991.tb00813.x

LaBonte, A. L., Brown, K. M., & Fialko, Y. (2009). Hydrologic detection and finite element modeling of a slow slip event in the Costa Rica prism toe. Journal of Geophysical Research: Solid Earth, 114(4), 1–13. https://doi.org/10.1029/2008JB005806

Lauer, R. M., & Saffer, D. M. (2012). Fluid budgets of subduction zone forearcs: The contribution of splay faults. Geophysical Research Letters, 39(13), 1–6. https://doi.org/10.1029/2012GL052182

L'Esperance, J. C., Boudreau, B. P., Barry, M. A., & Johnson, B. D. (2013). Small-scale, high-precision and high-accuracy determination of Poisson's ratios in cohesive marine sediments. Geo-Marine Letters, 33(1), 75–81. https://doi.org/10.1007/s00367-012-0305-z

Levin, L. A. (2005). Ecology of cold seep sediments: Interactions of fauna with flow, chemistry and microbes. Oceanography and Marine Biology, 43, 1–46.

Li, Y.-H., & Gregory, S. (1974). Diffusion of ions in sea water and in deep-sea sediments. Geochimica et Cosmochimica Acta, 38(5), 703–714. https://doi.org/10.1073/pnas.1619553114

Liu, X., & Flemings, P. B. (2006). Passing gas through the hydrate stability zone at southern Hydrate Ridge, offshore Oregon. Earth and Planetary Science Letters, 241(1–2), 211–226. https://doi.org/10.1016/j.epsl.2005.10.026

Liu, Y., & Rice, J. R. (2007). Spontaneous and triggered aseismic deformation transients in a subduction fault model. Journal of Geophysical Research: Solid Earth, 112(9), 1–23. https://doi.org/10.1029/2007JB004930

Luo, M., Hong, W. L., Torres, M. E., Kutterolf, S., Pank, K., Hopkins, J. L., Solomon, E. A., Wang, K. L., & Lee, H. Y. (2023). Volcanogenic aluminosilicate alteration drives formation of authigenic phases at the northern Hikurangi margin: Implications for subseafloor geochemical cycles. Chemical Geology, 619, 121317. https://doi.org/10.1016/j.chemgeo.2023.121317

Luo, M., Yu, M., Torres, M. E., Solomon, E. A., Gieskes, J., You, C. F., Kong, L., & Chen, D. (2024). Volcanic ash alteration triggers active sedimentary lithium cycling: Insights from lithium isotopic compositions of pore fluids and sediments in the Hikurangi subduction zone. Earth and Planetary Science Letters, 642, 118854. https://doi.org/10.1016/j.epsl.2024.118854

MacKay, M. E., Moore, G. F., Cochrane, G. R., Moore, J. C., & Kulm, L. V. D. (1992). Landward vergence and oblique structural trends in the Oregon margin accretionary prism: Implications and effect on fluid flow. Earth and Planetary Science Letters, 109(3–4), 477–491. https://doi.org/10.1016/0012-821X(92)90108-8

Martin, J. B., Kastner, M., Henry, P., Le Pichon, X., & Lallement, S. (1996). Chemical and isotopic evidence for sources of fluids in a mud volcano field seaward of the Barbados accretionary wedge. Journal of Geophysical Research: Solid Earth, 101(B9), 20325–20345. https://doi.org/10.1029/96jb00140

McCaffrey, R., Wallace, L. M., & Beavan, J. (2008). Slow slip and frictional transition at low temperature at the Hikurangi subduction zone. Nature Geoscience, 1(5), 316–320. https://doi.org/10.1038/ngeo178

McKinney, R. E., & Conway, R. A. (1957). Chemical Oxygen in Biological Waste Treatment. Sewage and Industrial Wastes, 29(10), 1097–1106. https://www.jstor.org/stable/25033446%0AJSTOR

McNamara, D. D., Behboudi, E., Wallace, L., Saffer, D., Cook, A. E., Fagereng, A., Paganoni, M., Wu, H. Y., Kim, G., Lee, H., Savage, H. M., Barnes, P., Pecher, I., LeVay, L. J., & Petronotis, K. E. (2021). Variable in situ stress orientations across the northern Hikurangi subduction margin. Geophysical Research Letters, 48(5), 1–11. https://doi.org/10.1029/2020GL091707

McNeill, L. C., Goldfinger, C., Kulm, L. V.D., & Yeats, R. S. (2000). Tectonics of the Neogene Cascadia forearc basin: Investigations of a deformed late Miocene unconformity. Bulletin of the Geological Society of America, 112(8), 1209–1224. https://doi.org/10.1130/0016-7606(2000)112<1209:TOTNCF>2.0.CO;2

Merle, S. G., Embley, R. W., Johnson, H. P., Lau, T. K., Phrampus, B. J., Raineault, N. A., & Gee, L. J. (2021). Distribution of Methane Plumes on Cascadia Margin and Implications for the Landward Limit of Methane Hydrate Stability. Frontiers in Earth Science, 9(March), 1–24. https://doi.org/10.3389/feart.2021.531714

Milkov, A. V., & Etiope, G. (2018). Revised genetic diagrams for natural gases based on a global dataset of >20,000 samples. Organic Geochemistry, 125, 109–120. https://doi.org/10.1016/j.orggeochem.2018.09.002

Moore, J. C., Brown, K. M., Horath, F., Cochrane, G., Mackay, M., & Moore, G. (1991). Plumbing accretionary prisms: effects of permeability variations. Philosophical Transactions of the Royal Society of London. Series A: Physical and Engineering Sciences, 335(1638), 275–288. https://doi.org/10.1098/rsta.1991.0047

Moore, J. C., & Saffer, D. (2001). Updip limit of the seismogenic zone beneath the accretionary prism of Southwest Japan: An effect of diagenetic to low-grade metamorphic processes and increasing effective stress. Geology, 29(2), 183–186. https://doi.org/10.1130/0091-7613(2001)029<0183:ULOTSZ>2.0.CO;2

Moore, J. C., & Vrolijk, Peter. (1992). Fluids in accretionary prisms. Reviews of Geophysics, 30(2), 113–135. https://doi.org/10.1029/90EO00031

Morgan, J. K., Solomon, E. A., Fagereng, A., Savage, H. M., Wang, M., Meneghini, F., Barnes, P. M., Bell, R. E., French, E., Bangs, N. L., Kitajima, H., Saffer, D. M., & Wallace, L. M.

(2022). Seafloor overthrusting causes ductile fault deformation and fault sealing along the Northern Hikurangi Margin. Earth and Planetary Science Letters, 593, 117651. https://doi.org/10.1016/j.epsl.2022.117651

Mottl, M. J., Wheat, C. G., Fryer, P., Gharib, J., & Martin, J. B. (2004). Chemistry of springs across the Mariana forearc shows progressive devolatilization of the subducting plate. Geochimica et Cosmochimica Acta, 68(23), 4915–4933. https://doi.org/10.1016/j.gca.2004.05.037

Mottl, M. J., Wheat, G., Baker, E., Becker, N., Davis, E., Feely, R., Grehan, A., Kadko, D., Lilley, M., Massoth, G., Moyer, C., & Sansone, F. (1998). Warm springs discovered on 3.5 Ma oceanic crust, eastern flank of the Juan de Fuca Ridge. Geology, 26(1), 51–54. https://doi.org/10.1130/0091-7613(1998)026<0051:WSDOMO>2.3.CO;2

Nayar, K. G., Sharqawy, M. H., Banchik, L. D., & Lienhard V, J. H. (2016). Thermophysical properties of seawater: A review and new correlations that include pressure dependence. Desalination, 390, 1–24. https://doi.org/10.1016/j.desal.2016.02.024

Neuzil, C. E. (1995). Abnormal Pressures as Hydrodynamic Phenomena. American Journal of Science, 295(6), 742–786.

Neuzil, C. E. (2003). Hydromechanical coupling in geologic processes. Hydrogeology Journal, 11(1), 41–83. https://doi.org/10.1007/s10040-002-0230-8

Pape, T., Geprägs, P., Hammerschmidt, S., Wintersteller, P., Wei, J., Fleischmann, Ti., Bohrmann, G., & Kopf, A. J. (2014). Hydrocarbon seepage and its sources at mud volcanoes of the Kumano forearc basin, Nankai Trough subduction zone. Geochemistry, Geophysics, Geosystems, 15(6), 2180–2194. https://doi.org/10.1002/2013GC005057.Received

Park, J. O., Fujie, G., Wijerathne, L., Hori, T., Kodaira, S., Fukao, Y., Moore, G. F., Bangs, N. L., Kuramoto, S., & Taira, A. (2010). A low-velocity zone with weak reflectivity along the Nankai subduction zone. Geology, 38(3), 283–286. https://doi.org/10.1130/G30205.1

Park, J. O., Tsuru, T., Kodaira, S., Cummins, P. R., & Kaneda, Y. (2002). Splay fault branching along the Nankai subduction zone. Science, 297(5584), 1157–1160. https://doi.org/10.1126/science.1074111

Paytan, A., Griffith, E. M., Eisenhauer, A., Hain, M. P., Wallmann, K., & Ridgwell, A. (2021). A 35-million-year record of seawater stable Sr isotopes reveals a fluctuating global carbon cycle. Science, 371(6536), 1346–1350. https://doi.org/10.1126/science.aaz9266

Peacock, S. M. (2004). Insight into the hydrogeology and alteration of oceanic lithosphere based on subduction zones and arc volcanism. In E. E. Davis & H. Elderfield (Eds.), Hydrogeology of Oceanic Lithosphere (pp. 659–676). Cambridge University Press.

Peng, Z., & Gomberg, J. (2010). An integrated perspective of the continuum between earthquakes and slow-slip phenomena. Nature Geoscience, 3(9), 599–607. https://doi.org/10.1038/ngeo940

Philip, B. T., Solomon, E. A., Kelley, D. S., Tréhu, A. M., Whorley, T. L., Roland, E., Tominaga, M., & Collier, R. W. (2023). Fluid sources and overpressures within the central Cascadia Subduction Zone revealed by a warm, high-flux seafloor seep. Science Advances, 9(4). https://doi.org/10.1126/sciadv.add6688

Pytte, A. M., & Reynolds, R. C. (1989). The Thermal Transformation of Smectite to Illite. In N. D. Naeser & T. H. McCulloh (Eds.), Thermal History of Sedimentary Basins (pp. 133–140). Springer, New York, NY. https://doi.org/https://doi.org/10.1007/978-1-4612-3492-0_8

Ranero, C. R., Grevemeyer, I., Sahling, H., Barckhausen, U., Hensen, C., Wallmann, K., Weinrebe, W., Vannucchi, P., Von Huene, R., & McIntosh, K. (2008). Hydrogeological system of erosional convergent margins and its influence on tectonics and interplate seismogenesis. Geochemistry, Geophysics, Geosystems, 9(3). https://doi.org/10.1029/2007GC001679

Reeburgh, W. S. (1967). An Improved Interstitial Water Sampler. Limnology and Oceanography, 12(1), 163–165. https://doi.org/10.4319/lo.1967.12.1.0163

Reyes, A. G., Christenson, B. W., & Faure, K. (2010). Sources of solutes and heat in low-enthalpy mineral waters and their relation to tectonic setting, New Zealand. Journal of Volcanology and Geothermal Research, 192(3–4), 117–141. https://doi.org/10.1016/j.jvolgeores.2010.02.015

Rice, J. R., & Cleary, M. P. (1976). Some Basic Stress Diffusion Solutions for Fluid-Saturated Elastic Porous Media With Compressible Constituents. Reviews of Geophysics and Space Physics, 14(2), 227–241.

Richter, F. M., & DePaolo, D. J. (1987). Numerical models for diagenesis and the Neogene Sr isotopic evolution of seawater from DSDP Site 590B. Earth and Planetary Science Letters, 83(1–4), 27–38. https://doi.org/10.1016/0012-821X(87)90048-3

Riedel, M., Collett, T. S., & Malone, M. (2010). Expedition 311 Synthesis: scientific findings. Proceedings of the IODP, 311. https://doi.org/10.2204/iodp.proc.311.213.2010

Riedel, M., Scherwath, M., Römer, M., Veloso, M., Heesemann, M., & Spence, G. D. (2018). Distributed natural gas venting offshore along the Cascadia margin. Nature Communications, 9(1). https://doi.org/10.1038/s41467-018-05736-x

Roeloffs, E. (1996). Poroelastic Techniques in the Study of Earthquake-Related Hydrologic Phenomena. In R. Dmowska & B. Saltzman (Eds.), Advances in Geophysics (Vol. 37, pp. 135–195). Academic Press. https://doi.org/10.1016/S0065-2687(08)60270-8%0APublisher

Rona, P. A., & Trivett, D. A. (1992). Discrete and diffuse heat transfer at ashes vent field, Axial Volcano, Juan de Fuca Ridge. Earth and Planetary Science Letters, 109(1–2), 57–71. https://doi.org/10.1016/0012-821X(92)90074-6

Ruh, J. B., Sallarès, V., Ranero, C. R., & Gerya, T. (2016). Crustal deformation dynamics and stress evolution during seamount subduction: High-resolution 3-D numerical modeling Jonas. AGU: Journal of Geophysical Research, Solid Earth, 121(9), 6880–6902. https://doi.org/10.1002/2016JB013250

Sacks, S. I., Suyehiro, S., Linde, A. T., & Snoke, J. A. (1978). Slow earthquakes and stress redistribution. Nature, 275(5681), 599–602. https://doi.org/10.1038/275599a0

Saffer, D. M., & Bekins, B. A. (1998). Episodic fluid flow in the Nankai accretionary complex : Timescale, geochemistry, flow rates, and fluid budget. Journal of Geophysical Research: Solid Earth, 103(B12), 30351–30370. https://doi.org/10.1029/98JB01983

Saffer, D. M., & Screaton, E. J. (2003). Fluid flow at the toe of convergent margins: Interpretation of sharp pore-water geochemical gradients. Earth and Planetary Science Letters, 213(3–4), 261–270. https://doi.org/10.1016/S0012-821X(03)00343-1

Saffer, D. M., & Tobin, H. J. (2011). Hydrogeology and mechanics of subduction zone forearcs: Fluid flow and pore pressure. Annual Review of Earth and Planetary Sciences, 39, 157–186. https://doi.org/10.1146/annurev-earth-040610-133408

Saffer, D. M., & Wallace, L. M. (2015). The frictional, hydrologic, metamorphic and thermal habitat of shallow slow earthquakes. Nature Geoscience, 8, 594–600. https://doi.org/10.1038/ngeo2490

Saishu, H., Okamoto, A., & Otsubo, M. (2017). Silica precipitation potentially controls earthquake recurrence in seismogenic zones. Scientific Reports, 7(1), 1–10. https://doi.org/10.1038/s41598-017-13597-5

Sample, J. C., Reid, M. R., Tobin, H. J., & Moore, J. C. (1993). Carbonate cements indicate channeled fluid flow along a zone of vertical faults at the deformation front of the Cascadia accretionary wedge (northwest U.S. coast). Geology, 21(6), 507–510. https://doi.org/10.1130/0091-7613(1993)021<0507:CCICFF>2.3.CO;2

Savin, S. M., & Eptein, S. (1970). The oyxgen and hydrogen isotope geochemistry of ocean sediments and shales. Geochimica et Cosmochimica Acta, 34(1), 43–63. https://doi.org/10.1016/0016-7037(70)90150-X

Schmalzle, G. M., McCaffrey, R., & Creager, K. C. (2014). Central Cascadia subduction zone creep. Geochemistry, Geophysics, Geosystems, 15(4), 1515–1532. https://doi.org/10.1002/2013GC005172.Received

Scholz, C. H. (1998). Earthquakes and friction laws. Nature, 391(6662), 37–42. https://doi.org/10.1038/34097

Scholz, F., Hensen, C., Schmidt, M., & Geersen, J. (2013). Submarine weathering of silicate minerals and the extent of pore water freshening at active continental margins. Geochimica et Cosmochimica Acta, 100, 200–216. https://doi.org/10.1016/j.gca.2012.09.043

Schulz, H. D., Dahmke, A., Schinzel, U., Wallmann, K., & Zabel, M. (1994). Early diagenetic processes, fluxes, and reaction rates in sediments of the South Atlantic. Geochimica et Cosmochimica Acta, 58(9), 2041–2060. https://doi.org/10.1016/0016-7037(94)90284-4

Schulz, H. D., & Zabel, M. (2006). Marine geochemistry. In Eos, Transactions American Geophysical Union. https://doi.org/10.1029/EO052i006pIU237

Schwartz, S. Y., & Rokosky, J. M. (2007). Slow slip events and seismic tremor at circum-Pacific subduction zones. Reviews of Geophysics, 45(3), 1–32. https://doi.org/10.1029/2006RG000208.1.

Seeberg-Elverfeldt, J., Schlüter, M., Feseker, T., & Kölling, M. (2005). Rhizon sampling of porewaters near the sediment-water interface of aquatic systems. Limnology and Oceanography: Methods, 3(8), 361–371. https://doi.org/10.4319/lom.2005.3.361

Seewald, J. S., Doherty, K. W., Hammar, T. R., & Liberatore, S. P. (2001). Instruments and methods A new gas-tight isobaric sampler for hydrothermal fluids. Deep-Sea Research I, 49, 189–196.

Shaddox, H. R., & Schwartz, S. Y. (2019). Subducted seamount diverts shallow slow slip to the forearc of the northern Hikurangi subduction zone, New Zealand. Geology, 47(5), 415–418. https://doi.org/10.1130/G45810.1

Sharqawy, M. H., Lienhard V, J. H., & Zubair, S. M. (2010). Thermophysical properties of seawater: A review of existing correlations and data. Desalination and Water Treatment, 16(1–3), 354–380. https://doi.org/10.5004/dwt.2010.1079

Sheppard, S. M. F., & Gilg, H. A. (1996). Stable Isotope Geochemistry of Clay Minerals. Clay Minerals, 31(1), 1–24. https://doi.org/10.1180/claymin.1996.031.1.01

Sibson, R. H. (1990). Conditions for fault-valve behaviour. Geological Society, London, Special Publications, 54, 15–28. https://doi.org/10.1144/GSL.SP.1990.054.01.02

Sibson, R. H., & Rowland, J. V. (2003). Stress, fluid pressure and structural permeability in seismogenic crust, North Island, New Zealand. Geophysical Journal International, 154(2), 584–594. https://doi.org/10.1046/j.1365-246X.2003.01965.x

Silver, E., Kastner, M., Fisher, A., Morris, J., McIntosh, K., & Saffer, D. (2000). Fluid flow paths in the Middle America Trench and Costa Rica margin. Geology, 28(8), 679–682. https://doi.org/10.1130/0091-7613(2000)28<679:FFPITM>2.0.CO;2

Solomon, E. A., & Kastner, M. (2012). Progressive barite dissolution in the Costa Rica forearc - Implications for global fluxes of Ba to the volcanic arc and mantle. Geochimica et Cosmochimica Acta, 83, 110–124. https://doi.org/10.1016/j.gca.2011.12.021

Solomon, E. A., Kastner, M., Jannasch, H., Robertson, G., & Weinstein, Y. (2008). Dynamic fluid flow and chemical fluxes associated with a seafloor gas hydrate deposit on the northern Gulf of Mexico slope. Earth and Planetary Science Letters, 270(1–2), 95–105. https://doi.org/10.1016/j.epsl.2008.03.024

Solomon, E. A., Kastner, M., Wheat, C. G., Jannasch, H., Robertson, G., Davis, E. E., & Morris, J. D. (2009). Long-term hydrogeochemical records in the oceanic basement and forearc prism at the Costa Rica subduction zone. Earth and Planetary Science Letters, 282(1–4), 240–251. https://doi.org/10.1016/j.epsl.2009.03.022

Solomon, E. A., Spivack, A. J., Kastner, M., Torres, M. E., & Robertson, G. (2014). Gas hydrate distribution and carbon sequestration through coupled microbial methanogenesis and silicate weathering in the Krishna-Godavari Basin, offshore India. Marine and Petroleum Geology, 58(PA), 233–253. https://doi.org/10.1016/j.marpetgeo.2014.08.020

Spinelli, G. A., Giambalvo, E. R., & Fisher, A. T. (2004). Sediment permeability, distribution, and influence on fluxes in oceanic basement. In E. E. Davis & H. Elderfield (Eds.), Hydrogeology of Oceanic Lithosphere (pp. 151–188). Cambridge University Press.

Stein, J. S., & Fisher, A. T. (2001). Multiple scales of hydrothermal circulation in Middle Valley, northern Juan de Fuca Ridge: Physical constraints and geologic models. Journal of Geophysical Research: Solid Earth, 106(B5), 8563–8580. https://doi.org/10.1029/2000jb900395

Stern, R. J. (2002). Subduction zones. Reviews of Geophysics, 40(4), 3-1-3–38. https://doi.org/10.1029/2001RG000108

Suess, E. (1979). Mineral phases formed in anoxic sediments by microbial decomposition of organic matter. Geochimica et Cosmochimica Acta, 43(3), 339–352. https://doi.org/10.1016/0016-7037(79)90199-6

Suess, E. (2014). Marine cold seeps and their manifestations: geological control, biogeochemical criteria and environmental conditions. International Journal of Earth Sciences, 103(7), 1889–1916. https://doi.org/10.1007/s00531-014-1010-0

Suess, E., Bohrmann, G., Von Huene, R., Linke, P., Wallmann, K., Lammers, S., Sahling, H., Winckler, G., Lutz, R. A., & Orange, D. (1998). Fluid venting in the eastern Aleutian subduction zone. Journal of Geophysical Research: Solid Earth, 103(B2), 2597–2614. https://doi.org/10.1029/97jb02131

Sun, T., Ellis, S., & Saffer, D. (2020). Coupled Evolution of Deformation, Pore Fluid Pressure, and Fluid Flow in Shallow Subduction Forearcs. Journal of Geophysical Research: Solid Earth, 125(3), 1–26. https://doi.org/10.1029/2019JB019101

Sun, T., Saffer, D., & Ellis, S. (2020). Mechanical and hydrological effects of seamount subduction on megathrust stress and slip. Nature Geoscience, 13(3), 249–255. https://doi.org/10.1038/s41561-020-0542-0

Teichert, B. M. A., Torres, M. E., Bohrmann, G., & Eisenhauer, A. (2005). Fluid sources, fluid pathways and diagenetic reactions across an accretionary prism revealed by Sr and B geochemistry. Earth and Planetary Science Letters, 239(1–2), 106–121. https://doi.org/10.1016/j.epsl.2005.08.002

Teske, A., Lizarralde, D., T.W. Höfig, Aiello, I. W., Ash, J. L., Bojanova, D. P., Buatier, M. D., Edgcomb, V. P., Galerne, C. Y., Gontharet, S., Heuer, V. B., Jiang, S., Kars, M. A. C., Singh, S. K., Kim, J.-H., Koornneef, L. M. T., Marsaglia, K. M., Meyer, N. R., Morono, Y., … Zhuang, G. (2021). Site U1546. Proceedings of the International Ocean Discovery Program Volume 385, 1–78. https://doi.org/10.14379/iodp.proc.385.104.2021

Tobin, H. J., Moore, J. C., MacKay, M. E., Orange, D. L., & Kulm, L. D. (1993). Fluid flow along a strike-slip fault at the toe of the Oregon accretionary prism: Implications for the geometry of frontal accretion. Bulletin of the Geological Society of America, 105(5), 569–582. https://doi.org/10.1130/0016-7606(1993)105<0569:FFAASS>2.3.CO;2

Tobin, H. J., & Saffer, D. M. (2009). Elevated fluid pressure and extreme mechanical weakness of a plate boundary thrust, Nankai Trough subduction zone. Geology, 37(8), 679–682. https://doi.org/10.1130/G25752A.1

Toki, T., Higa, R., Ijiri, A., Tsunogai, U., & Ashi, J. (2014). Origin and transport of pore fluids in the Nankai accretionary prism inferred from chemical and isotopic compositions of pore water at cold seep sites off Kumano. Earth, Planets and Space, 66(137), 1–14. https://doi.org/10.1186/s40623-014-0137-3

Torres, M. E., Bohrmann, G., & Suess, E. (1996). Authigenic barites and fluxes of barium associated with fluid seeps in the Peru subduction zone. Earth and Planetary Science Letters, 144(3–4), 469–481. https://doi.org/10.1016/s0012-821x(96)00163-x

Torres, M. E., Hong, W. L., Solomon, E. A., Milliken, K., Kim, J. H., Sample, J. C., Teichert, B. M. A., & Wallmann, K. (2020). Silicate weathering in anoxic marine sediment as a requirement for authigenic carbonate burial. Earth-Science Reviews, 200(January 2019), 102960. https://doi.org/10.1016/j.earscirev.2019.102960

Torres, M. E., McManus, J., Hammond, D. E., de Angekis, M. A., Heeschen, K. U., Colbert, S. L., Tryon, M. D., Brown, K. M., & Suess, E. (2002). Fluid and chemical Fluxes in and out of sediments hosting methane hydrate deposits on Hydrate Ridge, OR, I: Hydrological provinces. Earth and Planetary Science Letters, 201(3–4), 541–557. https://doi.org/10.1016/S0012-821X(02)00732-X

Torres, M. E., Mix, A. C., & Rugh, W. D. (2005). Precise δ13C analysis of dissolved inorganic carbon in natural waters using automated headspace sampling and continuous-flow mass spectrometry. Limnology and Oceanography: Methods, 3(8), 349–360. https://doi.org/10.4319/lom.2005.3.349

Torres, M. E., Teichert, B. M. A., Tréhu, A. M., Borowski, W., & Tomaru, H. (2004). Relationship of pore water freshening to accretionary processes in the Cascadia margin:

Fluid sources and gas hydrate abundance. Geophysical Research Letters, 31(22), 1–4. https://doi.org/10.1029/2004GL021219

Torres, M. E., Wallmann, K., Tréhu, A. M., Bohrmann, G., Borowski, W. S., & Tomaru, H. (2004). Gas hydrate growth, methane transport, and chloride enrichment at the southern summit of Hydrate Ridge, Cascadia margin off Oregon. Earth and Planetary Science Letters, 226(1–2), 225–241. https://doi.org/10.1016/j.epsl.2004.07.029

Tréhu, A. M., Flemings, P. B., Bangs, N. L., Chevallier, J., Gràcia, E., Johnson, J. E., Liu, C. S., Liu, X., Riedel, M., & Torres, M. E. (2004). Feeding methane vents and gas hydrate deposits at south Hydrate Ridge. Geophysical Research Letters, 31(23), 1–4. https://doi.org/10.1029/2004GL021286

Tréhu, A. M., Bohrmann, G., Torres, M. E., & Colwell, F. S. (2006). Drilling Gas Hydrates on Hydrate Ridge, Cascadia Continental Margin. Proceedings of the Ocean Drilling Program Volume 204 Scientific Results. https://doi.org/10.2973/odp.proc.sr.204.2006

Tryon, M., Brown, K., Dorman, L. R., & Sauter, A. (2001). A new benthic aqueous flux meter for very low to moderate discharge rates. Deep-Sea Research Part I: Oceanographic Research Papers, 48(9), 2121–2146. https://doi.org/10.1016/S0967-0637(01)00002-4

Tryon, M. D., Brown, K. M., Torres, M. E., Tréhu, A. M., McManus, J., & Collier, R. W. (1999). Measurements of transience and downward fluid flow near episodic methane gas vents, Hydrate Ridge, Cascadia. Geology, 27(12), 1075–1078. https://doi.org/10.1130/0091-7613(1999)027<1075:MOTADF>2.3.CO;2

Tryon, M. D., Wheat, C. G., & Hilton, D. R. (2010). Fluid sources and pathways of the Costa Rica erosional convergent margin. Geochemistry, Geophysics, Geosystems, 11(4), 1–15. https://doi.org/10.1029/2009GC002818

Underwood, M. B. (2007). Sediment Inputs to Subduction Zones: Why Lithostratigraphy and Clay Mineralogy Matter. In T. H. Dixon & J. C. Moore (Eds.), The Seismogenic Zone of Subduction Thrust Faults. Columbia University Press. https://www.jstor.org/stable/10.7312/dixo13866.6

Van Der Kamp, G., & Gale, J. E. (1983). Theory of earth tide and barometric effects in porous formations with compressible grains. Water Resources Research, 19(2), 538–544. https://doi.org/10.1029/WR019i002p00538

Vasseur, G., Demongodin, L., & Bonneville, A. (1993). Thermal modelling of fluid flow effects In thin-dipping aquifers. Geophysical Journal International, 112(2), 276–289. https://doi.org/10.1111/j.1365-246X.1993.tb01455.x

Verma, S. P., & Santoyo, E. (1997). New improved equations for Na/K, Na/Li and SiO2 geothermometers by outlier detection and rejection. Journal of Volcanology and Geothermal Research, 79(1–2), 9–23. https://doi.org/10.1016/S0377-0273(97)00024-3

Villinger, H., & Davis, E. E. (1987). A new reduction algorithm for marine heat flow measurements. Journal of Geophysical Research: Solid Earth, 92(B12), 12846–12856. https://doi.org/10.1029/jb092ib12p12846

Von Damm, K. L. (1990). Seafloor hydrothermal activity: black smoker chemistry and chimneys. Annual Review of Earth & Planetary Sciences, 18, 173–204. https://doi.org/10.1146/annurev.ea.18.050190.001133

Von Damm, K. L., Edmond, J. M., Grant, B., Measures, C. I., Walden, B., & Weiss, R. F. (1985). Chemistry of submarine hydrothermal solutions at 21 °N, East Pacific Rise. Geochimica et Cosmochimica Acta, 49(11), 2197–2220. https://doi.org/10.1016/0016-7037(85)90222-4

von Huene, R., & Kulm, L. D. (1973). Tectonic Summary of Leg 18. Initial Reports of the Deep Sea Drilling Project, 18, 5, 961–976. https://doi.org/10.2973/dsdp.proc.18.133.1973

Wadleigh, M. A., Veizer, J., & Brooks, C. (1985). Strontium and its isotopes in Canadian rivers: Fluxes and global implications. Geochimica et Cosmochimica Acta, 49(8), 1727–1736. https://doi.org/10.1016/0016-7037(85)90143-7

Wallace, L. M. (2020). Slow Slip Events in New Zealand. Annual Review of Earth & Planetary Sciences, 48, 175–203. https://doi.org/10.1146/annurev-earth-071719-055104

Wallace, L. M., Saffer, D. M., Barnes, P. M., Pecher, I. A., Petronotis, K. E., & LeVay, L. J. (2019). Hikurangi Subduction Margin Coring, Logging, and Observatories. Proceedings of the International Ocean Discovery Program, 372B/375. https://doi.org/10.14379/iodp.proc.372B375.2019

Wallace, L. M., Webb, S. C., Ito, Y., Mochizuki, K., Hino, R., Henrys, S., Schwartz, S. Y., & Sheehan, A. F. (2016). Slow slip near the trench at the Hikurangi subduction zone, New Zealand. Science, 352(6286), 701–704. https://doi.org/10.1126/science.aaf2349

Wallmann, K., Aloisi, G., Haeckel, M., Tishchenko, P., Pavlova, G., Greinert, J., Kutterolf, S., & Eisenhauer, A. (2008). Silicate weathering in anoxic marine sediments. Mineralogical Magazine, 72(1), 363–366. https://doi.org/10.1180/minmag.2008.072.1.363

Walter, L. M., Bischof, S. A., Patterson, W. P., & Lyons, T. W. (1993). Dissolution and recrystallization in modern shelf carbonates: evidence from pore water and solid phase chemistry. Philosophical Transactions - Royal Society of London, A, 344(1670), 27–36. https://doi.org/10.1098/rsta.1993.0072

Walton, M. A. L., Staisch, L. M., Dura, T., Pearl, J. K., Sherrod, B., Gomberg, J., Engelhart, S., Tréhu, A., Watt, J., Perkins, J., Witter, R. C., Bartlow, N., Goldfinger, C., Kelsey, H., Morey, A. E., Sahakian, V. J., Tobin, H., Wang, K., Wells, R., & Wirth, E. (2021). Toward an integrative geological and geophysical view of cascadia subduction zone earthquakes. Annual Review of Earth and Planetary Sciences, 49, 367–398. https://doi.org/10.1146/annurev-earth-071620-065605

Wang, K., & Bilek, S. L. (2014). Invited review paper: Fault creep caused by subduction of rough seafloor relief. Tectonophysics, 610, 1–24. https://doi.org/10.1016/j.tecto.2013.11.024

Wang, K., & Davis, E. E. (1996). Theory for the propagation of tidally induced pore pressure variations in layered subseafloor formations. Journal of Geophysical Research: Solid Earth, 101(5), 11483–11495. https://doi.org/10.1029/96jb00641

Wang, K., & Tréhu, A. M. (2016). Invited review paper: Some outstanding issues in the study of great megathrust earthquakes—The Cascadia example. Journal of Geodynamics, 98, 1–18. https://doi.org/10.1016/j.jog.2016.03.010

Warren-Smith, E., Fry, B., Wallace, L., Chon, E., Henrys, S., Sheehan, A., Mochizuki, K., Schwartz, S., Webb, S., & Lebedev, S. (2019). Episodic stress and fluid pressure cycling in subducting oceanic crust during slow slip. Nature Geoscience, 12(6), 475–481. https://doi.org/10.1038/s41561-019-0367-x

Watson, S. J., Mountjoy, J. J., Barnes, P. M., Crutchley, G. J., Lamarche, G., Higgs, B., Hillman, J., Orpin, A. R., Micallef, A., Neil, H., Mitchell, J., Pallentin, A., Kane, T., Woelz, S., Bowden, D., Rowden, A. A., & Pecher, I. A. (2020). Focused fluid seepage related to variations in accretionary wedge structure, Hikurangi margin, New Zealand. Geology, 48(1), 56–61. https://doi.org/10.1130/G46666.1

Wei, W. (2007). Fluid origins, paths, and fluid-rock reactions at convergent margins, using halogens, Cl stable isotopes, and alkali metals as geochemical tracers [Doctor of Philosophy]. University of California, San Diego.

Wheat, C. G., & Fisher, A. T. (2008). Massive, low-temperature hydrothermal flow from a basaltic outcrop on 23 Ma seafloor of the Cocos Plate: Chemical constraints and implications. Geochemistry, Geophysics, Geosystems, 9(12). https://doi.org/10.1029/2008GC002136

Wheat, C. G., Fisher, A. T., McManus, J., Hulme, S. M., & Orcutt, B. N. (2017). Cool seafloor hydrothermal springs reveal global geochemical fluxes. Earth and Planetary Science Letters, 476, 179–188. https://doi.org/10.1016/j.epsl.2017.07.049

Wheat, C. G., Jannasch, H. W., Kastner, M., Plant, J. N., & DeCarlo, E. H. (2003). Seawater transport and reaction in upper oceanic basaltic basement: Chemical data from continuous monitoring of sealed boreholes in a ridge flank environment. Earth and Planetary Science Letters, 216(4), 549–564. https://doi.org/10.1016/S0012-821X(03)00549-1

Whorley, T. L. (2021). The response of seep and methane hydrate biogeochmical systems to variability in climate, hydrogeology, and trace metal availability [Doctor of Philosophy]. University of Washington.

Wiersberg, T., Hammerschmidt, S. B., Fuchida, S., Kopf, A., & Erzinger, J. (2018). Mantle-derived fluids in the Nankai Trough Kumano forearc basin. Progress in Earth and Planetary Science, 5(1). https://doi.org/10.1186/s40645-018-0235-0

Wilke, C. R., & Chang, P. (1955). Correlation of diffusion coefficients in dilute solutions. AIChE Journal, 1(2), 264–270. https://doi.org/10.1002/aic.690010222

Wilson, D. S. (2002). The Juan de Fuca plate and slab: Isochron structure and Cenozoic plate motions. In The Cascadia Subduction Zone and Related Subduction Systems: Seismic Structure, Intraslab Earthquakes and Processes, and Earthquake Hazards.

Wintsch, R. P., Christoffersen, R., & Kronenberg, A. K. (1995). Fluid-rock reaction weakening of fault zones. Journal of Geophysical Research, 100(B7). https://doi.org/10.1029/94jb02622

Woods, K., Wallace, L., Williams, C. A., Hamling, I. J., Spahr, C., Ito, Y., Palmer, N., Hino, R., Suzuki, S., Kane, M., Warren-smith, E., & Mochizuki, K. (2024). Spatiotemporal Evolution of Slow Slip Events at the Offshore Hikurangi Subduction Zone in 2019 using GNSS, InSAR, and seafloor geodetic data. Journal of Geophysical Research.

Woods, K., Webb, S. C., Wallace, L. M., Ito, Y., Collins, C., Palmer, N., Hino, R., Savage, M. K., Saffer, D. M., Davis, E. E., & Barker, D. H. N. (2022). Using Seafloor Geodesy to Detect Vertical Deformation at the Hikurangi Subduction Zone: Insights From Self-Calibrating Pressure Sensors and Ocean General Circulation Models. Journal of Geophysical Research: Solid Earth, 127(12), 1–22. https://doi.org/10.1029/2022JB023989

Yarce, J., Sheehan, A., Roecker, S., & Mochizuki, K. (2021). Seismic Velocity Heterogeneity of the Hikurangi Subduction Margin, New Zealand: Elevated Pore Pressures in a Region With Repeating Slow Slip Events. Journal of Geophysical Research: Solid Earth, 126(5), 1–17. https://doi.org/10.1029/2020jb021605

Yeh, H. W., & Epstein, S. (1978). Hydrogen isotope exchange between clay minerals and sea water. Geochimica et Cosmochimica Acta, 42(1), 140–143. https://doi.org/10.1016/0016-7037(78)90224-7

Yeh, H. W., & Eslinger, E. V. (1986). Oxygen isotopes and the extent of diagenesis of clay minerals during sedimentation and burial in the sea. Clays & Clay Minerals, 34(4), 403–406. https://doi.org/10.1346/CCMN.1986.0340407

Yeh, H. W., & Savin, S. M. (1976). The extent of oxygen isotope exchange between clay minerals and sea water. Geochimica et Cosmochimica Acta, 40(7), 743–748. https://doi.org/10.1016/0016-7037(76)90027-2

Yeh, H. W. (1980). D / H Ratios and late-stage dehydration of shales during burial Sample preparation. Geochimca et Cosmochimica Acta, 44(2), 341–352.

You, C. F., Castillo, P. R., Gieskes, J. M., Chan, L. H., & Spivack, A. J. (1996). Trace element behavior in hydrothermal experiments: Implications for fluid processes at shallow depths in subduction zones. Earth and Planetary Science Letters, 140(1–4), 41–52. https://doi.org/10.1016/0012-821X(96)00049-0

You, K., Flemings, P. B., Malinverno, A., Collett, T. S., & Darnell, K. (2019). Mechanisms of Methane Hydrate Formation in Geological Systems. Reviews of Geophysics, 57(4), 1146–1196. https://doi.org/10.1029/2018RG000638

Zal, H. J., Jacobs, K., Savage, M. K., Yarce, J., Mroczek, S., Graham, K., Todd, E. K., Nakai, J., Iwasaki, Y., Sheehan, A., Mochizuki, K., Wallace, L., Schwartz, S., Webb, S., & Henrys, S. (2020). Temporal and spatial variations in seismic anisotropy and VP/VS ratios in a region of slow slip. Earth and Planetary Science Letters, 532, 115970. https://doi.org/10.1016/j.epsl.2019.115970

APPENDIX A: SUPPLEMENTARY INFORMATION FOR CHAPTER 2

INTRODUCTION

In this supporting information, Figures A1 to A6 show all heat flow results using the 3.5-m probe on the 2019 SAFFRONZ expedition (R/V Revelle Expedition RR1901/1902). Successful determinations as well as attempted measurement locations are shown in map view for each site; successful determinations are also shown in profile view. Heat flow data are available at https://www.marine-geo.org/tools/files/31405 (Harris et al., 2023). Figures A7 and A8 show all pore water data used in this study from cores collected at the southern and northern margin, respectively. The complete pore water geochemistry dataset plotted in Figures A7 and A8 is available at https://doi.org/10.60520/IEDA/113176 (Aylward et al., 2024). Figures A9 and A10 provide plots of data from previous studies to provide useful context for interpretation of the pore water geochemistry data we present

Tables A1 provides the input parameters used for pore water advection rate modeling. Table A2 details the results of the advection rate modeling for the 33 sediment cores discussed in this study. Advection rate estimates are likely less reliable for the cores collected in the southern margin since all estimates were made in reference to IODP Sites U1518 and U1519 which are located in the northern margin.

SUPPLEMENTARY FIGURES AND TABLES

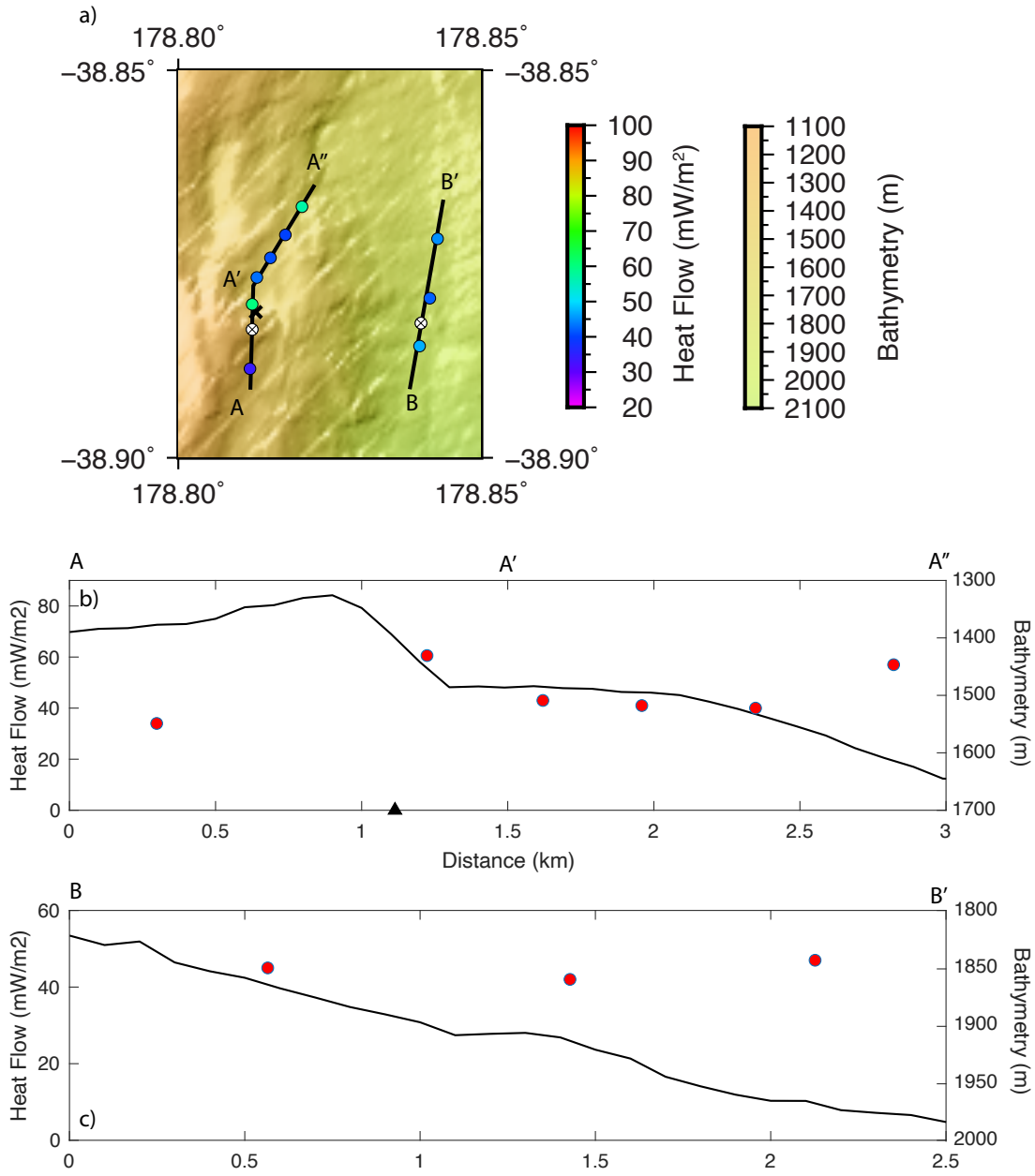

Figure A1. Heat flow data at Site 1N.

a) Map view of heat flow data. Heat flow measurements are shown by circles color coded by value. White circles with 'x' show unsuccessful heat flow measurement. Bold 'x' show mapped seepage indicators [Watson et al., 2020]. b) Profile A-A', circles show heat flow values, solid line shows bathymetry, and triangles show seep locations. c) Profile B-B', circles show heat flow values, solid line shows bathymetry.

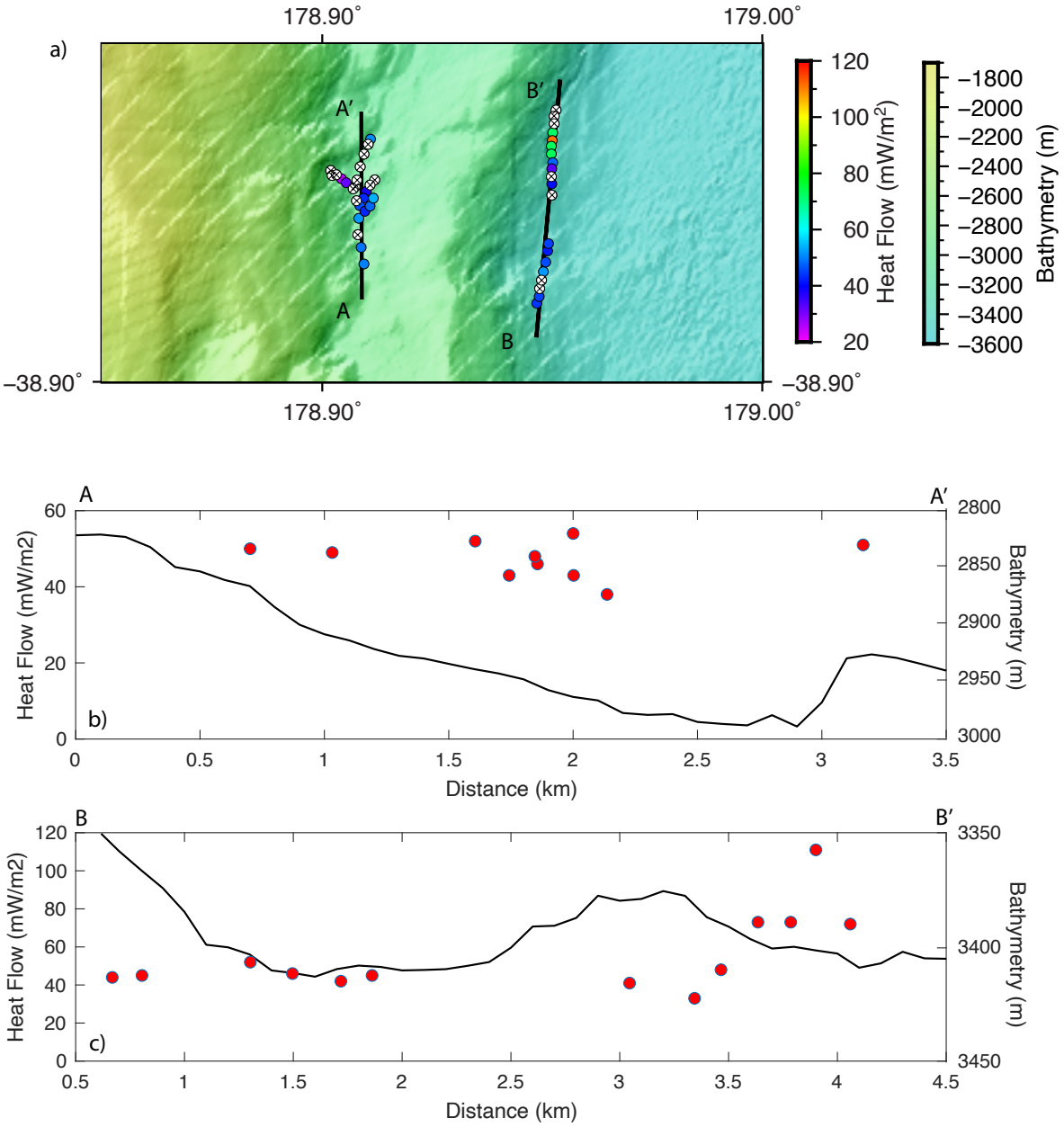

Figure A2. Heat flow data at Site HFA_N.
a) Map view of heat flow data. Heat flow measurements are shown by circles color coded by value. White circles with 'x' show unsuccessful heat flow measurement. b) Profile A-A', circles show heat flow values, solid line shows bathymetry. c) Profile B-B', circles show heat flow values, solid line shows bathymetry.

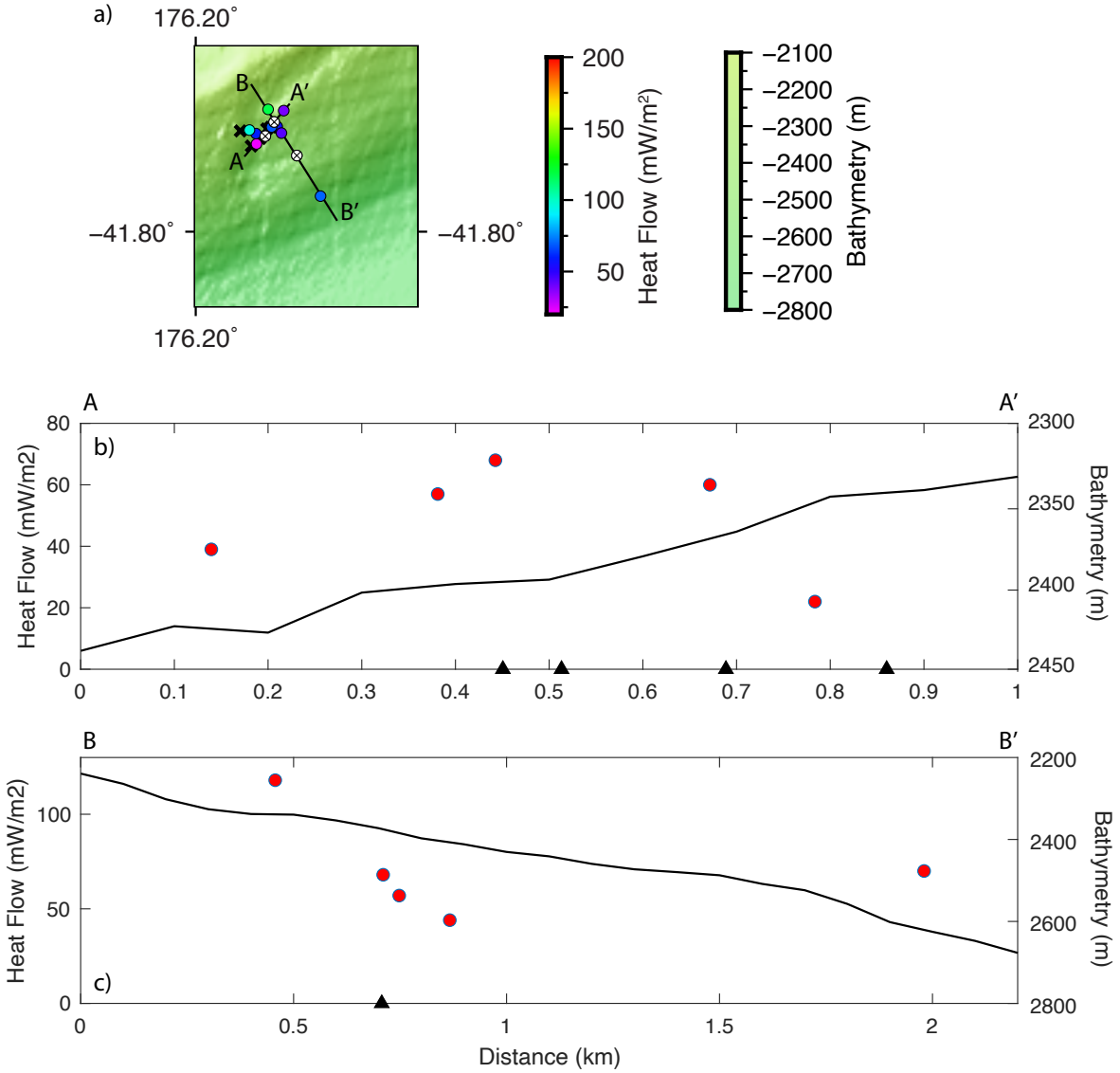

Figure A3. Heat flow data at Site 1S.
a) Map view of heat flow data. Heat flow measurements are shown by circles color coded by value. White circles with ‘x’ show unsuccessful heat flow measurement. Bold ‘x’ show mapped seepage indicators [Watson et al., 2020]. b) Profile A-A’, circles show heat flow values, solid line shows bathymetry, and triangles show seep locations. c) Profile B-B’, circles show heat flow values, solid line shows bathymetry, and triangles show seep locations.

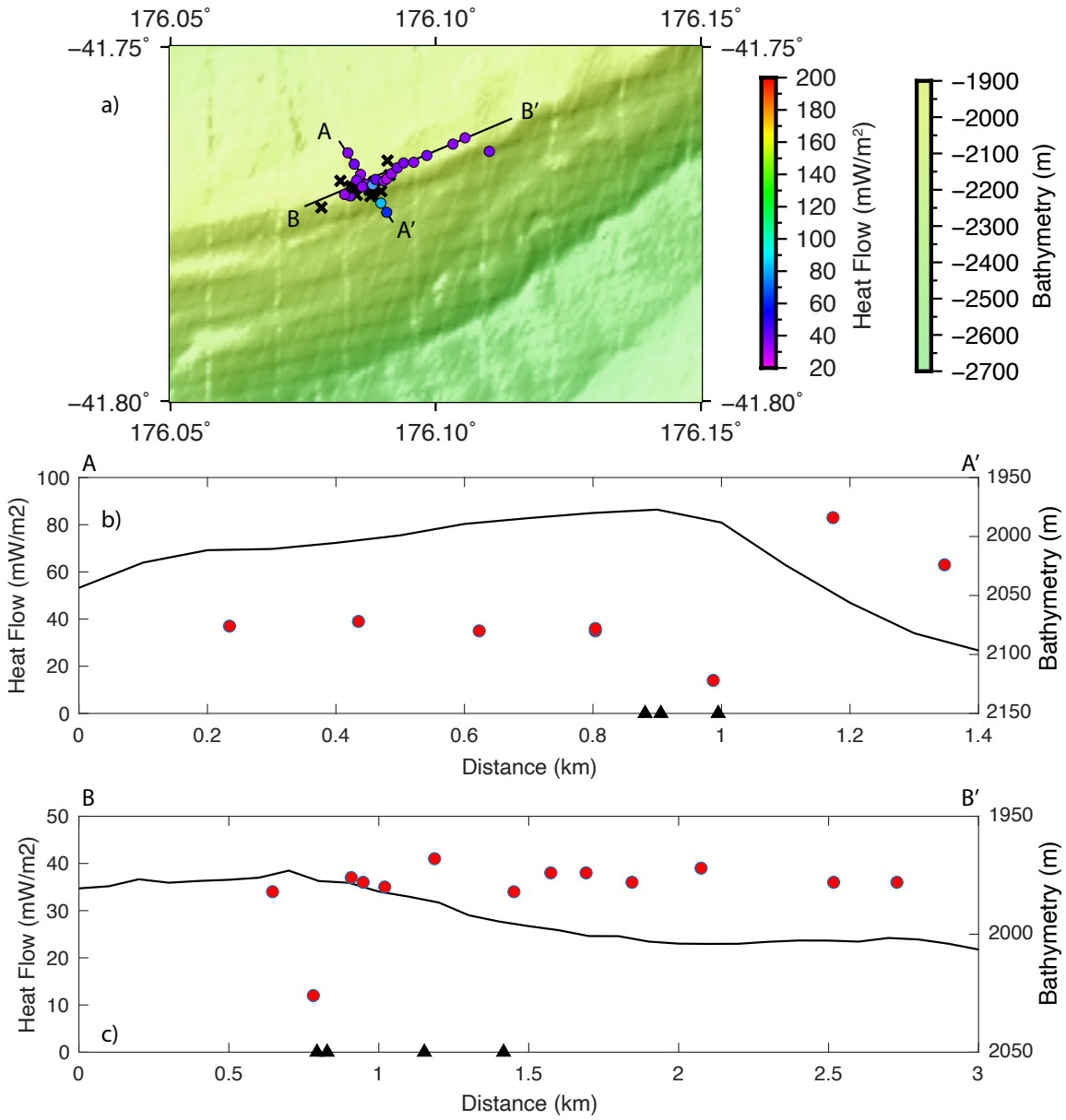

Figure A4. Heat flow data at Site 2S.
a) Map view of heat flow data. Heat flow measurements are shown by circles color coded by value. Bold ‘x’ show mapped seepage indicators [Watson et al., 2020]. b) Profile A-A’, circles show heat flow values, solid line shows bathymetry, and triangles show seep locations. c) Profile B-B’, circles show heat flow values, solid line shows bathymetry, and triangles show seep locations.

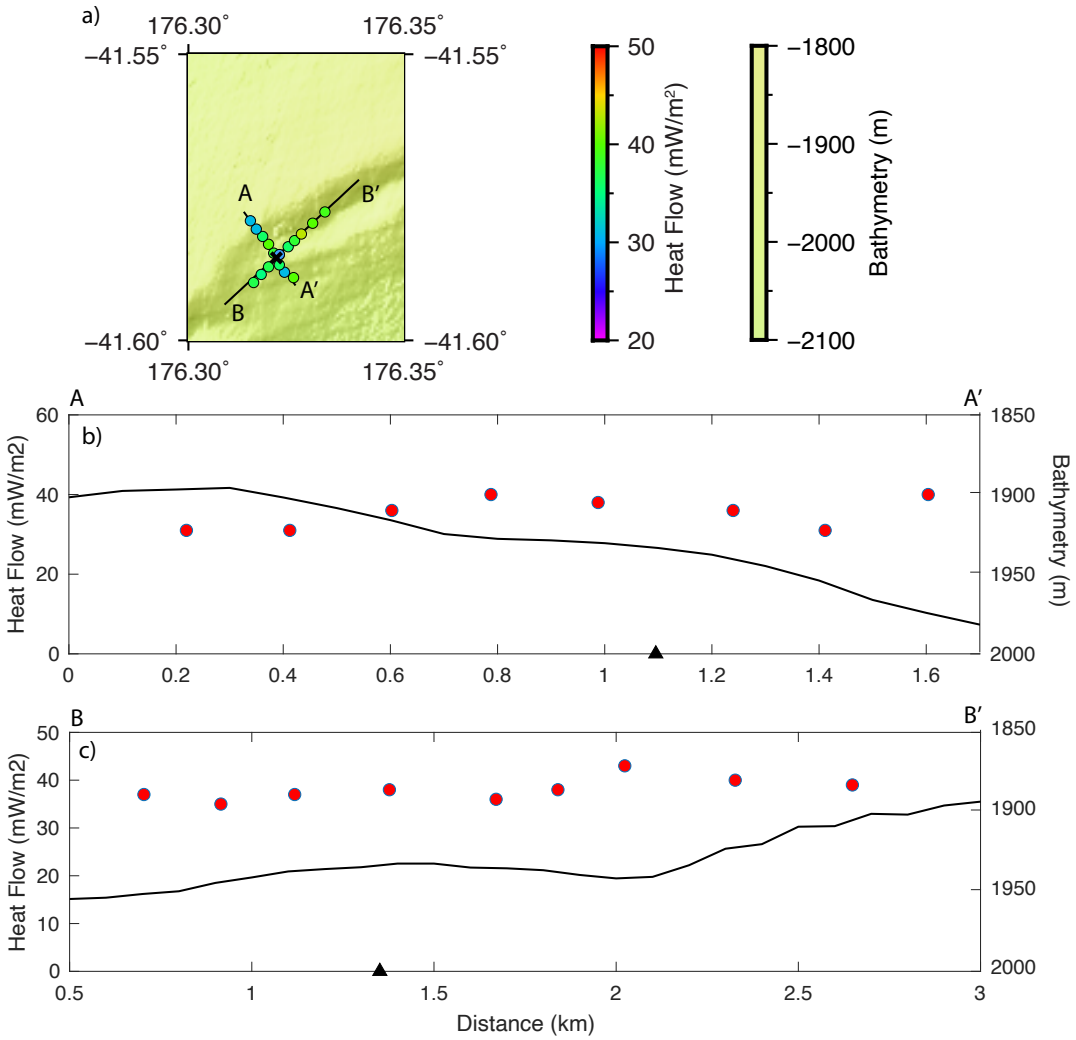

Figure A5. Heat flow data at Site 3S.
a) Map view of heat flow data. Heat flow measurements are shown by circles color coded by value. Bold 'x' show mapped seepage indicators [Watson et al., 2020]. b) Profile A-A', circles show heat flow values, solid line shows bathymetry, and triangles show seep locations. c) Profile B-B' circles show heat flow values, solid line shows bathymetry, and triangles show seep locations.

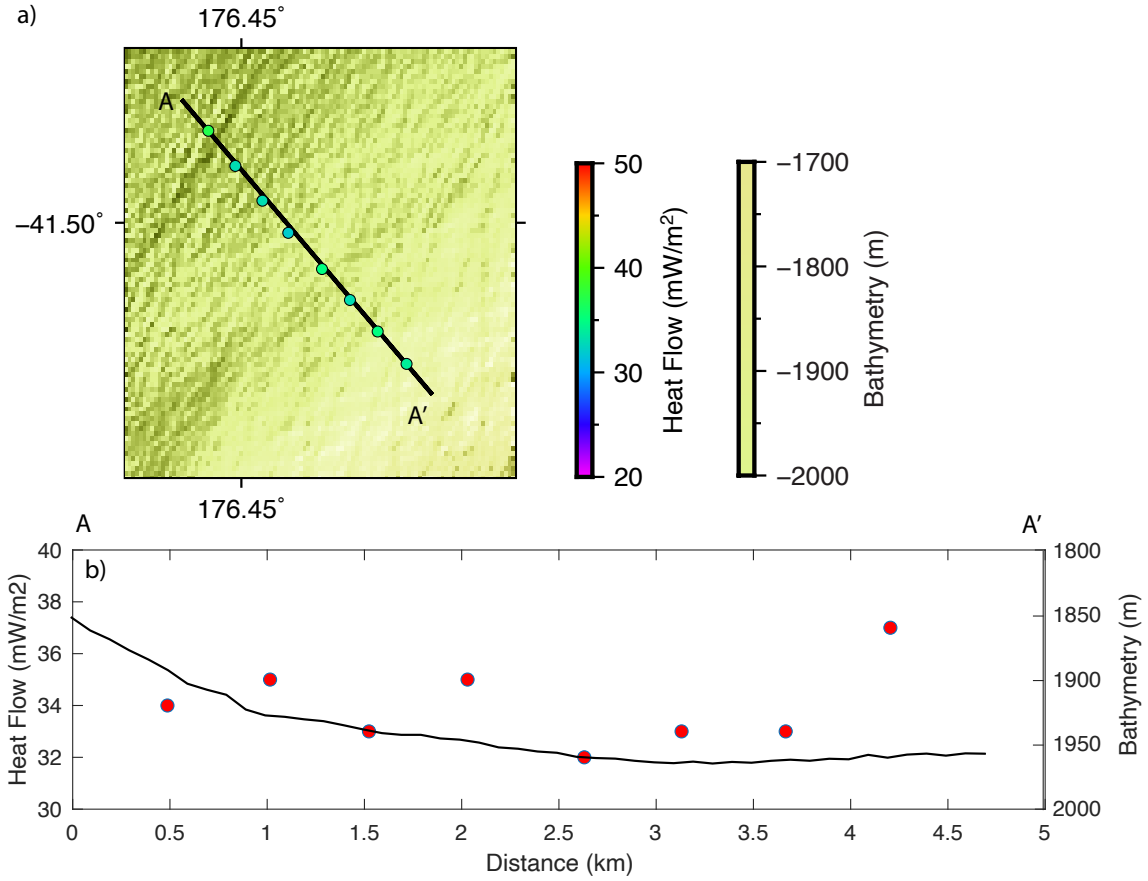

Figure A6. Heat flow data at Site HFA_S.
a) Map view of heat flow data. Heat flow measurements are shown by circles color coded by value. b) Profile A-A', circles show heat flow values, solid line shows bathymetry.

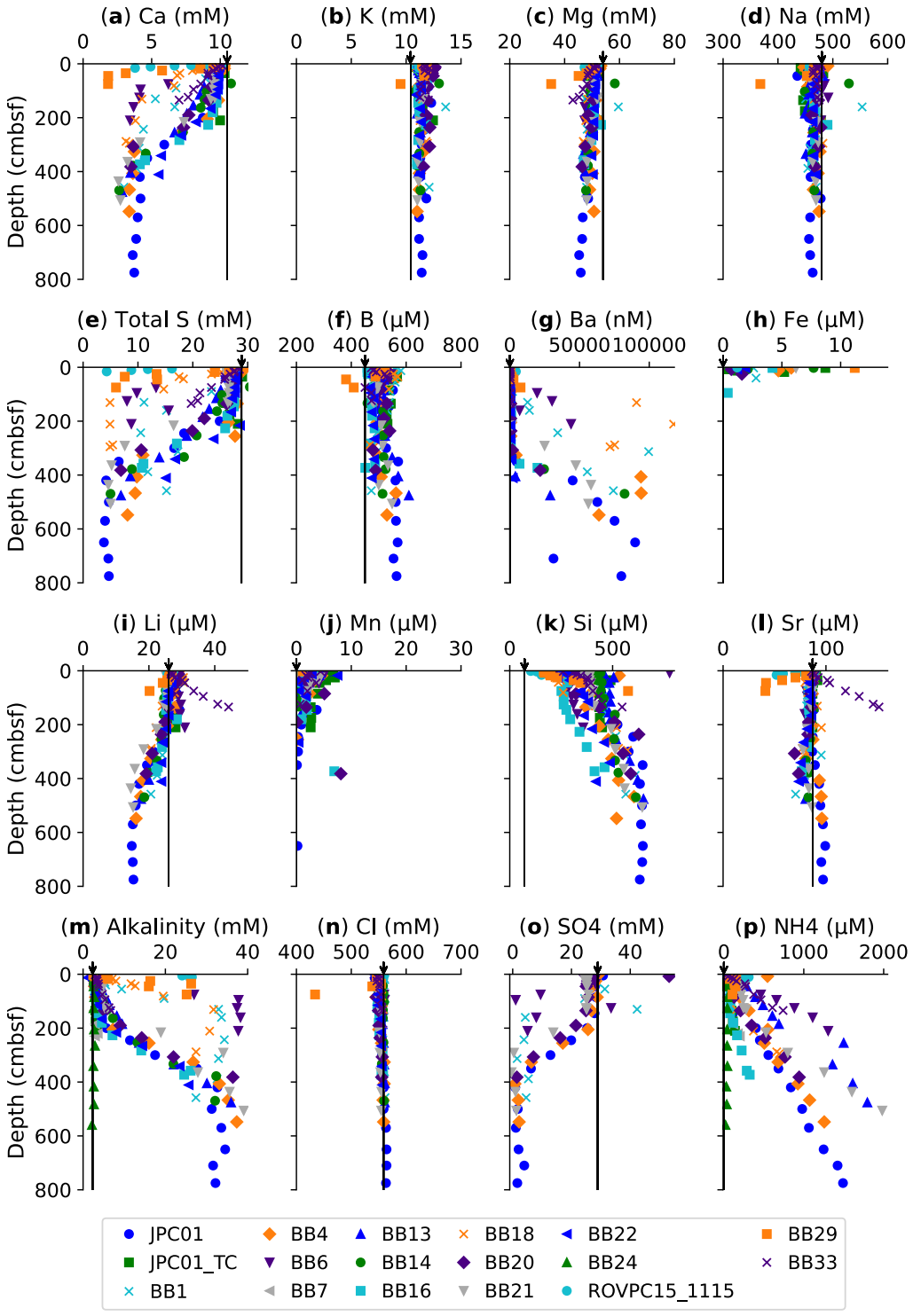

Figure A7. Pore water solute profiles for all southern margin cores.
Gravity, piston, and push cores have prefixes “BB,” “JPC,” and “ROVPC,” respectively. Seawater concentration is denoted by a black arrow and vertical line. Not all solutes were analyzed for every core.

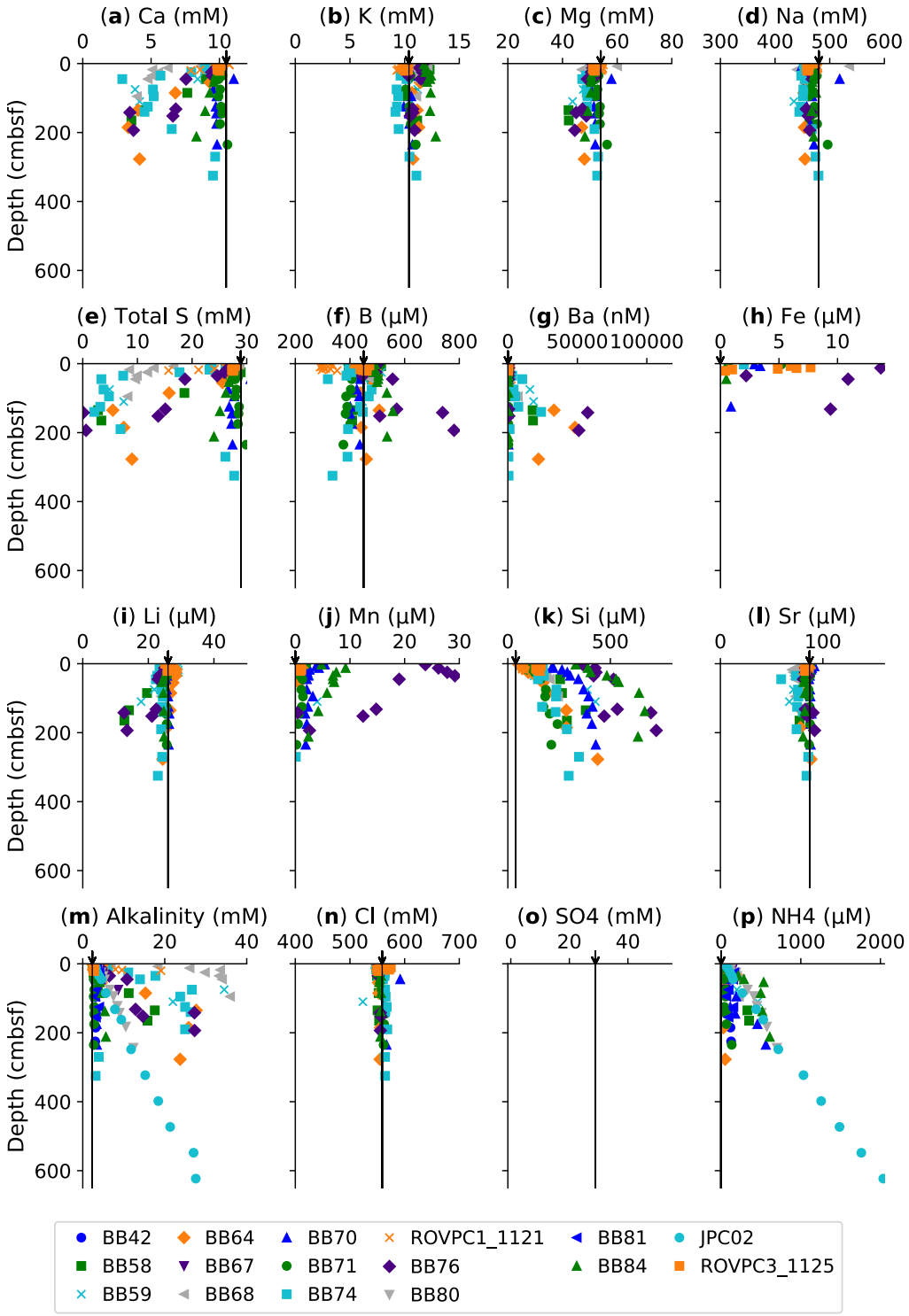

Figure A8. Pore water solute profiles for all northern margin cores.
Gravity, piston, and push cores have prefixes “BB,” “JPC,” and “ROVPC,” respectively. Seawater concentration is denoted by a black arrow and vertical line. Not all solutes were analyzed for every core.

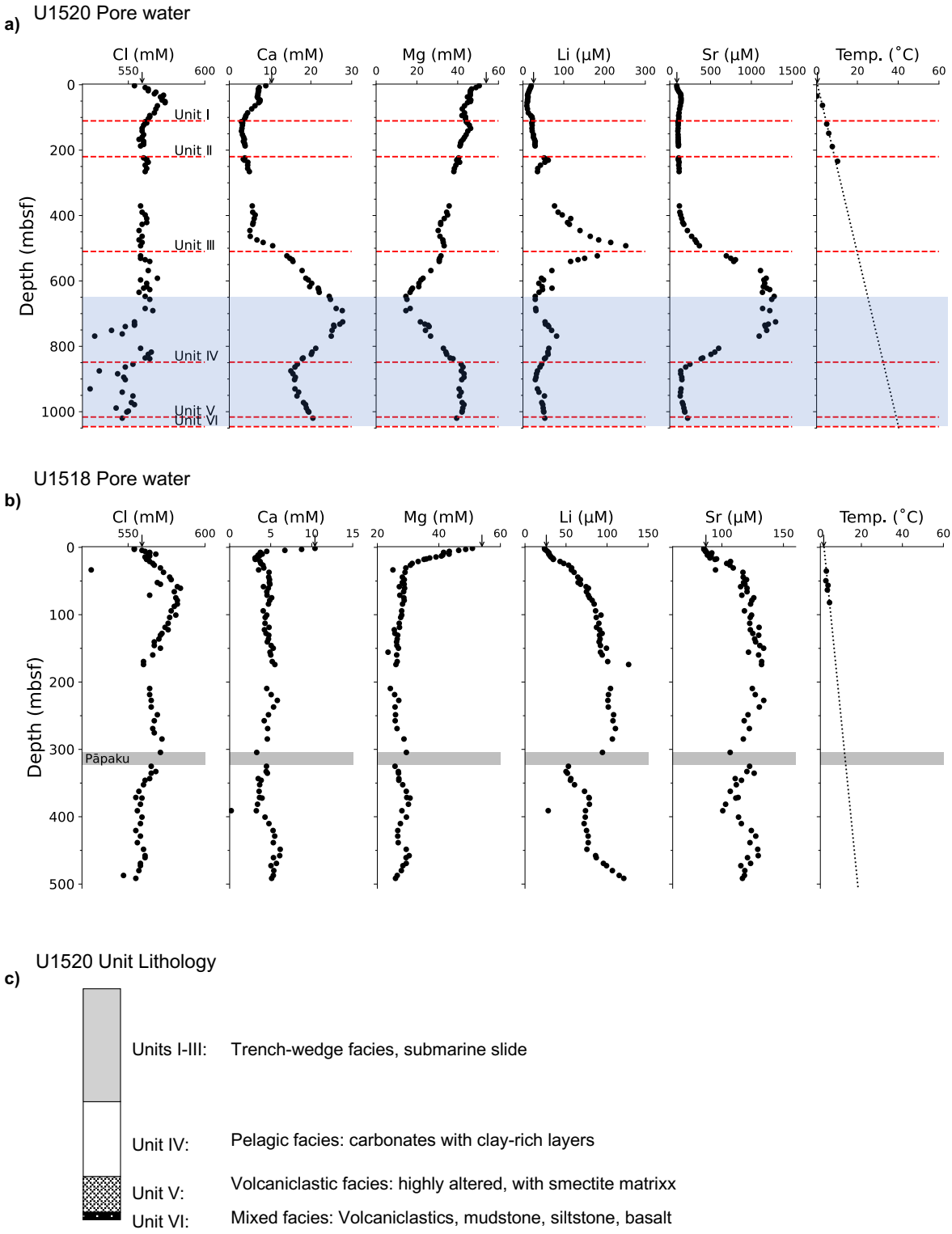

Figure A9. Pore water and sediment lithology at northern Hikurangi IODP Sites.
Pore water Cl, Ca, Mg, Li, and Sr, and temperature profiles with depth for the sediments drilled at (a) Site U1520 and (b) Site U1518 (Wallace et al., 2019). Black arrows show seawater values. Blue shaded region in (a) is the interval correlated to subduction interface zone (Barnes et al.,

2020); gray shaded region in (b) corresponds to the Pāpaku Fault Zone (depths 304.2 – 322.4 mbsf from Morgan et al., 2022). (c) Simplified lithology of IODP Site U1520 (Wallace et al., 2019; Barnes et al., 2020).

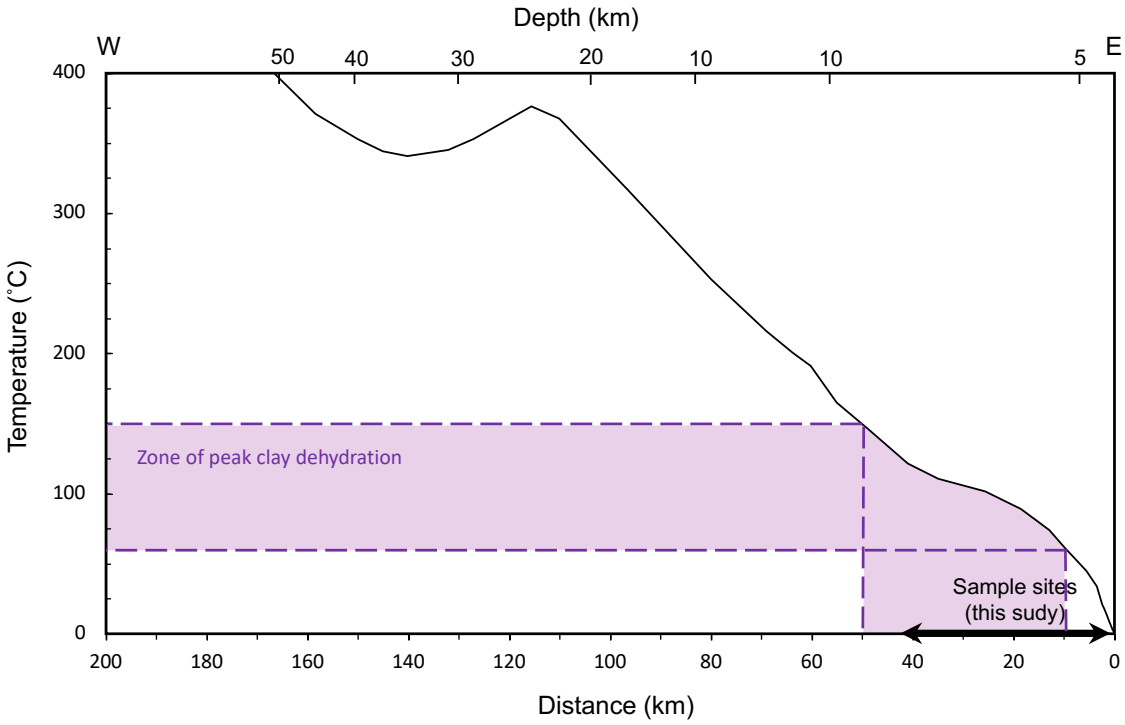

Figure A10. Temperature along the plate boundary versus distance from the deformation front. Solid black line shows modeled temperature as a function of the variable effective coefficient of friction (Antriasian et al., 2019). The zone of sites sampled in this study (thick black arrow) overlap with the zone of peak clay dehydration (60 – 150 ˚C, shaded purple).

Table A1. Advection rate model input parameters for reference Sites U1518 and U1519. NH4 reaction rates (separated into 3 zones of near-constant slope) were modeled for reference (non-seep) Sites U1518 and U1519 given an advection rate of 0 cm/yr. "Synthetic" advection rates were then modeled using the pre-determined NH4 reaction rates (all other input parameters remained the same). NH4 concentrations, porosity, and temperature data are from Wallace et al., (2019). Bottom boundary NH4 concentration at U1518 (Hole E) is an average of two points where the profile temporarily reaches near-asymptotic values; the U1519 NH4 profile is steadier and the bottom boundary is set to the bottom of Hole E. Sedimentation rates are averages from Crundwell and Woodhouse, (2022). Reference diffusivity for NH4 at 18 ˚C from Li & Gregory, (1974).

Site	Porosity	Bottom Water Temp. (˚C)	Geo-thermal Gradient (˚C/m)	Sedimen-tation Rate (m/yr)	Reference Diffusivity (cm^2/s)	Top Boundary [NH_4] (μM)	Bottom Boundary [NH_4] (μM)	Bottom Boundary Depth (mbsf)	Reaction Zone	Depth Range of Reaction Zone (mbsf)	Modeled NH_4 Reaction Rate ($mol/m^3/yr$)
U1518	Variable (measured)	1.6	0.035	2.15E+03	1.68E-05	0	8750*	56.6*	1	0 - 14.3	1.00E-07
									2	14.3 - 54.8	1.00E-04
									3	54.8 - 56.6	-8.00E-06
U1519	Variable (measured)	5.7	0.025	1.80E-03	1.68E-05	0	3660	84.7	1	0 - 20.9	1.20E-04
									2	20.9 - 32.5	9.00E-06
									3	32.5 - 84.7	3.50E-06

*average between measured values at 54.8 and 58.4 mbsf.

Table A2. Flow rate model results.
ND indicates No Data. 0 indicates no upward flow was detected. Gravity, piston, and push cores have prefixes “BB,” “JPC,” and “ROVPC” respectively; “S” and “N” in site names denote southern and northern margins respectively. The depth of near-seawater alkalinity profile is the depth of the mixed layer.

Core	Site	Reference Site	Penetration depth (cmbsf)	Depth of Near-SW Alk Profile (cm)	Estimated upward advection rate (cm/yr)
JPC01	2S	U1518	775	145	0.05
JPC01_TC	2S	U1518	210	210 (all)	0
BB1	2S	U1518	458	0	ND
BB4	2S	U1518	548	135	0.05
BB6	1S	U1518	210	35	0.1
BB7	1S	U1518	230	230 (all)	0
BB13	3S	U1518	476	0	0.06
BB14	3S	U1518	469.5	25	ND
BB16	4S	U1519	373	145	0
BB18	4S	U1519	295	0	0
BB20	4S	U1519	382	45	0.04
BB21	5S	U1519	506	125	0.2
BB22	5S	U1519	411	166	ND
BB24	5S	U1519	559.5	559.5 (all)	0
ROVPC15_1115	5S	U1519	15.5	1	1
BB29	7S	U1518	75	7.5	0.05
BB33	HFA_S	U1518	134.5	0	0.07
BB58	3N	U1519	165	35	0.05
BB59	3N	U1519	110	35	0.1
BB64	4N	U1519	277	35	0
BB67	4N	U1519	45	25	0
BB68	4N	U1519	95	0	0
BB70	5N	U1519	235	235 (all)	0
BB71	5N	U1519	235	235 (all)	0
BB74	5N	U1519	325	0	ND
ROVPC1_1121	5N	U1519	20	14	2
BB42	1N	U1518	225	225 (all)	0
BB76	HFA_N	U1518	193.5	0	ND
BB80	HFA_N	U1518	243.5	0	0.05
BB81	HFA_N	U1518	155	155 (all)	0
BB84	HFA_N	U1518	212	0	0.05
JPC02	HFA_N	U1518	623	0	0.05
ROVPC3_1125	HFA_N	U1518	21	21 (all)	ND

APPENDIX B: SUPPLEMENTARY INFORMATION FOR CHAPTER 3

BENTHIC FLUID FLOW METERS

We used two types of benthic fluid flow meters in this study: 1) Chemical Aqueous Transport (CAT) meters and 2) Multiple Orifice Sampler and Quantitative Injection Tracer Observers (MOSQUITOs). We provide brief descriptions of each instrument below. See Tryon et al., (2001) and Solomon et al., (2008) for complete descriptions of the CAT meters and MOSQUITOs, respectively.

The primary components of a CAT meter are 1) a fluid collection chamber (Ti, cross-sectional area of 0.37 m^2) that sits coupled to the seafloor and 2) a PVC box mounted on the chamber, housing an osmotic pump (Jannasch et al., 2004), two sample coils of Teflon tubing pre-filled with ultra-pure water, and a bag of RbCl tracer solution density-matched to seawater (**Fig. B1**). Throughout deployment, the osmotic pump continuously pumps tracer solution from the tracer bag into an inlet/outlet tube which connects the sample coils to the collection chamber. Concurrently, fluid is drawn from the inlet/outlet tube into the two sample coils, displacing the ultrapure water. The two sample intakes are located on either side of the tracer injection point (i.e., one sample coil is positioned to draw fluid from downstream of the tracer injection point, and the other draws from upstream of the tracer injection point). The fluid contained in each sample coil will then be a mixture of tracer, pore water, or seawater. The proportions of each component will vary through time depending on the rate and polarity (upward or downward) of fluid flow across the sediment water interface. Funneling of fluid form the collection chamber (large cross-sectional area) into the inlet/outlet tube (small cross-sectional area) amplifies the flow signal, allowing resolution of extremely low flow rates. The two sample intakes poised on

either side of the tracer injection point allow for measurement of both upward and downward flow.

Upon deployment of a MOSQUITO, five Ti needles of different lengths are driven into the sediment, penetrating to depths of ~10-30 cmbsf (**Fig. B2**). A discrete volume of fluorescein tracer solution, density-matched to seawater, is then injected as a point-source into the sediment through the second-deepest needle. Each of the other four (sampling) needles is connected to a sample coil of Teflon tubing that is pre-filled with ultrapure water and an osmotic pump. Throughout deployment, the osmotic pumps draw water from the tip of each sampling needle, located within the sediment just above or just below the tracer injection point, and into a sample coil. The concentration of tracer in each sample coil will change over time as a function of diffusion as well as the rate and polarity of fluid advection. The direct sampling of pore water through needles mitigates the impact of shallow bioturbation processes on fluid flow rate estimates, and provides un-diluted pore water samples that can be chemically analyzed to infer fluid sources and in situ biogeochemical reactions.

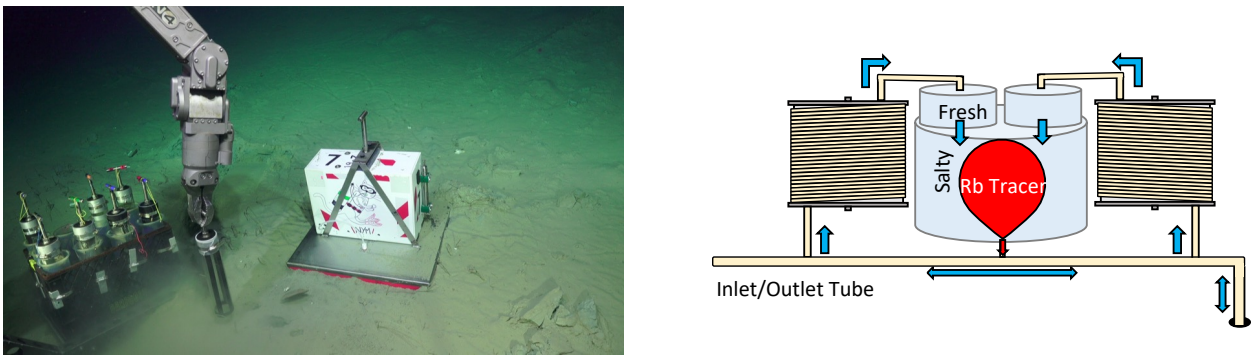

Figure B1. Photo and internal diagram of CAT meter
Note that freshwater chambers in diagram are at the top of the osmotic pump for visual clarity only.

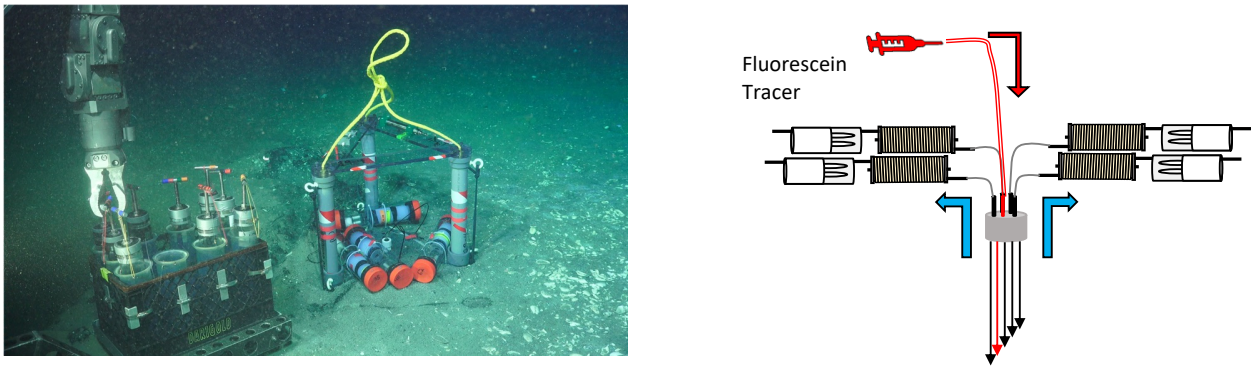

Figure B2. Photo and internal diagram of MOSQUITO.

APPENDIX C: SUPPLEMENARY INFORMATION FOR CHAPTER 4

SUPPLEMENTARY FIGURES AND TABLES

Table C1. Sediment core locations and modeling results.
Gravity and push cores have prefixes "BB" and "ROVPC," respectively. Positive flow rates indicate upward flow. Mixed layer depth is the depth of near-seawater alkalinity concentrations. Cores that were not analyzed for Cl were not modeled ("-").

Core	Lat.	Lon.	Location Description	Deepest Sample (cmbsf)	Mixed layer Depth (cmbsf)	Modeled Flow Rate (cm/yr)
BB2	44.4847	-125.0639	Near Blow Out	95	0	5.5
BB5	44.4872	-125.0677	N of Pythia	236	75	1.5
BB7	44.4866	-125.0683	W of Pythia	200	0	2
BB8	44.4861	-125.0687	SW of Pythia	404.5	75	no fit
BB10	44.4879	-125.0678	N of Pythia	301	-	-
BB11	44.4867	-125.0665	E of Pythia	110	0	downward flow
BB12	44.4866	-125.0664	E of Pythia	256	42	-
BB13	44.4866	-125.0684	W of Pythia	102	0	downward flow
BB14	44.4866	-125.0678	Near Pythia	65	0	4.5
BB15	44.4868	-125.0686	W of Pythia	295	0	-
BB16	44.4889	-125.0719	Near Promontory	318.5	0	downward flow
BB17	44.4870	-125.0669	NE of Pythia	290	0	downward flow
BB18	44.4855	-125.0643	N of Blow Out	43	0	downward flow
BB19	44.4858	-125.0639	N of Blow Out	277	0	downward flow
BB20	44.4851	-125.0650	Near Blow Out	108	0	6
BB21	44.4868	-125.0687	W of Pythia	255	50	-
BB22	44.4827	-125.0622	Near Moat	365	0	2

Table C1 continued.

BB23	44.4867	-125.0677	Near Pythia	70	0	downward flow
BB24	44.4865	-125.0678	Near Pythia	8.5	0	-
BB25	44.4861	-125.0679	S of Pythia	75	0	5
BB27	44.4813	-125.0639	Near Moat	284	75	3
ROVPC 4	44.4844	-125.0631	Near Blow Out	11	0	no fit
ROVPC 6	44.4843	-125.0633	Near Blow Out	11	0	downward flow
ROVPC 9	44.4866	-125.0680	Near Pythia	9	5	-
ROVPC 10	44.4867	-125.0680	Near Pythia	5	5	-
ROVPC 11	44.4866	-125.0678	Near Pythia	19	9	-
ROVPC 12	44.4866	-125.0678	Near Pythia	15	15	-

Table C2. Flow rate modeling input parameters.

Input parameters	
Pore Water Cl data	Measured profile
Porosity (nearest core)	Measured profile
Top Boundary Cl (0 depth; mM)	548
Bottom Boundary Cl (mM)	Deepest measured value
Reaction Rate ($mol/m^3/yr$)	0
Bottom Water Temp. (˚C)	3.3
Sedimentation Rate (cm/yr)	0.015
Temp. Gradient (˚C/m)	0
Spatial Interval (cm)	~5
Spatial Steps	~18
Time Interval (yr)	0.1
Time Steps	3×10^4

Table C3. Geothermometers

Comparison of Pythia's Oasis fluid compositions to high temperature experiments (above); employment of empirical and theoretical geothermometers to estimate subsurface fluid formation temperatures (below).

Geoindicator	**James et al., (2003) Escanaba sediment (˚C)**	**You et al., (1996) Nankai decollement Sediment (˚C)**	**Wei (2007) Barbados smectite (˚C)**	**Wei (2007) Basaltic ash + smectite (˚C)**	**Overall (˚C)**
Li	200-250	154	125-150	199-243	125-250
Ca	250	249-298	-	243-271	243-298
Mg	199-250	nd	-	171	171-250

Geo-indicator	**Equation(s)**	**Reference(s)**	**Suggested Range of Application (˚C)**	**Pythia's Oasis Result (SO_4-depleted endmember) (˚C)**
O/H isotopes	$\delta^{18}O_{clay} = \delta^{18}O_{fluid} + \left(\frac{2.55 \times 10^6}{T^2}\right) - 4.05$ $\delta D_{clay} = \delta D_{fluid} + \left(\frac{-19.6 \times 10^3}{T}\right) + 25$ $\delta D_{clay} = \delta D_{fluid} + \left(\frac{-45.3 \times 10^3}{T}\right) + 94.7$	Method from Hensen et al., (2004). Equations from Sheppard and Gilg, (1996); Yeh (1980); Cupuano (1992).	$\delta^{18}O$ eq: 0-400 δD eqs: 0-120 (You) 0-150 (Capuano)	≤ 206
Mg, Li	$T\,(^{\circ}C) = \frac{2200}{\log\left(\frac{\sqrt{Mg}}{Li}\right) + 5.47} - 273$	Kharaka and Mariner, (1989)	0-350	74
Na, Li	$T\,(^{\circ}C) = \frac{1195}{\log\left(\frac{Na}{Li}\right) - 0.13} - 273$	Fouillac and Michard, (1981)	~0-350	135

Table C3 continued.

Na, Li	$T\,(^{\circ}C) = \frac{1590}{\log\left(\frac{Na}{Li}\right) + 0.779} - 273$	Kharaka and Mariner, (1989)	0-350	92
Na, Li	$T\,(^{\circ}C) = \frac{1267}{\log\left(\frac{Na}{Li}\right) + 0.07} - 273$	Verma and Santoyo, (1997)	50-320	132

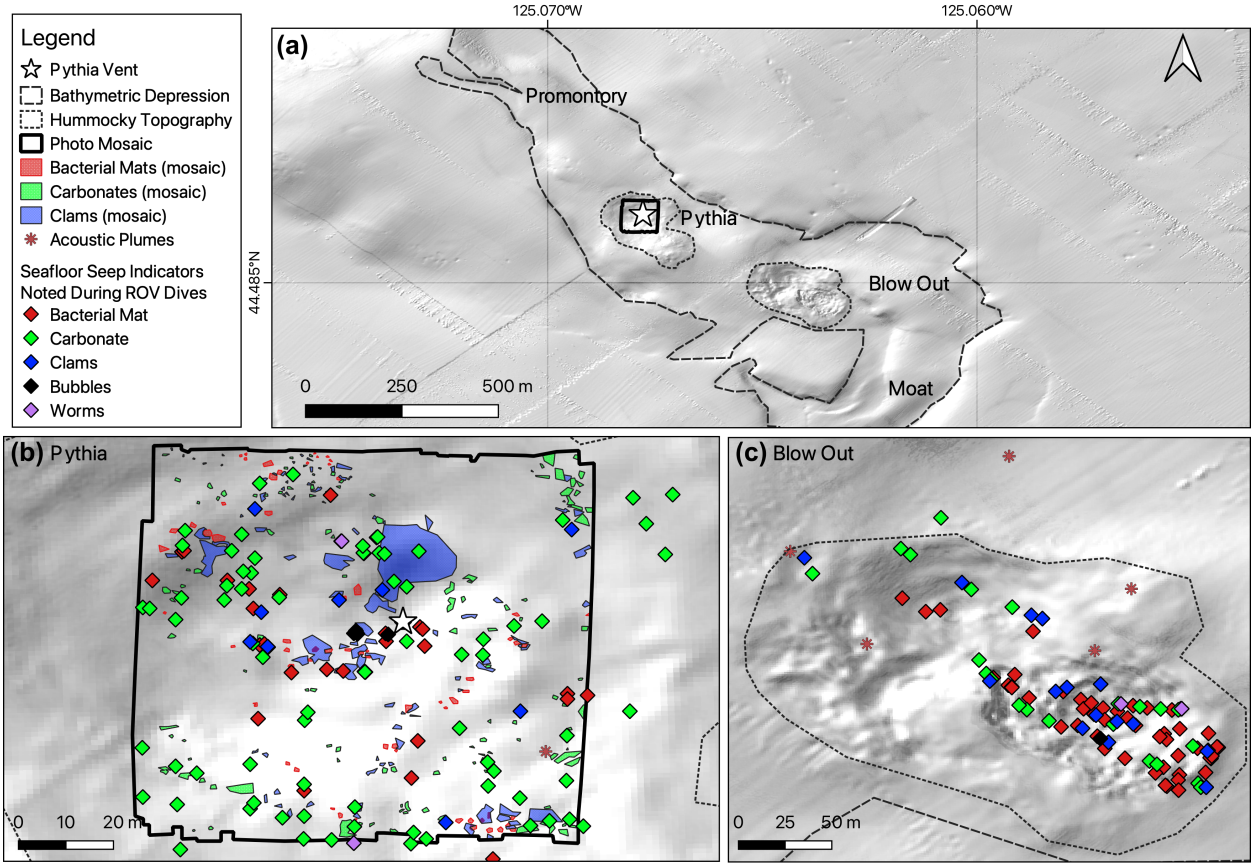

Figure C1. Observations used to estimate the spatial area of seepage at Pythia's Oasis. (a) Bathymetric depression surrounding the entire seep area, areal extent of hummocky topography surrounding Pythia and Blow Out, and area of the photomosaic produced from images collected during an ROV *Jason* dive are outlined (photomosaic courtesy of M. Elend, UW). (b) Close up of the Pythia and Blow Out sites. Seafloor seepage features noted during ROV dives (diamonds) and identified from post-cruise examination of the photo-mosaic (polygons) are shown.